**Faculteit Wetenschappen**
**Departement Fysica**

# Tight-Binding Model for Two-Dimensional Materials

_____

# Tight-Binding Model Voor Tweedimensionale Materialen

Thesis submitted to achieve the degree of
**Doctor of Science: Physics**
**Mohammad Nakhaee**

Supervisors:
**Prof. Dr. Francois Peeters**
University of Antwerpen, Antwerpen, Belgium
**Prof. Dr. Ahmad Ketabi**
Damghan University, Damghan, Iran

**February 2020**

Faculteit Wetenschappen
Departement Fysica

Damghan
University
School of Physics

*Dedicated to those who do not believe in believing.*

# ACKNOWLEDGEMENTS

# TABLE OF CONTENTS

**Page**

# INTRODUCTION

Many researchers work on the electrical properties of different crystals, nano-structures and molecules. The starting point for all of them is the Hamiltonian of the given system. In other words, if the Hamiltonian of a typical system is known, everything is computable, otherwise not. But where does this Hamiltonian come from?

For example, consider the famous two-dimensional graphene material. If the magic value of $-2.5eV$ is known as the electron hopping from one site to another site, one can calculate the Hamiltonian of this structure or any finite system created by this material and can calculate the other electronic properties of the system. To be more precise, we can see many different Hamiltonians which have also been introduced for graphene with different accuracies, with different validity ranges, that have been used by researchers. Using these Hamiltonians around 40,000 articles (up to 2020) have been reported by researchers and it reveals how much they have paved the way for the development of graphene science.

## 1.1   Nano-Materials

Hundreds of articles on nano-structures have been written in the last two decades. Therefore, there was a need to classify them. Nano-structures, as a matter of nanotechnology, can be called low-dimensional materials that

include sub-micron-sized or nano-scale units in at least one direction and with quantum size effects. The first classification of nano-structures was introduced by Gleiter [1] in 1995 and further explained in 2000 by Skorokhod [2]. Skorokhod and Pokropivny reported a modified classification scheme for nano-structures [3], which incorporates zero-dimensional, one-dimensional, two-dimensional, and three-dimensional nano-structures.

Dimension categorization of nano-materials is one of the most basic segmentation of nano-structures. In this introduction, we will only introduce the types of nano-structures and their differences, without examining details such as properties, applications and methods of synthesis. Each material in space has three dimensions of length, width and height. If a material is, at least for one of these three dimensions in the nanometer range, that material is called a nano-structure. There is no accepted definition for the nanometer range, but a more acceptable definition is one to one hundred nanometers. Because the importance of nanotechnology is due to its desirable properties and better performance, and these advantages may appear even in larger dimensions, so there are many articles that even "nano-structured" even in the case of a few hundred nanometers.

If all three dimensions of a material are in the nanometer range, they will be called zero-dimensional nano-structure. Likewise, if two dimensions of the material are in the nano-scale range, they are called one-dimensional nano-structures and if one dimension is in the nanometer range, they are called two-dimensional nano-structures. With this designation, because the nanometer dimension is shorter than the other dimensions, the dimension within the nanometer range is considered as non-dimensional.

These three types of nano-structures are fundamentally different, both in terms of synthesis and production, and in properties and applications. In general, the electrical, optical, magnetic, surface, etc. properties of these three structures are fundamentally different and, therefore, their applications are different. For example, zero-, one- and two-dimensional nano-materials are different in terms of light absorption and light emission. For example, one-dimensional nano-structures can be used for electronic interconnections, whereas zero-dimensional and two-dimensional nano-materials do not. One

important point to note is that in one-dimensional nano-materials all three dimensions can be in the nano-scale, but one of the dimensions must be several times larger than the other two dimensions. Likewise, in 2D nano-materials, the main two dimensions must be several times larger than the smallest dimension [4–8].

Zero-dimensional and three-dimensional nano-structures have a simpler synthesis method than the other two types (one-dimensional and two-dimensional), and their production costs are less, and so they are more popular and widely used. Because the properties depend on the dimensions, it is therefore necessary to have a set of uniform produced nanoparticles as much as possible ie. the distribution of the particle size should be narrow [9–13] .

Most of these structures (crystalline structures) can be derived from their bulk by reducing one or two dimension(s). But at the nano-scale, in some compounds such as carbon, in addition to the usual atomic structures (such as graphite and diamond structures), there exist new structures of zero-, one- and two-dimensional nano-materials which do not have the same bulk unit-cell. There are a variety of zero-dimensional carbon types which can be made e.g. fullerene which can be considered as a zero-dimensional nano-structure that has 20 hexagons and 12 pentagons [7, 14–16] .

One-dimensional nano-structures are those that have its main dimension, at least, several times larger or outside the nanometer range. One-dimensional nano-structures are subdivided into various types, depending on many parameters such as cross-sectional shape and aspect ratio (large to small aspect ratio). If the aspect ratio is small, it is called a nano-rod, and if the dimension is large, it is called a nano-wire. Synthesis of one-dimensional nano-materials is more difficult than zero-dimensional nano-materials and their cost-effective production is more difficult, and therefore less useful in commercial applications, but because of their special properties, they are widely used in research, electronics, applications in optics and etc.

## 1.2　Two-Dimensional Nano-Materials

Two-dimensional (2D) nano-materials are another group of nano-structures. Basically 2D nano-materials exist in two different and completely different states. The more popular is the thin-film. The schematic of some 2D materials are shown in Fig. 1.1 which can be placed on another material. The thin layer is placed on a surface of a material called substrate.
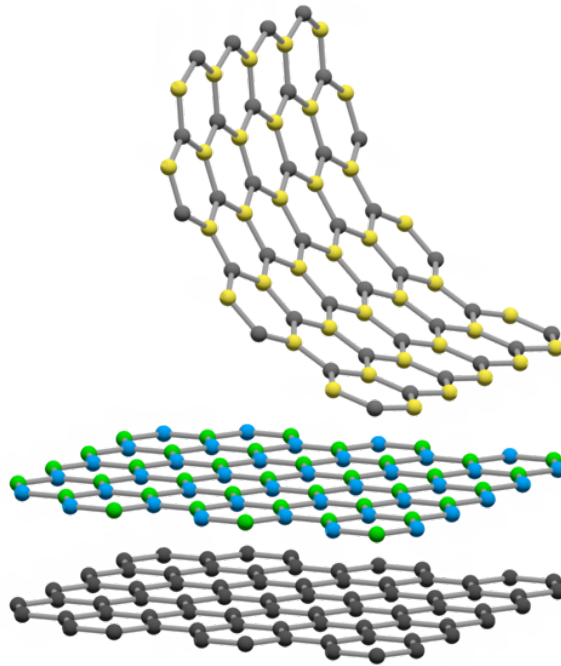


Figure 1.1: Schematic model of 2D materials

In recent years, synthesized 2D nano-structures have become a hub for material research because of their new properties. In the quest to find 2D nano-structures, over the past few years, scientists have focused on the development of 2D nano-structures. 2D nano-structures with specific geometries exhibit unique shape-dependent properties and are used as key components in nano-technologies [17–19] . In addition, a two-dimensional nano-structure is interesting, not only for basic understanding of the growth mechanism, but also for research and development of new applications in sensors, nanocontainers, nanoreactors, and photocatalysts. In Fig 1.2 , some two-dimensional nano-structures such as junctions, branched structures, nanoparticles, nanoparticles, nanowires, nanotubes, and nanodiscs are shown.
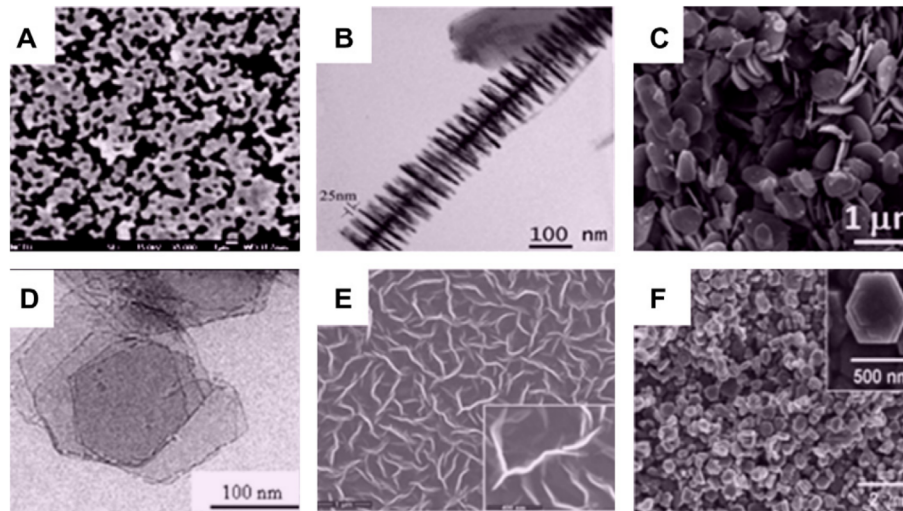
Figure 1.2: Images from electron microscopes from a variety of two-dimensional nano-structures obtained by different research groups. (A) Junctions (Continuous Islands), (B) Branched Structures, (C) Nanoplates, (D) Nanoparticles, (E) Nanowalls, and (F) Nano disks . [20–27]

Thin layers have many applications in different domains. Thin layers are widely used in the manufacturing of electronic and optical devices. Thin layers also have many uses in creating customized surface properties such as corrosion resistance, abrasion resistance, and so on. As in the case of semiconductor materials, if the thickness is low enough to allow quantum effects to prevail, the thin layer is called Quantum-well. The accuracy and quality of the layers varies depending on the application, and generally it is higher for electronics and optics. The other 2D material that is less important than thin films are those that are independent of a substrate. From this group we can name the nanosheets and the nanoplates. Nanoplates are often thicker than nanosheets. The synthesis of these nano-structures strongly depends on the crystalline structure of the material and the synthesis conditions. Quantum wells in the second group can also exist, although they are less important.

The most important 2D material is Graphene which is also called a single layer of graphite. Graphene's thickness is much less than a nanometer and about the radius of a carbon atom. Graphene has extraordinary electronic, optical, and mechanical properties. It has the specificity, highest electrical and thermal conductivity, high transparency, high strength coupled with superb

flexibility and lightness are part of the unique properties of this material. These extraordinary properties are the main reason that scientists focus on its importance and applications so that nowadays a large number of international articles on its properties and possible applications are available.

## 1.3   2D Material Applications

In recent decades, 2D materials have been used in various fields such as electronics, chemistry, physics and building industries and so on. Nano-scale transistors are used for computers with highly integrated electronic circuits. In order to further minimize nano-scale circuit components, perhaps even down to the molecular scale, researchers have suggested several alternatives to transistors. These nano-scale electronic devices resemble current transistors, both as switches or amplifiers. However, unlike today's field effect transistors, which operate based on the movement of electrons as particles in the bulk material, they benefit from quantum mechanical phenomena that occur at the nano-scale in two dimensions. The development of transistors in the mid-20th century was a revolution and a dramatic shift in the technology and manufacturing of electronic devices. The working principle of transistors that are now widely used in manufactured integrated and non-integrated electronic circuits are based on the principles of those basic and classic transistors. However, due to advances in material science and manufacturing technology, current transistors are made with much smaller dimensions, with much higher quality and durability. For example, in a computer processor, millions of silicon transistors are built side-by-side on a single chip without any slightest flaw.

## 1.4   Tight-Binding Approximation

Naturally, many of the physical properties that occur in nano-scale materials can only be investigated by quantum mechanics. These properties, including electrical, optical, acoustical, and physical properties are completely dependent on their dimensions of the crystalline structure, giving rise to a

phenomenon called Quantum Confinement Effect. In small-scale systems, the most important measurable energy variable is the status of the system. Each system has an identifier that is unique between different materials like a fingerprint, and is called band-structure. The band structure shows the energies that an electron is allowed to have in a system. In the case of molecules the band energies reduce to energy levels.

The study of the energy band structure is done in two main ways, the First-Principles Calculations and the Tight-Binding (TB) Approximation. The basics approach relies on the Hartree Fock Approximation which is computationally a self-consistent method to find the best electron density that can satisfy the Schrödinger equation. One of these methods is Density Functional Theory (DFT) which has been made concrete in various software packages. One of the advantages of this method is its accuracy which can be comparable to experiments. But at the same time, this method is inefficient for large systems. Tight-Binding method is simpler than the real Hamiltonian. TB method is very powerful in electronic band-structure calculations and has almost no limitation in the number of atoms.

The term tight refers to the approximation that the overlap of atomic wave functions is limited to neighboring atoms. Such a description allows us to skip the additional interactions in the Hamiltonian system reducing computations considerably. TB method is a quasi-experimental computational method that can calculate the energy band structure including the effects of strain, electric field, optical radiation on the material structure.

Many researchers around the world are interested in the electrical properties of various systems using the Green's function method and use the TB approximation. This method allows researchers to extend their system to very high number of atoms. Researchers can also design their systems more flexibly. For example, a non-periodic system or molecular bonding to graphene plates can be designed.

In TB model, a set of assumptions and approximations based on physics is used to facilitate and avoid large amounts of computation. These approximations are very informative and useful for understanding orbitals and examining the bonds formed between orbitals. Also this method is very ap-

plicable, because it is the first step in calculating the Green's function that are then used in any further calculations. This method is also a very powerful method to calculate the Bloch states [28–31] which has been developed by many scientists [32–34] . Meanwhile, Slater and Koster invented a very powerful method that can reproduce the hopping between all orbitals that are effective in forming the band structure.

TB approximation can be used in two different ways: orthogonal and non-orthogonal, which have their own advantages and disadvantages. We can choose the orthogonal or non-orthogonal method, depending on the accuracy required in reproducing the band-structure and the number of bands. Sometimes the orthogonal method cannot be used because the structure is very compact and, in fact, the orbitals are tightly compressed. Atomic orbitals in such compact structures have complex forms and cannot be approximated by atomic orbitals. Such structures are usually made of small atoms.

## 1.5   Slater and Koster Method

The most important operator that is the background of the idea of Slater and Koster approach is the rotation operator defined as follows

$$D(\hat{\mathbf{n}}, \phi) = \exp\left(-i\phi \frac{\hat{\mathbf{n}} \cdot \mathbf{J}}{\hbar}\right) \qquad (1.1)$$

and the SK parameters

$$h_{ll'}^{mm'}(\vec{r}) = \left\langle \varphi_l^m(\vec{x} + \vec{r}) | H(\vec{x} + \vec{r}) | \varphi_{l'}^{m'}(\vec{x}) \right\rangle,$$
$$s_{ll'}^{mm'}(\vec{r}) = \left\langle \varphi_l^m(\vec{x} + \vec{r}) | \varphi_{l'}^{m'}(\vec{x}) \right\rangle, \qquad (1.2)$$

where $\varphi_l^m(\vec{x})$ stands for a specific atomic orbital defined by angular quantum numbers $l$ and $m$. Note, the orbitals in Eq. (1.2) are the real spherical harmonics. Without any change in the basic framework one can rotate the basis vectors as follows

$$h_{ll'}^{mm'}(\vec{r}) = \left\langle \varphi_l^m(\vec{x}+\vec{r}) | \bar{D}^\dagger H(\vec{x}+\vec{r})\bar{D} | \varphi_{l'}^{m'}(\vec{x}) \right\rangle ,$$

$$s_{ll'}^{mm'}(\vec{r}) = \left\langle \varphi_l^m(\vec{x}+\vec{r}) | \bar{D}^\dagger \bar{D} | \varphi_{l'}^{m'}(\vec{x}) \right\rangle , \tag{1.3}$$

where $\bar{D} = \bar{D}(\mathbf{l}, \mathbf{m}, \mathbf{n})$ is a function of directional cosines defined by the angles of the bond vector between the atoms and the Cartesian basis vectors $\hat{x}$, $\hat{y}$ and $\hat{z}$. The rotation operator for different orbitals can be calculated from the Clebsch-Gordan coefficients. The bar symbol means symmetrized coefficients which are essential to rotate a real spherical harmonic. The complex spherical harmonics will be converted to real spherical harmonics by applying the following operators ($R_l$) for the different orbitals

$$R_0 = \begin{pmatrix} 1 \end{pmatrix},$$

$$R_1 = \begin{pmatrix} \frac{i}{\sqrt{2}} & 0 & \frac{i}{\sqrt{2}} \\ 0 & 1 & 0 \\ \frac{1}{\sqrt{2}} & 0 & -\frac{1}{\sqrt{2}} \end{pmatrix},$$

$$R_2 = \begin{pmatrix} \frac{i}{\sqrt{2}} & 0 & 0 & 0 & -\frac{i}{\sqrt{2}} \\ 0 & \frac{i}{\sqrt{2}} & 0 & \frac{i}{\sqrt{2}} & 0 \\ 0 & 0 & 1 & 0 & 0 \\ 0 & \frac{1}{\sqrt{2}} & 0 & -\frac{1}{\sqrt{2}} & 0 \\ \frac{1}{\sqrt{2}} & 0 & 0 & 0 & \frac{1}{\sqrt{2}} \end{pmatrix}. \tag{1.4}$$

The integrals of the rotated vectors in the right hand side of Eq. (1.3) are called SK parameters as $ss\sigma$, $sp\sigma$, $pp\sigma$, $pp\pi$, $sd\sigma$, $pd\sigma$, $pd\pi$, $dd\sigma$, $dd\pi$ and $dd\delta$ where the letters $s$, $p$, and $d$ refer to different orbitals and the symbols $\sigma$, $\pi$, and $\delta$ refer to different covalent bond types between the orbitals. After some simplifications one can generate the expectation values of the Hamiltonian in the basis of the directed orbitals in terms of the ten integrals as follows

$$\mathrm{s} - \mathrm{s} = \mathrm{ss}\sigma\,,$$

$$\mathrm{s} - p_y = m\mathrm{sp}\sigma\,,$$

$$p_y - \mathrm{s} = m(-\mathrm{sp}\sigma)\,,$$

$$\mathrm{s} - p_z = n\mathrm{sp}\sigma\,,$$

$$p_z - \mathrm{s} = n(-\mathrm{sp}\sigma)\,,$$

$$\mathrm{s} - p_x = l\mathrm{sp}\sigma\,,$$

$$p_x - \mathrm{s} = l(-\mathrm{sp}\sigma)\,,$$

$$\mathrm{s} - d_{\mathrm{xy}} = \sqrt{3}\,lm\mathrm{sd}\sigma\,,$$

$$d_{\mathrm{xy}} - \mathrm{s} = \sqrt{3}\,lm\mathrm{sd}\sigma\,,$$

$$\mathrm{s} - d_{\mathrm{yz}} = \sqrt{3}\,mn\mathrm{sd}\sigma\,,$$

$$d_{\mathrm{yz}} - \mathrm{s} = \sqrt{3}\,mn\mathrm{sd}\sigma\,,$$

$$\mathrm{s} - d_{3z^2-r^2} = \frac{1}{2}\left(3n^2 - 1\right)\mathrm{sd}\sigma\,,$$

$$d_{3z^2-r^2} - \mathrm{s} = \frac{1}{2}\left(3n^2 - 1\right)\mathrm{sd}\sigma\,,$$

$$\mathrm{s} - d_{\mathrm{xz}} = \sqrt{3}\,ln\mathrm{sd}\sigma\,,$$

$$d_{\mathrm{xz}} - \mathrm{s} = \sqrt{3}\,ln\mathrm{sd}\sigma\,,$$

$$\mathrm{s} - d_{x^2-y^2} = -\frac{1}{2}\sqrt{3}\,\mathrm{sd}\sigma\left(2m^2 + n^2 - 1\right)\,,$$

$$d_{x^2-y^2} - \mathrm{s} = -\frac{1}{2}\sqrt{3}\,\mathrm{sd}\sigma\left(2m^2 + n^2 - 1\right)\,,$$

$$p_y - p_y = m^2(-\mathrm{pp}\pi) + m^2\mathrm{pp}\sigma + \mathrm{pp}\pi\,,$$

$$p_y - p_z = mn(\mathrm{pp}\sigma - \mathrm{pp}\pi)\,,$$

$$p_z - p_y = mn(\mathrm{pp}\sigma - \mathrm{pp}\pi)\,,$$

$$p_y - p_x = lm(\mathrm{pp}\sigma - \mathrm{pp}\pi)\,,$$

$$p_x - p_y = lm(\mathrm{pp}\sigma - \mathrm{pp}\pi)\,,$$

$$p_y - d_{\mathrm{xy}} = l\left(-2m^2\mathrm{pd}\pi + \sqrt{3}\,m^2\mathrm{pd}\sigma + \mathrm{pd}\pi\right)\,,$$

$$d_{\mathrm{xy}} - p_y = -l\left(-2m^2\mathrm{pd}\pi + \sqrt{3}\,m^2\mathrm{pd}\sigma + \mathrm{pd}\pi\right)\,,$$

$$p_y - d_{\mathrm{yz}} = n\left(-2m^2\mathrm{pd}\pi + \sqrt{3}\,m^2\mathrm{pd}\sigma + \mathrm{pd}\pi\right)\,,$$

$$d_{\mathrm{yz}} - p_y = n\left(-\left(-2m^2\mathrm{pd}\pi + \sqrt{3}\,m^2\mathrm{pd}\sigma + \mathrm{pd}\pi\right)\right)\,,$$

$$p_y - d_{3z^2-r^2} = -\frac{1}{2}m\left(2\sqrt{3}\,n^2\mathrm{pd}\pi - 3n^2\mathrm{pd}\sigma + \mathrm{pd}\sigma\right)\,,$$

$$d_{3z^2-r^2} - p_y = \frac{1}{2}m\left(2\sqrt{3}\,n^2\mathrm{pd}\pi - 3n^2\mathrm{pd}\sigma + \mathrm{pd}\sigma\right)\,,$$

$$p_y - d_{\mathrm{xz}} = lmn\left(\sqrt{3}\,\mathrm{pd}\sigma - 2\mathrm{pd}\pi\right)\,,$$

$$d_{\mathrm{xz}} - p_y = lmn\left(2\mathrm{pd}\pi - \sqrt{3}\,\mathrm{pd}\sigma\right),$$

$$p_y - d_{x^2-y^2} = m\mathrm{pd}\pi\left(2m^2 + n^2 - 2\right) - \frac{1}{2}\sqrt{3}\,m\mathrm{pd}\sigma\left(2m^2 + n^2 - 1\right),$$

$$d_{x^2-y^2} - p_y = \frac{1}{2}\sqrt{3}\,m\mathrm{pd}\sigma\left(2m^2 + n^2 - 1\right) - m\mathrm{pd}\pi\left(2m^2 + n^2 - 2\right),$$

$$p_z - p_z = n^2(-\mathrm{pp}\pi) + n^2\mathrm{pp}\sigma + \mathrm{pp}\pi,$$

$$p_z - p_x = ln(\mathrm{pp}\sigma - \mathrm{pp}\pi),$$

$$p_x - p_z = ln(\mathrm{pp}\sigma - \mathrm{pp}\pi),$$

$$p_z - d_{\mathrm{xy}} = lmn\left(\sqrt{3}\,\mathrm{pd}\sigma - 2\mathrm{pd}\pi\right),$$

$$d_{\mathrm{xy}} - p_z = lmn\left(2\mathrm{pd}\pi - \sqrt{3}\,\mathrm{pd}\sigma\right),$$

$$p_z - d_{\mathrm{yz}} = m\left(-2n^2\mathrm{pd}\pi + \sqrt{3}\,n^2\mathrm{pd}\sigma + \mathrm{pd}\pi\right),$$

$$d_{\mathrm{yz}} - p_z = -m\left(-2n^2\mathrm{pd}\pi + \sqrt{3}\,n^2\mathrm{pd}\sigma + \mathrm{pd}\pi\right),$$

$$p_z - d_{3z^2-r^2} = \sqrt{3}\left(n - n^3\right)\mathrm{pd}\pi + \frac{1}{2}n\left(3n^2 - 1\right)\mathrm{pd}\sigma,$$

$$d_{3z^2-r^2} - p_z = \frac{1}{2}\left(n - 3n^3\right)\mathrm{pd}\sigma + \sqrt{3}\,n\left(n^2 - 1\right)\mathrm{pd}\pi,$$

$$p_z - d_{\mathrm{xz}} = l\left(-2n^2\mathrm{pd}\pi + \sqrt{3}\,n^2\mathrm{pd}\sigma + \mathrm{pd}\pi\right),$$

$$d_{\mathrm{xz}} - p_z = -l\left(-2n^2\mathrm{pd}\pi + \sqrt{3}\,n^2\mathrm{pd}\sigma + \mathrm{pd}\pi\right),$$

$$p_z - d_{x^2-y^2} = \frac{1}{2}n\left(2m^2 + n^2 - 1\right)\left(2\mathrm{pd}\pi - \sqrt{3}\,\mathrm{pd}\sigma\right),$$

$$d_{x^2-y^2} - p_z = -\frac{1}{2}n\left(2m^2 + n^2 - 1\right)\left(2\mathrm{pd}\pi - \sqrt{3}\,\mathrm{pd}\sigma\right),$$

$$p_x - p_x = \mathrm{pp}\pi\left(m^2 + n^2\right) - \mathrm{pp}\sigma\left(m^2 + n^2 - 1\right),$$

$$p_x - d_{\mathrm{xy}} = m\left(\mathrm{pd}\pi\left(2m^2 + 2n^2 - 1\right) - \sqrt{3}\,\mathrm{pd}\sigma\left(m^2 + n^2 - 1\right)\right),$$

$$d_{\mathrm{xy}} - p_x = \mathrm{pd}\pi\left(-2m^3 - 2mn^2 + m\right) + \sqrt{3}\,m\mathrm{pd}\sigma\left(m^2 + n^2 - 1\right),$$

$$p_x - d_{\mathrm{yz}} = lmn\left(\sqrt{3}\,\mathrm{pd}\sigma - 2\mathrm{pd}\pi\right),$$

$$d_{\mathrm{yz}} - p_x = lmn\left(2\mathrm{pd}\pi - \sqrt{3}\,\mathrm{pd}\sigma\right),$$

$$p_x - d_{3z^2-r^2} = -\frac{1}{2}l\left(2\sqrt{3}\,n^2\mathrm{pd}\pi - 3n^2\mathrm{pd}\sigma + \mathrm{pd}\sigma\right),$$

$$d_{3z^2-r^2} - p_x = \frac{1}{2}l\left(2\sqrt{3}\,n^2\mathrm{pd}\pi - 3n^2\mathrm{pd}\sigma + \mathrm{pd}\sigma\right),$$

$$p_x - d_{\mathrm{xz}} = n\left(2\mathrm{pd}\pi\left(m^2 + n^2 - 1\right) - \sqrt{3}\,\mathrm{pd}\sigma\left(m^2 + n^2 - 1\right) + \mathrm{pd}\pi\right),$$

$$d_{\mathrm{xz}} - p_x = -n\left(2\mathrm{pd}\pi\left(m^2 + n^2 - 1\right) - \sqrt{3}\,\mathrm{pd}\sigma\left(m^2 + n^2 - 1\right) + \mathrm{pd}\pi\right),$$

$$p_x - d_{x^2-y^2} = l\mathrm{pd}\pi\left(2m^2 + n^2\right) - \frac{1}{2}\sqrt{3}\,l\mathrm{pd}\sigma\left(2m^2 + n^2 - 1\right),$$

$$d_{x^2-y^2} - p_x = \frac{1}{2}\sqrt{3}\,l\mathrm{pd}\sigma\left(2m^2 + n^2 - 1\right) - l\mathrm{pd}\pi\left(2m^2 + n^2\right),$$

$$d_{\mathrm{xy}} - d_{\mathrm{xy}} = -\mathrm{dd}\delta\left(m^2 - 1\right)\left(m^2 + n^2\right) + 4\mathrm{dd}\pi m^2\left(m^2 + n^2 - 1\right) - \mathrm{dd}\pi n^2 + \mathrm{dd}\pi - 3\mathrm{dd}\sigma m^2\left(m^2 + n^2 - 1\right),$$

$$d_{\mathrm{xy}} - d_{\mathrm{yz}} = ln\left(m^2(\mathrm{dd}\delta - 4\mathrm{dd}\pi + 3\mathrm{dd}\sigma) - \mathrm{dd}\delta + \mathrm{dd}\pi\right),$$

$$d_{\mathrm{yz}} - d_{\mathrm{xy}} = ln\left(m^2(\mathrm{dd}\delta - 4\mathrm{dd}\pi + 3\mathrm{dd}\sigma) - \mathrm{dd}\delta + \mathrm{dd}\pi\right),$$

$$d_{\mathrm{xy}} - d_{3z^2-r^2} = \frac{1}{2}\sqrt{3}\,lm\left(n^2(\mathrm{dd}\delta - 4\mathrm{dd}\pi + 3\mathrm{dd}\sigma) + \mathrm{dd}\delta - \mathrm{dd}\sigma\right),$$

$$d_{3z^2-r^2} - d_{\mathrm{xy}} = \frac{1}{2}\sqrt{3}\,lm\left(n^2(\mathrm{dd}\delta - 4\mathrm{dd}\pi + 3\mathrm{dd}\sigma) + \mathrm{dd}\delta - \mathrm{dd}\sigma\right),$$

$$d_{\mathrm{xy}} - d_{\mathrm{xz}} = -mn\left(\mathrm{dd}\delta\left(m^2 + n^2\right) + \mathrm{dd}\pi\left(-4m^2 - 4n^2 + 3\right) + 3\mathrm{dd}\sigma\left(m^2 + n^2 - 1\right)\right),$$

$$d_{\mathrm{xz}} - d_{\mathrm{xy}} = -mn\left(\mathrm{dd}\delta\left(m^2 + n^2\right) + \mathrm{dd}\pi\left(-4m^2 - 4n^2 + 3\right) + 3\mathrm{dd}\sigma\left(m^2 + n^2 - 1\right)\right),$$

$$d_{\mathrm{xy}} - d_{x^2-y^2} = -\frac{1}{2}lm\left(2m^2 + n^2 - 1\right)(\mathrm{dd}\delta - 4\mathrm{dd}\pi + 3\mathrm{dd}\sigma),$$

$$d_{x^2-y^2} - d_{\mathrm{xy}} = -\frac{1}{2}lm\left(2m^2 + n^2 - 1\right)(\mathrm{dd}\delta - 4\mathrm{dd}\pi + 3\mathrm{dd}\sigma),$$

$$d_{\mathrm{yz}} - d_{\mathrm{yz}} = \mathrm{dd}\delta\left(m^2 - 1\right)\left(n^2 - 1\right) + n^2\left(-4\mathrm{dd}\pi m^2 + \mathrm{dd}\pi + 3\mathrm{dd}\sigma m^2\right) + \mathrm{dd}\pi m^2,$$

$$d_{\mathrm{yz}} - d_{3z^2-r^2} = \frac{1}{2}\sqrt{3}\,mn\left(n^2(\mathrm{dd}\delta - 4\mathrm{dd}\pi + 3\mathrm{dd}\sigma) - \mathrm{dd}\delta + 2\mathrm{dd}\pi - \mathrm{dd}\sigma\right),$$

$$d_{3z^2-r^2} - d_{\mathrm{yz}} = \frac{1}{2}\sqrt{3}\,mn\left(n^2(\mathrm{dd}\delta - 4\mathrm{dd}\pi + 3\mathrm{dd}\sigma) - \mathrm{dd}\delta + 2\mathrm{dd}\pi - \mathrm{dd}\sigma\right),$$

$$d_{\mathrm{yz}} - d_{\mathrm{xz}} = lm\left(n^2(\mathrm{dd}\delta - 4\mathrm{dd}\pi + 3\mathrm{dd}\sigma) - \mathrm{dd}\delta + \mathrm{dd}\pi\right),$$

$$d_{\mathrm{xz}} - d_{\mathrm{yz}} = lm\left(n^2(\mathrm{dd}\delta - 4\mathrm{dd}\pi + 3\mathrm{dd}\sigma) - \mathrm{dd}\delta + \mathrm{dd}\pi\right),$$

$$d_{\mathrm{yz}} - d_{x^2-y^2} = \frac{1}{2}mn\left(\frac{\mathrm{dd}\delta\left(n^2\left(l^2 - m^2 + 4\right) + l^2 + 3m^2 - 4\right)}{n^2 - 1} + \mathrm{dd}\pi\left(8m^2 + 4n^2 - 6\right) - 3\mathrm{dd}\sigma\left(2m^2 + n^2 - 1\right)\right),$$

$$d_{x^2-y^2} - d_{\mathrm{yz}} = \frac{1}{2}mn\left(\frac{\mathrm{dd}\delta\left(n^2\left(l^2 - m^2 + 4\right) + l^2 + 3m^2 - 4\right)}{n^2 - 1} + \mathrm{dd}\pi\left(8m^2 + 4n^2 - 6\right) - 3\mathrm{dd}\sigma\left(2m^2 + n^2 - 1\right)\right),$$

$$d_{3z^2-r^2} - d_{3z^2-r^2} = \frac{1}{4}\left(3n^4(\mathrm{dd}\delta - 4\mathrm{dd}\pi + 3\mathrm{dd}\sigma) - 6n^2(\mathrm{dd}\delta - 2\mathrm{dd}\pi + \mathrm{dd}\sigma) + 3\mathrm{dd}\delta + \mathrm{dd}\sigma\right),$$

$$d_{3z^2-r^2} - d_{\mathrm{xz}} = \frac{1}{2}\sqrt{3}\,ln\left(n^2(\mathrm{dd}\delta - 4\mathrm{dd}\pi + 3\mathrm{dd}\sigma) - \mathrm{dd}\delta + 2\mathrm{dd}\pi - \mathrm{dd}\sigma\right),$$

$$d_{\mathrm{xz}} - d_{3z^2-r^2} = \frac{1}{2}\sqrt{3}\,ln\left(n^2(\mathrm{dd}\delta - 4\mathrm{dd}\pi + 3\mathrm{dd}\sigma) - \mathrm{dd}\delta + 2\mathrm{dd}\pi - \mathrm{dd}\sigma\right),$$

$$d_{3z^2-r^2} - d_{x^2-y^2} = -\frac{1}{4}\sqrt{3}\left(2m^2 + n^2 - 1\right)\left(n^2(\mathrm{dd}\delta - 4\mathrm{dd}\pi + 3\mathrm{dd}\sigma) + \mathrm{dd}\delta - \mathrm{dd}\sigma\right),$$

$$d_{x^2-y^2} - d_{3z^2-r^2} = -\frac{1}{4}\sqrt{3}\left(2m^2 + n^2 - 1\right)\left(n^2(\mathrm{dd}\delta - 4\mathrm{dd}\pi + 3\mathrm{dd}\sigma) + \mathrm{dd}\delta - \mathrm{dd}\sigma\right),$$

$$d_{\mathrm{xz}} - d_{\mathrm{xz}} = -\left(m^2 - 1\right)n^2(\mathrm{dd}\delta - 4\mathrm{dd}\pi + 3\mathrm{dd}\sigma) + n^4(-(\mathrm{dd}\delta - 4\mathrm{dd}\pi + 3\mathrm{dd}\sigma)) + \mathrm{dd}\delta m^2 - \mathrm{dd}\pi m^2 + \mathrm{dd}\pi,$$

$$d_{\mathrm{xz}} - d_{x^2-y^2} = -\frac{1}{2}ln\left(\mathrm{dd}\delta\left(2m^2 + n^2 + 1\right) - (4\mathrm{dd}\pi - 3\mathrm{dd}\sigma)\left(2m^2 + n^2\right) + 2\mathrm{dd}\pi - 3\mathrm{dd}\sigma\right),$$

$$d_{x^2-y^2} - d_{\mathrm{xz}} = -\frac{1}{2}ln\left(\mathrm{dd}\delta\left(2m^2 + n^2 + 1\right) - (4\mathrm{dd}\pi - 3\mathrm{dd}\sigma)\left(2m^2 + n^2\right) + 2\mathrm{dd}\pi - 3\mathrm{dd}\sigma\right),$$

$$d_{x^2-y^2} - d_{x^2-y^2} = \mathrm{dd}\delta m^4 + \mathrm{dd}\delta m^2\left(n^2 - 1\right) + \frac{1}{4}\mathrm{dd}\delta\left(n^2 + 1\right)^2 - \mathrm{dd}\pi\left(2m^2 + n^2\right)^2 + 4\mathrm{dd}\pi m^2 + \mathrm{dd}\pi n^2$$

$$+ \frac{3}{4}\mathrm{dd}\sigma\left(2m^2 + n^2 - 1\right)^2. \tag{1.5}$$

Note that the equations were computed symbolically and we found that in
the paper of Slater and Koster [35] there are a few typos in the interaction

between $p$ and $d$ orbitals which will result in a wrong electronic dispersion. In the case of two atoms on top of each other to evaluate the term $d_{yz} - d_{x^2-y^2}$ one should calculate the limit of $n \to 1$.

# TIGHT-BINDING STUDIO

M any researchers are interested in the study of nanostructures and solid state materials in general, but there are many computational and mathematical challenges which hinder rapid progress. Therefore, new computational packages are urgently needed in order to accelerate scientific progress. Here, we are interested in electronic structure properties.

First-principles electronic structure calculations [36] are based on the laws of quantum mechanics and only use the fundamental constants of physics as input to provide detailed insight into the origin of mechanical, electronic, optical and magnetic properties of materials and molecules. Both structural and spectroscopic information is directly obtainable from high-performance computations and yields information which is complementary to that obtained from experimental such as transmission electron microscopy data.

Density functional theory (DFT) is one of the most important methods used in electronic structure calculations and computational physics has provided already a diverse number of software packages such as OpenMX [37], VASP [38–40], QUANTUM ESPRESSO [98] and ABINIT [42] that are based on different algorithms. The accuracy of different methods depends on the used approximations, e.g. the particular form for the exchange-correlation (XC) energy.

First-principles calculations is commonly applied to calculate the properties of an infinite periodic arrangement of one or more atoms (the basis)

repeated at each lattice point that describes a highly ordered structure, occurring due to the intrinsic nature of its constituents to form symmetric patterns. The periodicity can make problems easier, but sometimes it can be a drawback when one is interested in the electronic properties of finite size systems. Linear combination of atomic orbitals (LCAO) [43, 44] is a good candidate to overcome this problem.

The most important justification to setup LCAO is that the combination of this method with Green's function theory can be also used for non-periodic systems and furthermore, in the case of systems with a huge number of atoms there are a variety of cost and time efficiency motivations which can lead one to use the LCAO method.

Tight-Binding (TB) approaches are based on the LCAO method that is primarily used to calculate the band structure and single-particle Bloch states of a material as e.g. done by Slater and Koster (SK) [35]. The tight-binding method is simple and computationally very fast. Therefore, it is often used in calculations of very large systems, with more than a few thousand atoms in the unit cell. There are a number of earlier reviews [45, 46] that people working in this field should be aware of. TB Hamiltonian gives the electronic structure of a system using a real-space picture of the system. The real Hamiltonians provide insight into the nature of the transport mechanisms.

To find a TB Hamiltonian one needs to evaluate the band-structure of a typical structure based on first principles calculations and construct a tight-binding model via the Slater and Koster method to reproduce the band energies obtained from DFT.

The purpose of this paper is to introduce Tight-Binding Studio (TBStudio), a new technical software package for generating TB Hamiltonians based on Slater-Koster method from data obtained from first principles calculations that has been made available at *tight-binding.com*. Cross-platform graphical user interface of TBStudio is written in C++ using native controls and emulates foreign functionality via wxWidgets [47] tools library for GTK, MS Windows, and MacOS. Also, BLAS [48] and LAPACK [49] routines are used for matrix multiplications, solving systems of simultaneous linear equations and eigenvalue problems. The standard high performance OpenGL graphic

library [50] has been used for real time plotting. The main structure of TB-Studio and several important topics, including the post processing tools are explained in the rest of this paper.

## 2.1 Linear Combination of Atomic Orbitals

Consider two atoms which have atomic orbitals described by wave function $\Psi_A$ and $\Psi_B$. If the atoms are at the equilibrium distance, their electron clouds overlap with each other and the wave function of molecular orbital can be obtained from a linear combination of atomic orbitals as follows

$$\Psi_{AB} = c_A \Psi_A + c_B \Psi_B, \tag{2.1}$$

where $\Psi_{AB}$ is the normalized wave function of molecular orbitals of the molecule AB. With this in mind we are able to expand the Bloch functions as linear combinations of the orbitals $\varphi$ as follows

$$\psi_k(\mathbf{r}) = \sum_i \sum_{v_i} c_{iv_i}(k)\phi_{v_i,k}(\mathbf{r} - \mathbf{r}_i), \tag{2.2}$$

where $i$ runs over all unit cell atoms and $v_i$ runs over the orbitals defined for $i^{th}$ atom and

$$\phi_{v,\mathbf{k}}(\mathbf{r}) = \sum_{n\in\mathbb{Z}} \sum_{m\in\mathbb{Z}} \sum_{l\in\mathbb{Z}} e^{i\mathbf{k}.\mathbf{R}_{n,m,l}} \varphi_v(\mathbf{r} - \mathbf{R}_{n,m,l}), \tag{2.3}$$

in which $\mathbf{R}_{n,m,l}$ is the discrete translation vector of the unit cell at $(n,m,l)$ of the Bravais lattice. The electron hopping between different orbitals is an essential ingredient in TB approach. In a simple non-interacting picture, the overlap of the outermost electrons leads to the hybridization of the electronic orbitals and leads to the de-localization of Bloch states.

To calculate the energy bands we should solve the generalized eigenvalue problem

$$\hat{H}(\mathbf{k})\psi_n^\sigma(\mathbf{k}) = \varepsilon_{n\mathbf{k}\sigma}\hat{S}(\mathbf{k})\psi_n^\sigma(\mathbf{k}), \tag{2.4}$$

where $\hat{H}$ and $\hat{S}$ are the TB Hamiltonian and the overlap operators that can be written as

$$\hat{H} = \sum_{i,i'} \sum_{v_i, v'_i} \hat{H} |\phi_{v_i}\rangle \langle \phi_{v'_{i'}}|,$$

$$\hat{S} = \sum_{i,i'} \sum_{v_i, v'_i} |\phi_{v_i}\rangle \langle \phi_{v'_{i'}}|, \tag{2.5}$$

where in general the basis can be non-orthogonal and then the overlap matrix can be a non-identity matrix. The elements of the Hamiltonian and the overlap matrices can be found by definition of the molecular two-center integrals in terms of the quantities called Slater and Koster integrals.

## 2.2    Calculation of Slater-Koster integral Table

The most important issue that is the background of the idea of Slater and Koster approach is the rotation operator defined as follows

$$D(\hat{\mathbf{n}}, \phi) = \exp\left(-i\phi \frac{\hat{\mathbf{n}} \cdot \mathbf{J}}{\hbar}\right), \tag{2.6}$$

and the SK parameters

$$h_{ll'}^{mm'}(\mathbf{r}) = \left\langle \varphi_l^m(\mathbf{x} + \mathbf{r}) | H(\mathbf{x} + \mathbf{r}) | \varphi_{l'}^{m'}(\mathbf{x}) \right\rangle,$$

$$s_{ll'}^{mm'}(\mathbf{r}) = \left\langle \varphi_l^m(\mathbf{x} + \mathbf{r}) | \varphi_{l'}^{m'}(\mathbf{x}) \right\rangle, \tag{2.7}$$

in which $\varphi_l^m(\mathbf{x})$ stands for a specific atomic orbital defined by angular quantum numbers $l$ and $m$. Note, the orbitals in Eq. (2.7) are the real spherical harmonics. Without any change in the basic framework one can rotate the basis vectors as follows

$$h_{ll'}^{mm'}(\mathbf{r}) = \left\langle \varphi_l^m(\mathbf{x} + \mathbf{r}) | \bar{D}^\dagger H(\mathbf{x} + \mathbf{r}) \bar{D} | \varphi_{l'}^{m'}(\mathbf{x}) \right\rangle,$$

$$s_{ll'}^{mm'}(\mathbf{r}) = \left\langle \varphi_l^m(\mathbf{x} + \mathbf{r}) | \bar{D}^\dagger \bar{D} | \varphi_{l'}^{m'}(\mathbf{x}) \right\rangle, \tag{2.8}$$

where $\bar{D} = \bar{D}(l, m, n)$ operator is a function of directional cosines defined by the angles of the bond vector between the atoms and the Cartesian basis vectors $\hat{x}$, $\hat{y}$ and $\hat{z}$. The rotation operator for different orbitals can be calculated from the Clebsch-Gordan coefficients. The bar symbol means symmetrized coefficients which are essential to rotate a real spherical harmonic. The complex spherical harmonics will be converted to real spherical harmonics by applying the following operators ($R_l$) for the different orbitals

$$
R_0 = \begin{pmatrix} 1 \end{pmatrix},
$$
$$
R_1 = \begin{pmatrix} \frac{i}{\sqrt{2}} & 0 & \frac{i}{\sqrt{2}} \\ 0 & 1 & 0 \\ \frac{1}{\sqrt{2}} & 0 & -\frac{1}{\sqrt{2}} \end{pmatrix},
$$
$$
R_2 = \begin{pmatrix} \frac{i}{\sqrt{2}} & 0 & 0 & 0 & -\frac{i}{\sqrt{2}} \\ 0 & \frac{i}{\sqrt{2}} & 0 & \frac{i}{\sqrt{2}} & 0 \\ 0 & 0 & 1 & 0 & 0 \\ 0 & \frac{1}{\sqrt{2}} & 0 & -\frac{1}{\sqrt{2}} & 0 \\ \frac{1}{\sqrt{2}} & 0 & 0 & 0 & \frac{1}{\sqrt{2}} \end{pmatrix}. \tag{2.9}
$$

The integrals of the rotated vectors in the right hand side of Eq. (2.8) are called SK parameters as $ss\sigma$, $sp\sigma$, $pp\sigma$, $pp\pi$, $sd\sigma$, $pd\sigma$, $pd\pi$, $dd\sigma$, $dd\pi$ and $dd\delta$ [35, 51] where the first and the second letters are the orbital label as $s$, $p$ and $d$ and the third letter stands for the type of covalent binding which are formed by the overlap of atomic orbitals. $\sigma$, $\pi$ and $\delta$ bonds are related to the relative directions of two typical orbitals.

## 2.3 Atomic Spin-Orbit Coupling

Structures including heavy atoms show a considerable spin-orbit effect in their electronic properties [52]. Experimentally, this phenomenon is detectable as a splitting of spectral lines. The addition of spin-orbit coupling (SOC) to study such materials is known as fine structure. There are many structures [53–57] in which taking SOC into accounts becomes very important in atomistic modeling. This effect is a phenomenon that comes from a relativistic

interaction of a particle's spin with its motion inside a potential $\mathbf{V}$ and so the energy level split produced by the SOC is usually of the same order in size to the relativistic corrections to the kinetic energy. SOC fine structure can be added as a term to the Hamiltonian. The atomic spin-orbit interaction may be included in the TB model as

$$\hat{H}_{SO} = \frac{1}{2(m_e c)^2}(\nabla \mathbf{V} \times \mathbf{P}).\mathbf{S}, \tag{2.10}$$

where $\mathbf{P}$ and $\mathbf{S}$ are momentum and spin, respectively. Spin-orbit interactions can be accurately approximated by a local atomic contribution of the form

$$\hat{H}_{SO} = \sum_i \sum_v \hat{P}_{i,v} \lambda_v \mathbf{L}_i.\mathbf{S}_i, \tag{2.11}$$

in which $\hat{P}_{i,v}$ is the projection operator for angular momentum $v$ on site $i$ and $\lambda_v$ denotes the SOC constant for the angular momentum $v$, and $S_i$ is the spin operator on site $i$. The additional term in the Hamiltonian can be found by calculating the $\mathbf{L} \otimes \mathbf{S}$ operator. The angular and spin operators can be written as follows

$$\mathbf{L} = (L_x, L_y, L_z),$$
$$\mathbf{S} = (S_x, S_y, S_z), \tag{2.12}$$

where

$$L_x = \frac{L^+ + L^-}{2},$$
$$L_y = \frac{L^+ - L^-}{2i}, \tag{2.13}$$

in which $L^{+,-}$ denote the ladder operators for the orbitals. Similarly, we obtain $S_x$ and $S_y$ in terms of the $S^{+,-}$ ladder spin operators. Note that we need the operator to be compatible with the real spherical harmonics. The real SOC operator can be evaluated as follows

$$\bar{R}_l.(\mathbf{L}\otimes\mathbf{S}).\bar{R}_l^{-1}, \tag{2.14}$$

where

$$\bar{R}_l = R_l \otimes I_{2\times 2}. \tag{2.15}$$

One should find the final results for the different $s$, $p$ and $d$ orbitals as listed in Table 2.1.

Table 2.1: The real spherical harmonics for different angular quantum numbers $l$ and $m$.

| l | 0 | 1 | 1 | 1 | 2 | 2 | 2 | 2 | 2 |
|---|---|---|---|---|---|---|---|---|---|
| m | 0 | −1 | 0 | 1 | −2 | −1 | 0 | 1 | 2 |
| $\varphi$ | $s$ | $p_y$ | $p_z$ | $p_x$ | $d_{xy}$ | $d_{yz}$ | $d_{3z^2-r^2}$ | $d_{xz}$ | $d_{x^2-y^2}$ |

$$\hat{H}_s^{SOC} = \lambda_s \mathbf{L_s} \otimes \mathbf{S} = \begin{pmatrix} 0 & 0 \\ 0 & 0 \end{pmatrix},$$

$$\hat{H}_p^{SOC} = \lambda_p \mathbf{L_p} \otimes \mathbf{S} = \lambda_p \begin{array}{cccccc} & p_y & p_y & p_z & p_z & p_x & p_x \end{array} \begin{pmatrix} 0 & 0 & 0 & \frac{i}{2} & -\frac{i}{2} & 0 \\ 0 & 0 & \frac{i}{2} & 0 & 0 & \frac{i}{2} \\ 0 & -\frac{i}{2} & 0 & 0 & 0 & \frac{1}{2} \\ -\frac{i}{2} & 0 & 0 & 0 & -\frac{1}{2} & 0 \\ \frac{i}{2} & 0 & 0 & -\frac{1}{2} & 0 & 0 \\ 0 & -\frac{i}{2} & \frac{1}{2} & 0 & 0 & 0 \end{pmatrix} \begin{array}{c} p_y \\ p_y \\ p_z \\ p_z \\ p_x \\ p_x \end{array},$$

$$\hat{H}_d^{SOC} = \lambda_d \mathbf{L_d} \otimes \mathbf{S} =$$

$$
= \lambda_d
\begin{pmatrix}
0 & 0 & 0 & -\frac{1}{2} & 0 & 0 & 0 & \frac{i}{2} & -i & 0 \\
0 & 0 & \frac{1}{2} & 0 & 0 & 0 & \frac{i}{2} & 0 & 0 & i \\
0 & \frac{1}{2} & 0 & 0 & 0 & \frac{i\sqrt{3}}{2} & -\frac{i}{2} & 0 & 0 & \frac{i}{2} \\
-\frac{1}{2} & 0 & 0 & 0 & \frac{i\sqrt{3}}{2} & 0 & 0 & \frac{i}{2} & \frac{i}{2} & 0 \\
0 & 0 & 0 & -\frac{i\sqrt{3}}{2} & 0 & 0 & 0 & \frac{\sqrt{3}}{2} & 0 & 0 \\
0 & 0 & -\frac{i\sqrt{3}}{2} & 0 & 0 & 0 & -\frac{\sqrt{3}}{2} & 0 & 0 & 0 \\
0 & -\frac{i}{2} & \frac{i}{2} & 0 & 0 & -\frac{\sqrt{3}}{2} & 0 & 0 & 0 & \frac{1}{2} \\
-\frac{i}{2} & 0 & 0 & -\frac{i}{2} & \frac{\sqrt{3}}{2} & 0 & 0 & 0 & -\frac{1}{2} & 0 \\
i & 0 & 0 & -\frac{i}{2} & 0 & 0 & 0 & -\frac{1}{2} & 0 & 0 \\
0 & -i & -\frac{i}{2} & 0 & 0 & 0 & \frac{1}{2} & 0 & 0 & 0
\end{pmatrix}
\begin{matrix}
d_{xy} \\ d_{xy} \\ d_{yz} \\ d_{yz} \\ d_{3z^2-r^2} \\ d_{3z^2-r^2} \\ d_{xz} \\ d_{xz} \\ d_{x^2-y^2} \\ d_{x^2-y^2}
\end{matrix}
\;.
$$

Column labels: $d_{xy}\quad d_{xy}\quad d_{yz}\quad d_{yz}\quad d_{3z^2-r^2}\quad d_{3z^2-r^2}\quad d_{xz}\quad d_{xz}\quad d_{x^2-y^2}\quad d_{x^2-y^2}$

Please note that when we use the operators (2.9), the order of the matrix elements are not the same as complex spherical harmonics and depends on the definition of the transformation matrix ($R_l$). In this work, the order of the real spherical harmonics are presented in Table 2.1.

## 2.4 Iterative Minimization

TBStudio algorithm is based on the Levenberg–Marquardt least-squares curve fitting approach in which we have a set of data obtained from first-principles calculation and an analytical expression representing the TB model for which we have to find the best independent parameters. Generally, the sum of the squares of the deviations may be written as follows

$$S(\boldsymbol{\beta}) = \sum_n \sum_{\boldsymbol{k}} \sum_{\sigma} (\varepsilon'_{n\boldsymbol{k}\sigma} - \varepsilon_{n\boldsymbol{k}\sigma}(\boldsymbol{\beta}))^2,$$

where $\varepsilon$ and $\varepsilon'$ are, respectively, the TB results and DFT band energies and $\boldsymbol{\beta}$ is a parameter vector that is a set of independent variables i.e. SK parameters and overlap integrals and SOC. Non-linear least square minimization

problems arise especially in curve fitting where here the curves are energy bands which are highly coupled to each other. To start the minimization, the user has to provide an initial guess for $\boldsymbol{\beta}$ and using the guessed $\boldsymbol{\beta}$ and the mentioned SK parameters one can find the TB band energies and also the Jacobian matrix

$$J_{n\boldsymbol{k}\sigma,j} = \frac{\partial \varepsilon_{n\boldsymbol{k}\sigma}(\boldsymbol{\beta})}{\partial \boldsymbol{\beta}_j}.$$

In each iteration, we replace $\boldsymbol{\beta}$ by a new parameter vector $\boldsymbol{\beta} + \boldsymbol{\delta}$ in which $\boldsymbol{\delta}$ is a correction vector that can be estimated by first order Taylor series expansion of TB band energies as follows

$$\varepsilon_{n\boldsymbol{k}\sigma}(\boldsymbol{\beta} + \boldsymbol{\delta}) = \varepsilon_{n\boldsymbol{k}\sigma}(\boldsymbol{\beta}) + \boldsymbol{J}_{n\boldsymbol{k}\sigma}.\boldsymbol{\delta}.$$

At optimum values for the independent variables, the sum of square deviations has reached its minimum with respect to the independent vector and we have

$$\frac{\partial S(\boldsymbol{\beta} + \boldsymbol{\delta})}{\partial \boldsymbol{\delta}} = 0, \tag{2.16}$$

which however may also result in local minima. Depending on the problem and the system and the number of degrees of freedom, there might be many local minima which occur when the objective function value is greater than its value at the so-called global minimum. When multiple minima exist the important consequence is that the objective function definitely has a maximum value somewhere between two minima which makes it difficult to obtain a good fitting. Refinement from a bad SK parameter point (a set of independent parameter values $\boldsymbol{\beta}_0$) close to a physically unknown local minimum will be ill-conditioned and should be avoided as a starting point. Because generally we do not have an analytical expression for the TB band structure, we can not analyze the location of local minima in detail. Band structure curves have complex forms for which it is either very difficult or even impossible to derive analytical expressions for the elements of the

Jacobian. In such cases, we need to find the elements by using numerical approximations as follows

$$\frac{\partial \varepsilon_{n\boldsymbol{k}\sigma}(\boldsymbol{\beta})}{\partial \boldsymbol{\beta}_j} \approx \frac{\varepsilon_{n\boldsymbol{k}\sigma}(\boldsymbol{\beta}+\boldsymbol{\delta}) - \varepsilon_{n\boldsymbol{k}\sigma}(\boldsymbol{\beta}-\boldsymbol{\delta})}{2\boldsymbol{\delta}_j}.$$

## 2.5   Explicit form for the Tight-Binding Hamiltonian

Fig. 2.1 shows a schematic representation of the TB model. The mono-electronic Hamiltonian $H$ and the overlap matrix $S$ may be rewritten as

$$\hat{H} = \sum_{n\in\mathbb{Z}}\sum_{m\in\mathbb{Z}}\sum_{l\in\mathbb{Z}} \hat{h}_{l,n,m} e^{i\mathbf{k}.\mathbf{R}_{l,m,n}}, \tag{2.17}$$

and

$$\hat{H} = \sum_{n\in\mathbb{Z}}\sum_{m\in\mathbb{Z}}\sum_{l\in\mathbb{Z}} \hat{s}_{l,n,m} e^{i\mathbf{k}.\mathbf{R}_{l,m,n}}. \tag{2.18}$$
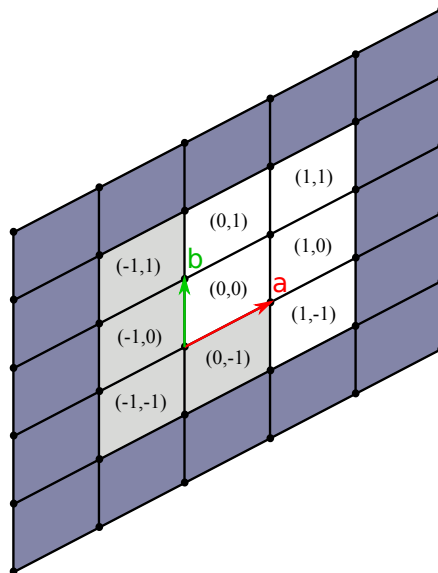


Figure 2.1: Schematic representation of the TB model for a typical 2D crystal. The red (**a**) and green (**b**) vectors are the unit vectors and the white cells indicate independent unit cells.

Since $\mathbf{H}$ and $\mathbf{S}$ are Hermitian, therefore

$$\hat{h}_{-n,-m,-l} = \hat{h}^{\dagger}_{n,m,l},$$
$$\hat{s}_{-n,-m,-l} = \hat{s}^{\dagger}_{n,m,l}, \tag{2.19}$$

and thus, in this two dimensional example, we have only five independent matrices. As shown in Fig. 2.1 we must determine only the matrices $\mathbf{h}$ and $\mathbf{s}$ for the cells at $(0,0)$, $(1,0)$, $(0,1)$, $(1,1)$ and $(-1,1)$. Using the SK coefficients we can calculate the Hamiltonian and the overlap matrix and extract the matrices $\mathbf{h}$ and $\mathbf{s}$. TBStudio generates the Hamiltonian and overlap matrix for any independent unit cell. Also the code generator tool builds Eqs. (2.17) and (2.18) in other desired programming languages. Also, one can use the outputs from TBStudio for post-processing in other transport packages. There are many useful packages for fast calculation of various physical properties of tight-binding models such as PyBinding [58], Kite [59], Kwant [60], GPUQT [61], TBTK [62], PythTB [63] and WannierTools [64].

After determining the Hamiltonian and the overlap matrix, one can easily calculate the eigenstates and the Bloch functions as well using Eqs. (2.2) and (2.3). The $i^{th}$ Wannier function (WF) for the cell $(l, m, n)$ is the Fourier coefficient of $\psi_{i,k}(\mathbf{r})$ as follows

$$w_i^{l,m,n}(r) = \frac{V}{8\pi^3} \int d^3\mathbf{k} \, e^{-i\mathbf{k}.\mathbf{R}_{l,m,n}} \psi_{i,k}(\mathbf{r}). \tag{2.20}$$

The WF calculated by this method is very close to the real chemical bonding and provides a reliable insight into the nature of the orbitals in the study of electronic properties of solids. It should be noted that, in this way we do not have the problem which we encounter in finding WFs using Maximally Localized Wannier Functions (MLWF) method [65]. Practically, MLWF algorithms change the shape of WF mathematically to find a perfect fitting to regenerate the band-structure obtained by first-principle methods, because a set of WFs which can generate the obtained band-structure is not unique and may physically not a good set of atomic-orbital-like WFs. In such algorithms that has been implemented in Wannier90 [66] and OpenMX

[37], to achieve a physically reliable set of WFs one needs to have a good initial guess and also follow the symmetry adapted methods, but it results in computational difficulties and convergence failure.

## 2.6   Download

The supporting information and several examples are available at *tight-binding.com*. The examples and the supporting codes in additional programming languages, i.e. Matlab, Mathematica, Python, C, C++ and Fortran are also accessible through Code Generator tools in TBStudio.

# BOROPHENE AND HYDROGENATED BOROPHENE

Awide range of two-dimensional (2*D*) materials ranging from graphene to topological insulators [67–72] share the extraordinary phenomenon that electrons behave as relativistic particles in their low-energy excitations. This emergent behavior of fermions in condensed matter systems has been classified as "Dirac materials" which have attracted both experimental and theoretical researches.

Recently, a fully metallic boron based two dimentional nano-structure has been synthesized on a silver crystal by physical vapor deposition, named as borophene [73–77]. There are many phases of bulk and 2*D* boron allotropes such as $\alpha$, $\beta$ and so on, which have been proposed theoretically [78–80]. Although, boron avoids to participate in the formation of chemical bonds to make a stable honeycomb lattice, it is possible to make a stable planar structure by a mixture of honeycomb together with triangular units [81, 82]. This structure contains two atoms per primitive unit cell which is called 2B:Pmmn in which Pmmn stands for the Space Group 59 included in Orthorhombic Crystal System. In 2016 Xu et al. [83] predicted a novel Dirac material: hydrogenated borophene (borophane) exhibiting Dirac characteristics with a remarkable Fermi velocity which is nearly twice that of graphene.

Free standing borophene has imaginary frequencies in its phononic dispersion and consequently is dynamically unstable and therefore it needs a substrate to be stabilized. In contrast, borophane has a dynamically stable structure

and density functional theory (DFT) calculations showed that borophane has an anisotropic Dirac cone between the $\Gamma$ and $X$ points [83]. Considering the recent successful realizations of graphene, silicene, germanene and stanene with similar structure, the predicted borophane with Dirac characteristics and ultra-high Fermi velocity is a novel interesting 2D material. In contrast to group $XIV$ elements (C, Si, Ge, Sn) of the periodic table, borophene and borophane have no similar hexagonal honeycomb monolayer structures because of their electron deficiency [80].

DFT calculations have revealed that the Dirac cone in borophane, unlike for the group $XIV$ elements [84], is not made up of only the $p_z$ orbital. In view of the position of the Dirac cone in the Brillouin zone and its lattice structure, one has to take both $p_x$ and $p_y$ orbitals also into account in the calculations. The goal of the present paper is to evaluate the best Slater-Koster coefficients to generate the Dirac point in borophane within the tight-binding (TB) approximation with fitting to DFT results and to obtain accurate results for the position of the Dirac cone and the velocity of the electrons at the Fermi level. The fitting approach is described in section 6.3 followed by an analysis of the energy spectrum around the Dirac cone in section 3.2.

## 3.1   Tight-binding model

With the linear combination of atomic orbitals (LCAO) method the system can be described by a set of non-interacting single-particles. The Slater and Koster scheme [35] is a powerful method to reproduce the first-principles data. The Naval Research Laboratory (NRL) scheme [85] is an extension of the SK method and an alternative method useful for systems including large number of atoms in the unit-cell. The Slater and Koster scheme has been applied to construct the tight-binding Hamiltonian of different systems. We follow the usual Levenberg-Marquardt nonlinear fitting algorithm [86] to find the best entries for both Hamiltonian and overlap matrices. The idea is to find the Slater-Koster coefficients for the boron-boron bonds in borophene and use them as initial guess for borophane and then to find the parameters of the hydrogen-boron bonds to reproduce the Dirac cone.

For the borophene lattice with a basis of two boron atoms, one can assume a basis of four cubic harmonic orbitals [87] (one atomic-like $s$ and three $p_x$, $p_y$ and $p_z$ orbitals per atom), which generates a band structure with four valence and four conduction bands. In the case of borophane, two hydrogens will be added in the basis for which one can add one atomic-like $s$ orbital for each hydrogen. So we have ten bands, but we will focus on the first five bands. The starting point to construct the model is the following expression [88]

$$\sum_{v'}\sum_{i'}[H_{iv,i'v'} - \epsilon_k S_{iv,i'v'}]c_{i'v'}(k) = 0\,,\tag{3.1}$$

where

$$H_{iv,i'v'} = <\phi_v(r - r_i)|H|\phi_{v'}(r - r_{i'})>$$

$$S_{iv,i'v'} = <\phi_v(r - r_i)|\phi_{v'}(r - r_{i'})>\,.\tag{3.2}$$

Here $H$ is the mono-electronic Hamiltonian and $S$ is the dimensionless overlap matrix with the basis formed by functions that are not orthonormal [89–91]. The integrals are calculated over the whole unit cell and $i$ and $v$ run over the atoms in the unit cell and the orbitals $s$, $p_x$, $p_y$ and $p_z$, respectively. Theoretically, the interatomic matrix elements mentioned in Eq. (3.2) can in principle be calculated directly from the known wave functions. In 1954 J. C. Slater and G. F. Koster [85] represented the expectation values of the Hamiltonian in the basis of the directed orbitals in terms of eight integrals ($v_{ss\sigma}$, $v_{sp\sigma}$, $v_{pp\sigma}$, $v_{pp\pi}$, $s_{ss\sigma}$, $s_{sp\sigma}$, $s_{pp\sigma}$, $s_{pp\pi}$) as follows

$$<s|H|s> = v_{ss\sigma}$$

$$<s|H|p_i> = n_i v_{sp\sigma}$$

$$<p_i|H|p_j> = (\delta_{ij} - n_i n_j)v_{pp\pi} + n_i n_j v_{pp\sigma}$$

where $n_i = \mathbf{r}.\mathbf{e}_i/|\mathbf{r}|$ is the directional cosines in which $\mathbf{r}$ is the vector along the bond and $i$ runs over $x$, $y$ and $z$. The corresponding expressions for the overlap matrix can be found by replacing $H$ by $S$ and $v$ by $s$. To evaluate complex conjugated hopping matrix elements we use the rule of angular quantum number: $<l|H|l'> = (-1)^{l+l'} <l'|H|l>$.

In practice, the unknown parameters are determined by a best fitting of the
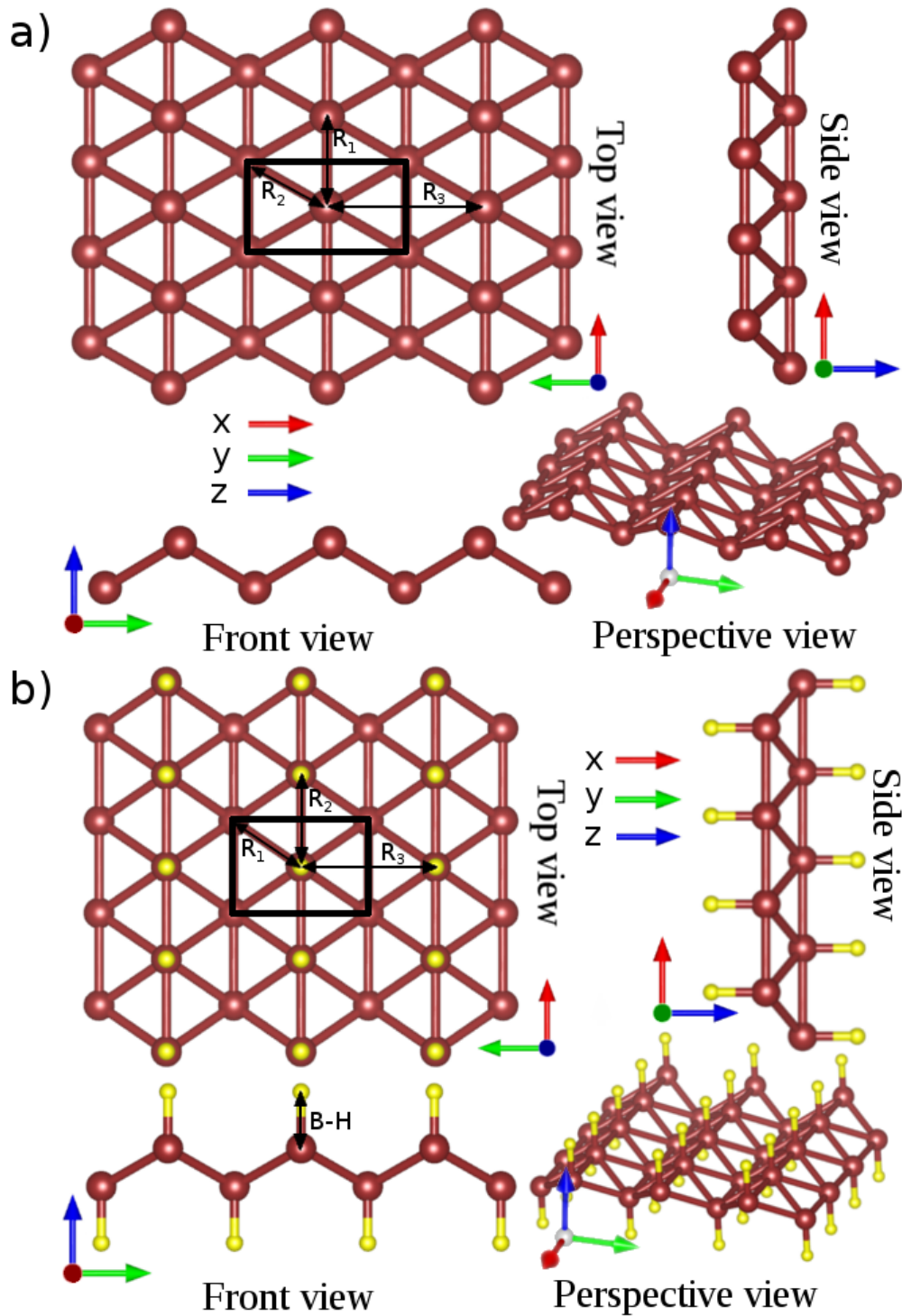
Figure 3.1: The optimized structure of (a) borophene and (b) borophane. Black rectangle refers to the unit cell. Red (yellow) dots are boron (hydrogen) atoms. $R_i$ denotes the distance between boron atoms and the H-B means the length of the hydrogen-boron bond.

energy bands that are obtained by other methods. We calculate the values of the eight integrals up to distances of the third nearest neighbor sites.

In this work, the electronic properties of borophene and borophane are investigated by first-principles calculations which are used to fit the TB parameters. Atomic structure relaxations and calculations of electronic properties were performed using OpenMX package [37] within the linear combination of pseudo-atomic orbitals (LCPAO) method [92]. Structure relaxations were carried out using the quasi-Newton scheme till the forces on the atoms become less than $10^{-5} eV/A$. The exchange-correlation energy was treated within the generalized gradient approximation (GGA), using the Perdew, Burke, and Ernzerhof (PBE) functional [93, 94]. A kinetic cutoff energy of 400 eV for the plane-wave basis was adopted. Brillioun zone integrations were evaluated with the Monkhorst-Pack mesh ($22 \times 15 \times 1$).

The fully relaxed borophene and borophane layers are displayed in Fig. 3.1. The optimized atomic positions and lattice constant for both borophene ($a = 1.62$Å and $b = 2.85$Å) and borophane ($a = 1.92$Å and $b = 2.81$Å) are in agreement with previous works [80, 83]. It should be noted that the lattice constant $a$ of borophane is remarkably increased with about 18.4 percents as compared with that of borophene, while the lattice vector $b$ is practically unchanged and as a result, the $B - B$ bond length in borophene is stretched which consequently will affect the electrical properties along the x-direction. To calculate the TB Hamiltonian by using the eight Slater-Koster integrals one needs to know the distance between the atoms. As shown in Fig. 3.1 the distance between two boron atoms is indicated by $R_i$ in which $i$ runs over three types of bonds between boron atoms and H-B is the length of the hydrogen-boron bond. After optimizing the atomic positions one finds the distances $R_1 = 1.625$Å, $R_2 = 1.851$Å and $R_3 = 2.852$Å for borophene and $R_1 = 1.881$Å, $R_2 = 1.923$Å, $R_3 = 2.806$Å and H-B $= 1.189$Å for borophane. Note that $R_1$ and $R_2$ are interchanged when going from borophene to borophane (see Figs. 3.1(a,b)).

The bandstructure of both systems is displayed in Fig. 3.2. Note that the bands of both systems are formed by cubic harmonic orbitals $s$, $p_x$, $p_y$ and $p_z$ and, as shown, the Dirac cone for borophane (right figure) is formed by the intersection between $p_x$ and $p_y$ bands.

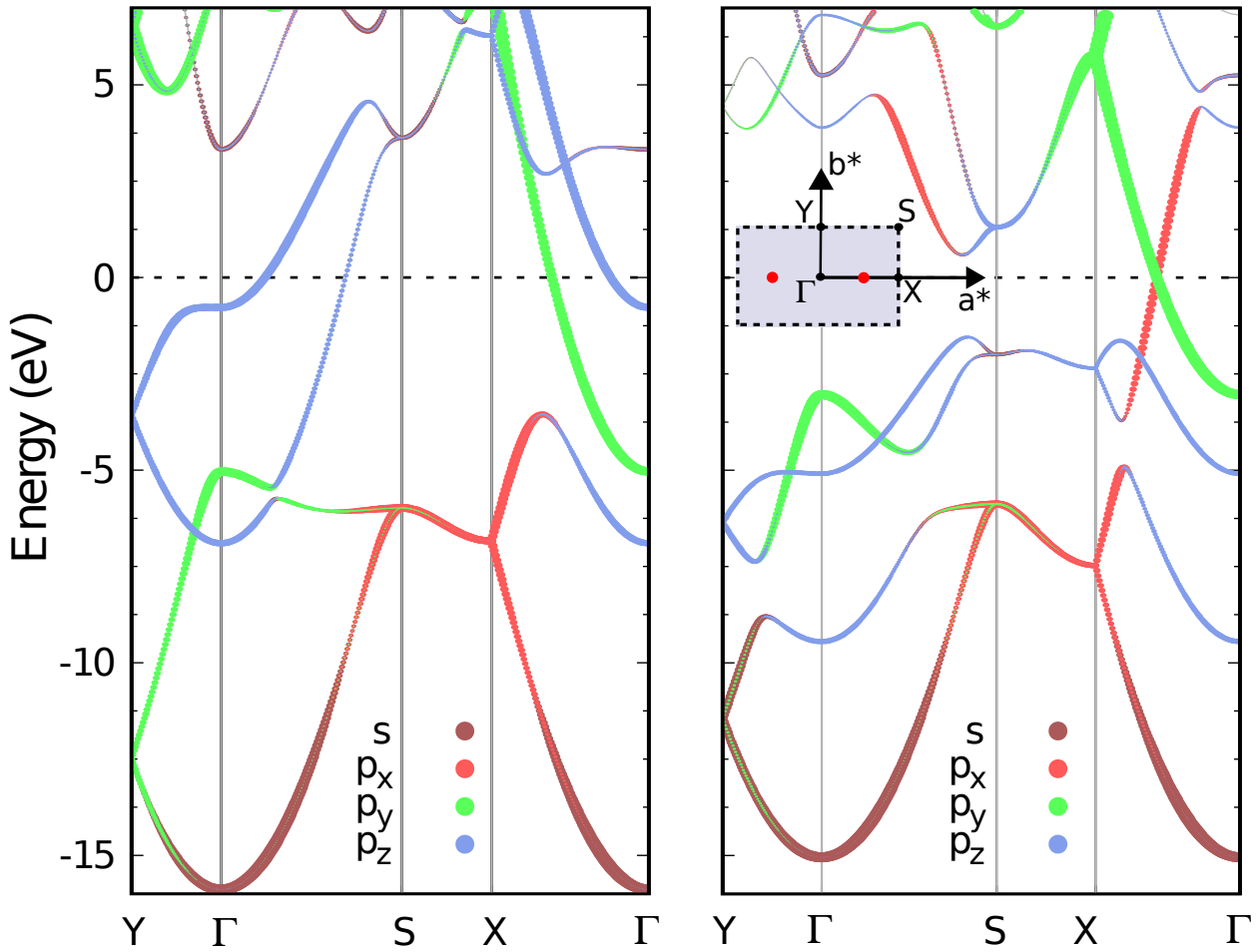In contrast to group $XIV$ sheets which have a Dirac cone formed by the

Figure 3.2: The bandstructure of borophene (left side) and borophane (right side). Red points in the Brillouin zone (see inset in right figure) indicate the positions of the Dirac cones and $a^* = \frac{2\pi}{a}\hat{a}$ and $b^* = \frac{2\pi}{b}\hat{b}$ are the reciprocal lattice vectors.

$p_z$ orbital, in borophene and borophane the contributions of other orbitals in the valence and conduction bands are significant. Considering that we want to construct a TB model up to three neighbors, a good tight-binding fitting can only be achieved if the orbitals on the different sites are assumed to be non-orthogonal as is common practice. The complicated electronic dispersion bands and the compact structure of borophene exhibit a $sp^3$ hybridization. Note that the first nearest neighbor of a boron atom in borophene lies at the nearest cell along $a$ and not in the primitive cell (see Figs. 3.1(a,b)). For both structures we have found the Slater-Koster integrals of boron-boron bonds up to the third nearest neighbors which result in a satisfactory fitting of the band structure (see Fig. 3.3). In hydrogenated borophene we add an $s$ orbital

in the position of the hydrogen atom and find its on-site and Slater-Koster parameters related to the first nearest boron atom in the lattice. There are 9 parameters which define the hoppings of an electron between the boron atoms and hydrogen located on top or below the boron layer. From a view of the location of the hydrogen atoms one can figure out that the $x$ and $y$ directional cosines are zero and accordingly, we have to determine an addition of 5 non-zero parameters for borophene.

In Table 3.1, we list the Slater-Koster parameters of both systems in terms of bond length and bond type as obtained by fitting the DFT energy bands shown in Fig. 3.3. The rather large overlap values are an indication for the short interatomic distance between the boron atoms. The on-site parameters of boron and hydrogen atoms are presented in Table 3.2. Using the Slater-Koster parameters one can calculate the Hamiltonian and the overlap matrix in terms of hoppings between different orbitals (see Appendix A).

| $R$ | $V_{ss\sigma}$ | $V_{sp\sigma}$ | $V_{pp\sigma}$ | $V_{pp\pi}$ | $S_{ss\sigma}$ | $S_{sp\sigma}$ | $S_{pp\sigma}$ | $S_{pp\pi}$ |
|---|---|---|---|---|---|---|---|---|
| $R_1$ | -3.728 | -4.391 | 4.445 | -2.298 | 0.213 | 0.287 | -0.384 | 0.063 |
| $R_2$ | -2.410 | -3.701 | 3.575 | -0.815 | 0.019 | 0.168 | -0.235 | -0.037 |
| $R_3$ | -0.279 | -0.825 | 1.914 | -0.543 | -0.034 | -0.022 | 0.017 | 0.034 |
| $R$ | $V_{ss\sigma}$ | $V_{sp\sigma}$ | $V_{pp\sigma}$ | $V_{pp\pi}$ | $S_{ss\sigma}$ | $S_{sp\sigma}$ | $S_{pp\sigma}$ | $S_{pp\pi}$ |
| $R_1$ | -2.822 | 2.987 | 2.290 | -0.672 | -0.0490 | -0.007 | -0.147 | 0.010 |
| $R_2$ | -0.742 | 1.709 | 2.076 | -1.381 | 0.150 | -0.212 | -0.421 | 0.049 |
| $R_3$ | -0.064 | 0.692 | 0.993 | -0.428 | 0.062 | -0.102 | -0.056 | 0.037 |
| H-B | 4.523 | -3.941 | 0.000 | 0.000 | -0.113 | -0.347 | 0.000 | 0.000 |

Table 3.1: The Slater-Koster parameters for borophene (top) and borophane (bottom). The $V$ parameters are in $eV$, and the $S$ parameters are dimensionless.

| | borophene | | | | borophane | | | |
|---|---|---|---|---|---|---|---|---|
| | $s$ | $p_x$ | $p_y$ | $p_z$ | $s$ | $p_x$ | $p_y$ | $p_z$ |
| **B** | -4.949 | 1.601 | -1.298 | 2.997 | -3.131 | 3.861 | 0.103 | -1.015 |
| **H** | | | | | 7.575 | | | |

Table 3.2: The on-site energies for borophene and borophane in units of $eV$.
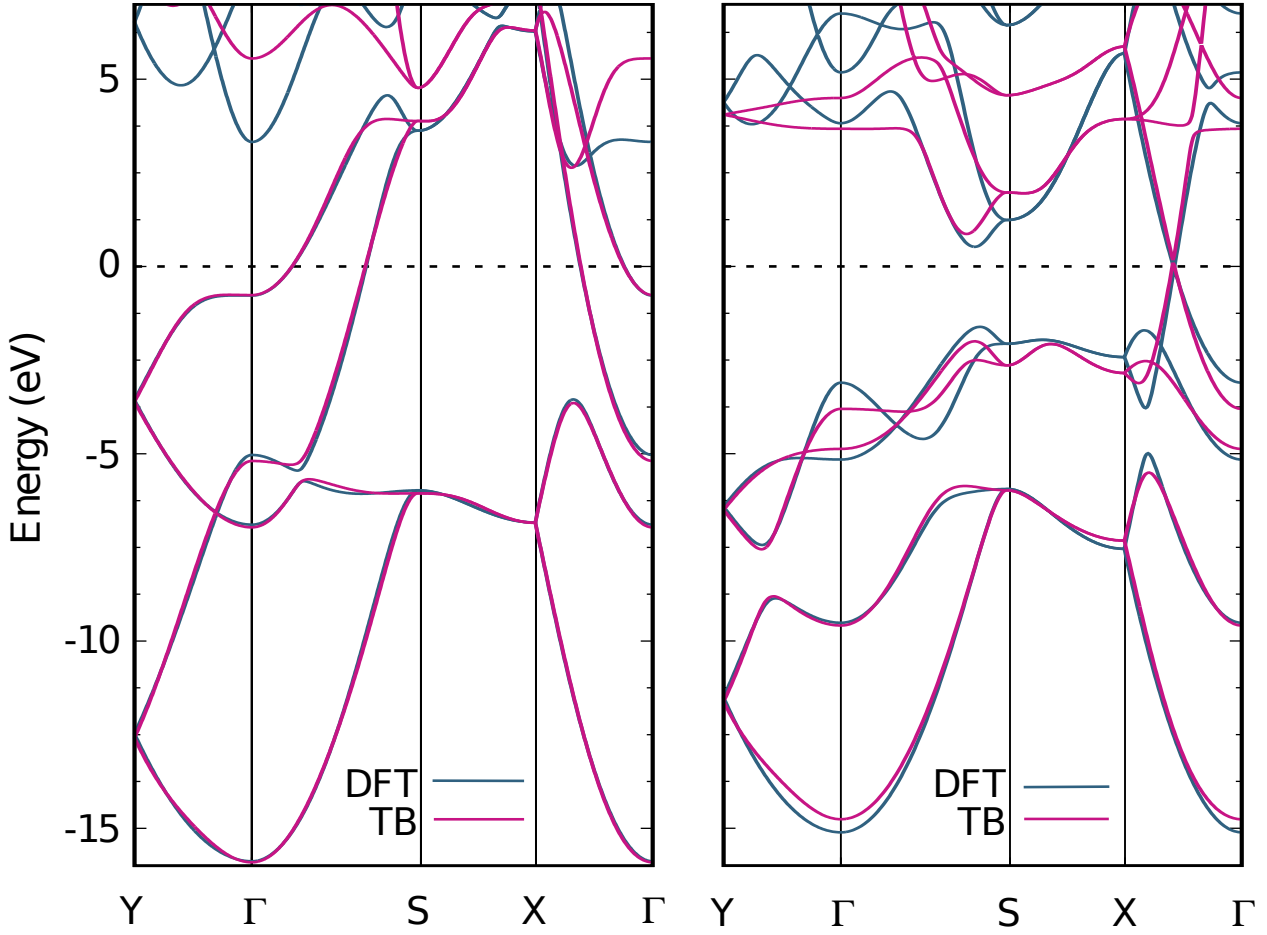
Figure 3.3: The fitted tight-bindig bandstructure of borophene (left side) and borophane (right side).

## 3.2 Low-Energy two-band Effective Hamiltonian for borophane

Concerning the Dirac cone found in the borophane bandstructure between the $\Gamma$ and $X$ points one more simplification will be made. We will construct the analog of the Dirac equation for relativistic spin one-half particles within the two band effective massless Dirac Hamiltonian that is valid for low energies. The correspondig Hamiltonian for the Dirac cone located at $\mathbf{k}_d = (\pm 0.64, 0, 0)\text{Å}^{-1}$ is given by the following equation

$$H_D = v_x \sigma_x p_x + v_y \sigma_y p_y + v_t I p_x \tag{3.3}$$

where $\sigma_x$ and $\sigma_y$ are the Pauli matrices and $I$ is the identity matrix of size 2. This expression defines a general anisotropic two-dimensional Dirac cone

which is described by three constants $v_x, v_y, v_t$ which stand for the velocity in the $x$ and $y$ directions and the degree of tilting in the x-direction, respectively. Diagonalizing this Hamiltonian results in the energy dispersion

$$\epsilon(k_x, k_y) = (k_x - k_d)v_t \pm \sqrt{(k_x - k_d)^2 v_x^2 + k_y^2 v_y^2} \qquad (3.4)$$
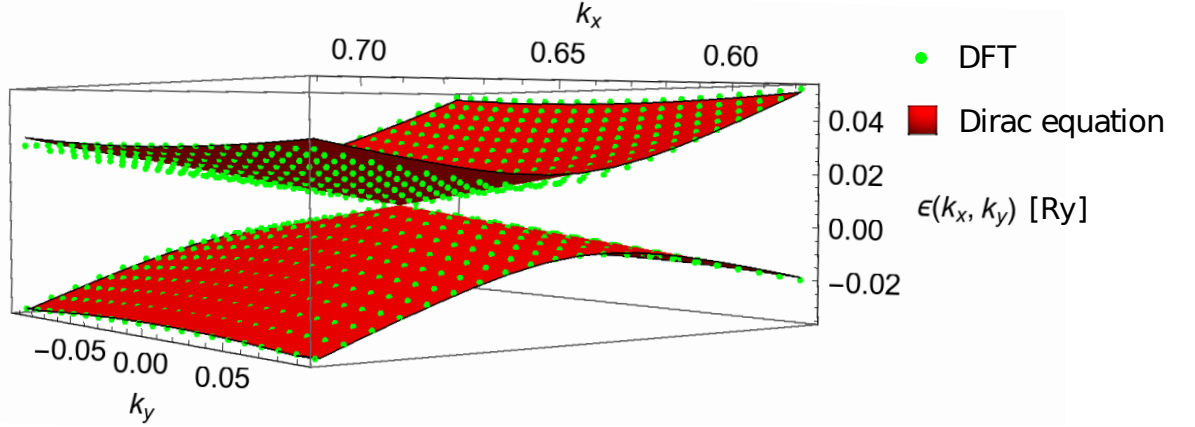


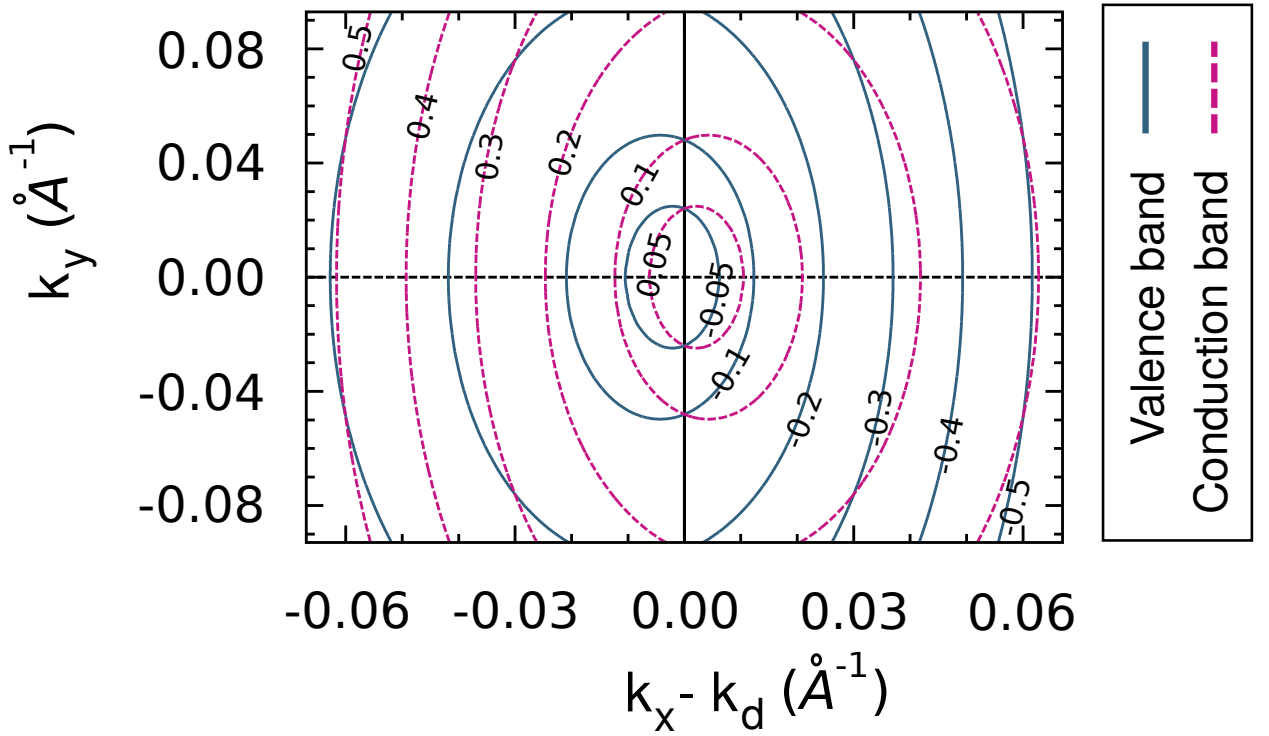Figure 3.4: The fitted dirac cone for borophane.



Figure 3.5: Contour plot of conduction (red colour) and valence (blue colour) bands around the Dirac cone for borophane. Values of the contours are in eV.

where $v_x = 19.58 \times 10^5 m/s$, $v_y = 6.32 \times 10^5 m/s$, $v_t = -5.06 \times 10^5 m/s$. A contour plot of the anisotropic Dirac cone is depicted in Fig. 3.5. The velocities in the positive and negative x-direction are given, respectively, by $v_x + |v_t| = 24.64 \times 10^5 m/s$ and $v_x - |v_t| = 14.52 \times 10^5 m/s$. $v_x + |v_t|$, $v_x - |v_t|$ and $v_y$ are 2.95, 1.74 and 0.76 times the Fermi velocity of graphene ($v_f = 8.36 \times 10^5 m/s$). The density of states per unit cell, derived from Eq. (3.3), is represented in Fig. 3.6 which is compared with the results obtained for graphene [95]. Despite of the different shape of the Brillouin zone of borophane and graphene, they have approximately the same area and also the same number of Dirac cones per unit cell. The average of the Fermi velocities for low-energy fermions for borophane are higher than that of graphene. That is why the number of possible occupied states are less than that of graphene per unit cell. It
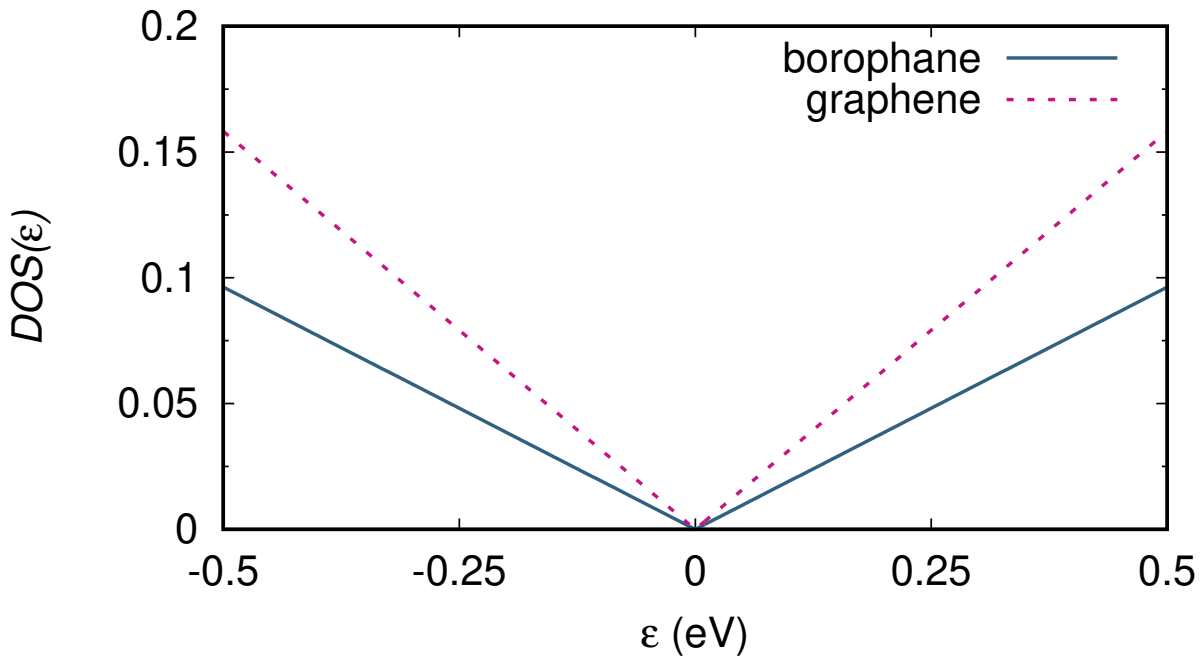


Figure 3.6: Density of states per unit cell as a function of energy calculated from the low-energy Dirac hamiltonian for borophane and graphene.

is possible to derive an analytical expression for the Green's function and extract the imaginary part of it in order to calculate the density of states (see Appendix A for more details). The density of states per unit cell corresponding

to the energy dispersion (3.4) can be calculated as follows

$$DOS(\varepsilon) = \frac{4\pi v_x^2}{\Omega v_y (v_x^2 - v_t^2)^{\frac{3}{2}}} |\varepsilon| \Theta(\varepsilon_c - |\varepsilon|) \qquad (3.5)$$

where $\Omega$ is the area of the Brillouin zone. The parameter $\varepsilon_c$ is a cut-off for the energy to make sure that Eq. (3.5) is valid within the linear regime of the band structure near the Dirac cones.

## 3.3 Band-Structure Dependent Properties of borophane

Thermoelectric properties of solids have attracted interests because of the capability of direct convertion of heat flux into electricity or reversely through the Seebeck effect and Peltier effect. The conversion efficiency of a thermoelectric material can be expressed by the power factor which is one of the spects of materials choice to determine the usefulness of the material examined in a thermoelectric cooler or a thermoelectric generator. Despite the gap between theory and practice, by calculating the semi-classical band-structure dependent quantities one can phenomenologically get a perspective of the desired material to prognose a sufficiently high thermoelectric performance. [96]

It is helpful to make a conformity assessment between the DFT approach and the tight-binding model described in section 6.3. So we present the thermoelectric properties of borophane using both first principle calculations and tight-binding approximation. Thermoelectric properties of the system have been calculated using BoltzTraP [97] code with an interface to Quantum Espresso [98] with the same inputs as mentioned in section 6.3 using projector-augmented-wave (PAW) [99], but with a dense $k$ mesh for the reciprocal Brillouin zone.

Semi-classical transport coefficients such as Seebeck coefficient and electrical conductivity were calculated under the constant relaxation time ($\tau$) approximation which is the most often used in praxis [100], at temperature $300(K)$. Substitution and doping are used to manipulate the chemical potential ($\mu$) which plays an important role on the thermoelectric transport

properties [101]. Fig. 3.7 depicts the values of the number of carriers ($n$), conductivity $\sigma/\tau$, Seebeck coefficient $S$ and power factor $S^2\sigma/\tau$ in terms of chemical potential.
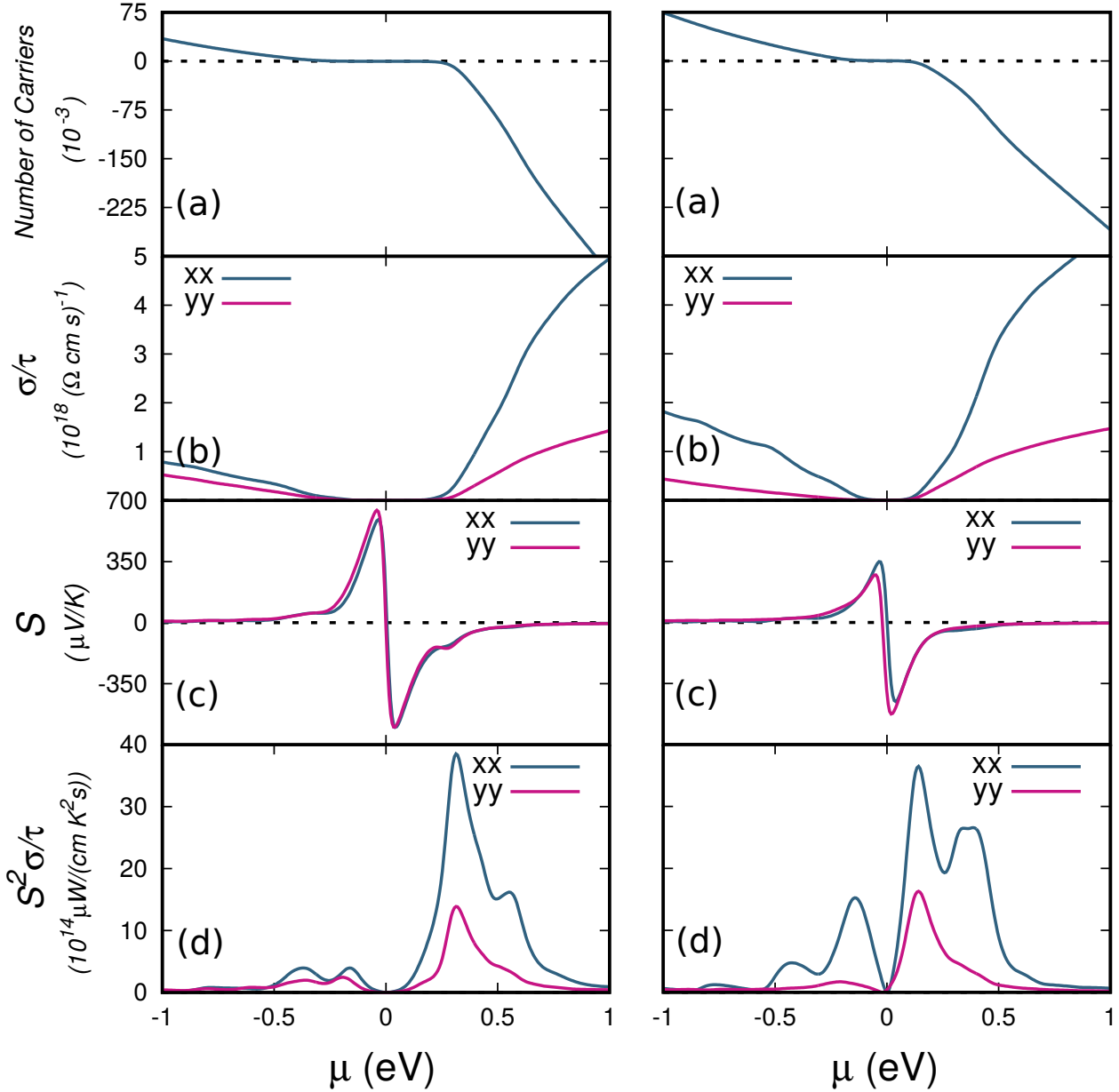


Figure 3.7: Transport coefficients as a function of chemical potential: (a) Number of carriers, (b) Electrical conductivity, (c) Seebeck coefficient and (d) Power factor with respect to relaxation time for both DFT approach (left side) and tight-binding model (right side).

We have used the Slater-Koster parameters for borophane (Tables 3.1 and 3.2) and used the same $k$ mesh to evaluate the transport coefficients scaled to scattering time. The first note to point out is that, as illustrated in
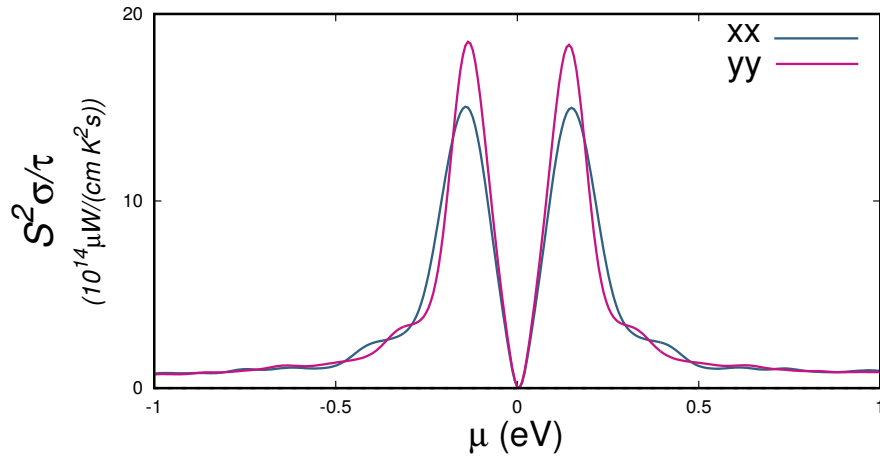
Figure 3.8: The Power factor of Graphene sheet with respect to relaxation time.

Fig. 3.7, these curves for the tight-binding model is in agreement with the density functional theory which demonstrates that the model is constructed and fitted adequately throughout the Brillouin zone. A comparison between the results of borophane and Graphene (Fig. 3.8) has been made which shows that the power factor of borophane in $x$ direction is approximately 2 times of that of graphene, but lower in $y$ direction. As an explanation for the order of the curves one should consider the relations between the Fermi velocities as aforementioned in Section 3.2. Fig. 3.7 (d) reveals that borophane in $x$ direction is able to generate more energy regardless of whether it has enough efficiency or not.

## 3.4 Data Availability

The supporting information and several examples are available at *tight-binding.com*. The examples and the supporting codes in additional programming languages, i.e. Matlab, Mathematica, Python, C, C++ and Fortran are also accessible through Code Generator tools in TBStudio.

# DIRAC NODAL LINE IN BILAYER BOROPHENE

Newly discovered Dirac [102, 103], Weyl [104–107], and nodal line semimetals [108–110] have resulted in novel states of matter. Nodal line semimetals can be considered as precursor states for other topological states intermediate between insulators and metals. The valence and conduction bands in topological semimetals touch at either discrete points or extended lines, forming respectively Dirac or Weyl semimetals and nodal line semimetals. Topologically nontrivial surface states are one of the characteristic features of topological insulators that are protected by time reversal symmetry. Band degeneracy points or lines in topological semimetals are also protected by symmetries and are thus robust against external perturbations. Recently, alongside the traditional topological insulators, topological semimetals attracted tremendous research interest.

Nodal line semimetals are observed in several bulk materials, such as body-centered orthorhombic $C_{16}$ [111] and hcp alkali earth metals [112] and recently, also in some 2D materials [113] like black phosphorus under pressure [114]. It turns out that there are many materials showing these topological states ranging from hyper-honeycomb lattices [115] and 3D-honeycomb lattices [116] to high-temperature super-conductions [117–119] and nearly flat drumhead-like surface states [120]. There are a number of reports on the existence of two concentric Dirac nodal loops centred around one point in reciprocal space [73] or a single nodal line as found in $CaP_3$ [121], $Ca_3P_2$

[122], $(Tl,Pb)TaSe_2$ [123].

Several novel properties have been predicted for nodal line semimetals, including special collective modes [124], and unique Landau levels [125]. The nodal line structure can also be considered as precursor states for different topological states. For instance, a nodal line semimetal can be converted to Weyl nodes [126–129] by taking spin-orbit coupling into account or the evolution of nodal rings into Dirac nodes and converting the nodal line semimetal into a topological insulator by opening a gap [130].

Two-dimensional (2D) materials have also attracted the interest of scientists because of the possibility of applications in high-speed nano-devices due to their special electronic properties. The realization of 2D topological semimetals will provide new platforms for the design of novel quantum devices at the nanoscale. In contrast to three-dimensional topological Dirac semimetals, the nodal lines in many 2D materials such as monolayer hexagonal lattices [131] and honeycomb-kagome lattices [113] are protected by mirror symmetry and require negligible spin orbit coupling [132]. Notwithstanding the lack of experimental realization of such structures up to now there is still a need to predict new 2D materials with nodal lines that can be fabricated.

Recently, 2D boron sheets (called borophene) have been successfully synthesized on a silver crystal by physical vapor deposition [73–77]. The boron-based materials show different metallic [133], semimetallic [134], and semiconducting [135] behaviors. Boron atoms have four available orbitals with three occupied valence electrons and because of electron-deficiency can form both covalent and ionic bonds. Various allotropes of boron-based structures can be formed such as clusters, nanotubes, 2D structures and bulk materials [136–138]. Using density functional theory (DFT) and global minimum search optimization method we are able to predict stable 2D bilayer borophene consisting of B6mmm sheets that are bound together by pillars. Phonon dispersion calculations reveal that this structure is dynamically stable [139] and therfore has the potential to be successfully synthesised for practical applications. Fig. 4.1 shows the structure of bilayer borophene B6mmm. The hexagon unit cell includes six atoms and the vectors **a** and **b** are the translational unit cell vectors that make a 120 degree angle. In the center of unit

cell there are two atoms that form a pillar between the two layers. Most importantly, the B6mmm structure exhibits a Dirac nodal line with a Fermi velocity comparable to that of graphene.

Efforts to search for potentially stable boron-based sheets with low energy and novel electronic properties are of great interest. In this paper, we report on Dirac nodal line fermions in B6mmm borophene bilayer based on first principles calculations and construct a tight-binding model via the Slater and Koster (SK) method [35] to reproduce the band energies calculated by DFT. The SK scheme is a powerful method based on the linear combination of atomic orbitals (LCAO) method. The Dirac nodal line in B6mmm forms a loop centred around the $K$ point in reciprocal lattice with dispersion in energy. Also we present a four band effective low-energy Hamiltonian to describe the nodal line which can be used as a new platform to study the novel physical properties of such two-dimensional Dirac nodal semimetals. Our results provide new opportunities to understand the nodal line structure and surface states and can be used to realize high-speed spin-less devices.

## 4.1 Electronic Structure Using DFT

The electronic properties of B6mmm are investigated by first-principles calculations using the OpenMX package [37]. Atomic structure relaxations and calculations of electronic band-structure were performed within the linear combination of pseudo-atomic orbitals (LCPAO) method [92]. Structure relaxations were carried out with the thershold $10^{-5}eV/A$ for the maximum value of the forces between the boron atoms. The generalized gradient approximation was applied for the exchange-correlation energy, using the Perdew, Burke, and Ernzerhof (PBE) functional [93, 94] with a cutoff energy of 400 eV for the plane-wave basis. Numerical integrations in the Brillioun zone were evaluated with the Monkhorst-Pack mesh ($12 \times 12 \times 1$).

After structure relaxation the lattice constant was calculated as $|\mathbf{a}| = |\mathbf{b}| = 2.85$Å with $\theta_{\mathbf{ab}} = 120°$ which are in agreement with a recent work [139]. This structure includes two honeycomb lattice at the top and the bottom layers which are connected through pillars. Thus the two layers of bilayer borophene
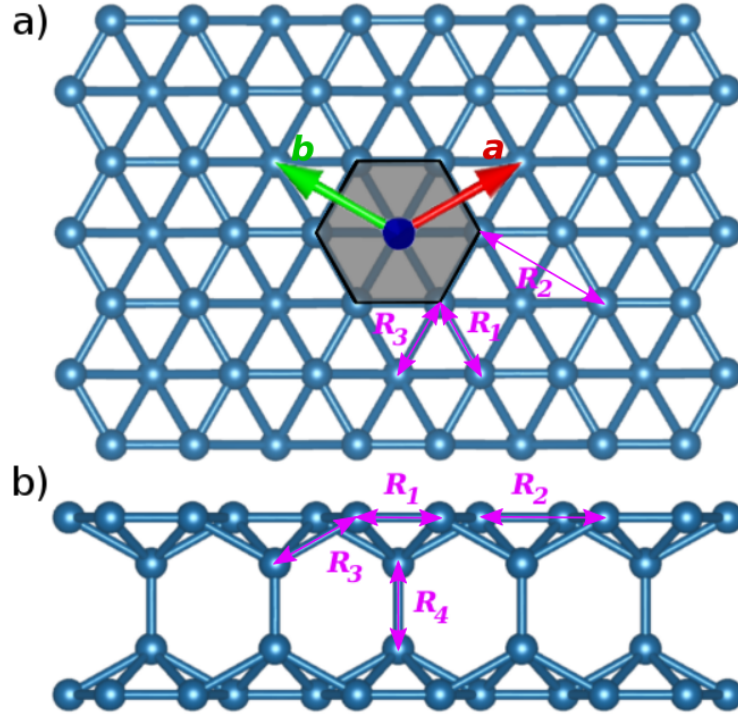
Figure 4.1: Top (a) and side (b) views of the structure of bilayer borophene B6mmm. The gray hexagon area is the primitive cell. The vectors $a$ and $b$ denote the translational vectors of the crystal lattice.

are chemically bound together in contrast to bilayer graphene which are hold together by only weak van der Waals forces. After optimizing the atomic positions one finds the distances $R_1 = 1.65\text{Å}$, $R_2 = 2.85\text{Å}$, $R_3 = 1.89\text{Å}$ and $R_4 = 1.70\text{Å}$. The bandstructure of B6mmm is displayed in Fig. 4.2. The contributions of the orbitals $s$, $p_x$, $p_y$ and $p_z$ are shown by different colors. Blue and red circles illustrate the location of two Dirac cones which are related to the electrons and holes, respectively. The nodal line is created by the intersection of two Dirac cones formed by the $p_z$ orbital centered at the point $K$ in the Brillouin zone.
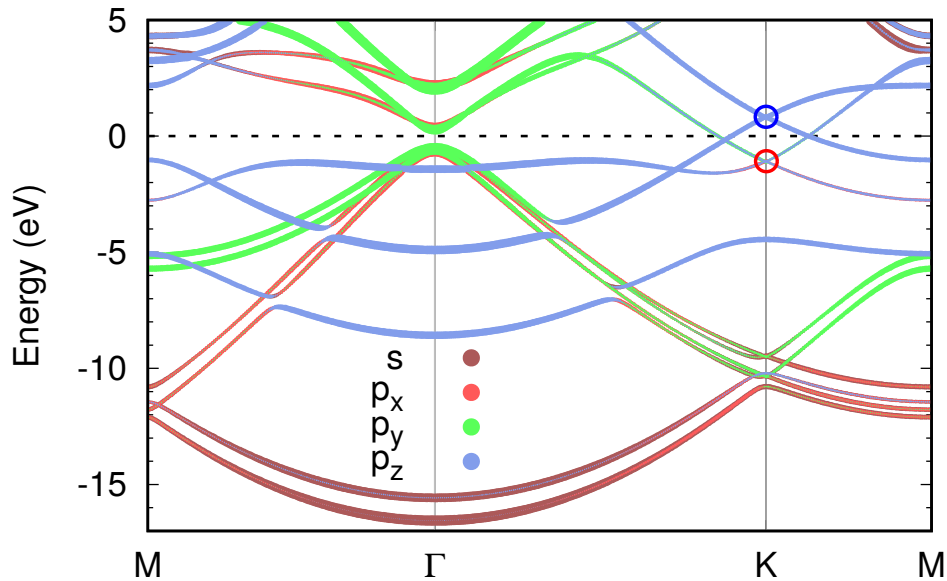
Figure 4.2: The bandstructure of B6mmm showing the contribution of different orbitals by the different colors. Blue and red circles show the Dirac cones which are related to the electrons and holes, respectively.

## 4.2 Tight-binding model and comparison with DFT calculations

For future purposes we develop a tight-binding model to reproduce the DFT band energies. We include the potentials of atoms on each layer which can be only sensed by the neighboring atoms in the same layer and electrons can hop between layers only through the pillars. To construct a TB model we consider the following matrix elements [88]

$$H_{iv,i'v'} = <\phi_v(r - r_i)|H|\phi_{v'}(r - r_{i'})>,$$
$$S_{iv,i'v'} = <\phi_v(r - r_i)|\phi_{v'}(r - r_{i'})> . \tag{4.1}$$

Here $H$ is the single electron Hamiltonian and $S$ is the overlap matrix resulting from the non-orthogonal basis functions [89–91]. The integrals are evaluated over the unit cell in real space and $i$ and $v$ run over all atoms in the unit cell and the orbitals $s$, $p_x$, $p_y$ and $p_z$, respectively. The eigen energy equation for a single electron can be written as follows

$$\sum_{v'}\sum_{i'}[H_{iv,i'v'} - \epsilon_k S_{iv,i'v'}]c_{i'v'}(k) = 0 . \tag{4.2}$$

The interatomic matrix elements found by fitting the known band energies [140]. The matrix elements can be represented by the expectation values of the Hamiltonian in the basis of the directed orbitals in terms of eight integrals $(v_{ss\sigma}, v_{sp\sigma}, v_{pp\sigma}, v_{pp\pi}, s_{ss\sigma}, s_{sp\sigma}, s_{pp\sigma}, s_{pp\pi})$ defined as follows

$$< s|H|s > = v_{ss\sigma},$$
$$< s|H|p_i > = n_i v_{sp\sigma},$$
$$< p_i|H|p_j > = (\delta_{ij} - n_i n_j) v_{pp\pi} + n_i n_j v_{pp\sigma}. \qquad (4.3)$$

Note, one should use the rule of angular quantum number: $< l|H|l' > = (-1)^{l+l'} < l'|H|l >$ to evaluate the complex conjucate hopping matrix elements. In Eq. (4.3) $n_i$ is the directional cosines defined by the following equation

$$n_i = \frac{\mathbf{r} . \mathbf{e}_i}{|\mathbf{r}|} \qquad (4.4)$$

where $\mathbf{r}$ is the vector along the corresponding bond and $i$ runs over different Cartesian directions ($x$, $y$ and $z$). For the overlap matrix the corresponding expressions can be found by replacing $H$ by $S$ and $v$ by $s$ in Eq. (4.3). The unknown parameters are determined by a best fitting of the energy bands that are obtained by the DFT method. We calculate the values of the eight integrals up to distances of the three nearest neighbor sites in each layer and for the pillars between layers.

B6mmm lattice is a structure with a basis of six boron atoms. We assume a basis containing one atomic-like $s$ and three $p_x$, $p_y$ and $p_z$ orbitals per atom, which generates a band structure with 24 bands. However, we will concentrate to find a satisfactory fitting for the first 11 bands. To calculate the TB Hamiltonian by using the eight Slater-Koster integrals one needs the distances and the directional cosines in Eq. (4.3) for the different bonds which we obtained from DFT. The distance between the boron atoms, $R_i$, correspond with different types of bonds are shown in Fig. 4.1.

Using the Levenberg-Marquardt nonlinear fitting algorithm [86] we find the optimal Hamiltonian and overlap matrices. The Slater-Koster coefficients for the differrent boron-boron bonds are given in Table 4.1 and the on-site energies for the boron atoms in Table 4.2. The full Hamiltonian and overlap matrices are given in Appendix B.

| $R$ | $V_{ss\sigma}$ | $V_{sp\sigma}$ | $V_{pp\sigma}$ | $V_{pp\pi}$ | $S_{ss\sigma}$ | $S_{sp\sigma}$ | $S_{pp\sigma}$ | $S_{pp\pi}$ |
|---|---|---|---|---|---|---|---|---|
| $R_1$ | -6.667 | 5.527 | 4.707 | -1.654 | 0.379 | -0.162 | 0.202 | 0.165 |
| $R_2$ | 0.100 | 0.092 | -0.150 | -0.1968 | 0.035 | -0.039 | -0.035 | 0.062 |
| $R_3$ | -0.974 | 1.792 | 2.869 | -1.333 | -0.126 | -0.007 | -0.293 | -0.143 |
| $R_4$ | 4.560 | -1.446 | -0.738 | 4.189 | -0.193 | -0.054 | -0.017 | -0.047 |

Table 4.1: The Slater-Koster parameters for B6mmm. The $V$ parameters are in $eV$, and the $S$ parameters are dimensionless.

| | $s$ | $p_x$ | $p_y$ | $p_z$ |
|---|---|---|---|---|
| **B** | -3.130 | 5.033 | 4.713 | 1.797 |

Table 4.2: The on-site energies of the boron atoms for the B6mmm structure in units of $eV$.

Using Eq. (4.3) with the coefficients presented in the Tables 4.1 and 4.2 one obtains the bandstructure shown in Fig. 4.3 which is compared to the band energies calculated by DFT. We made sure that the band structure is most accurately reproduced for small energies.
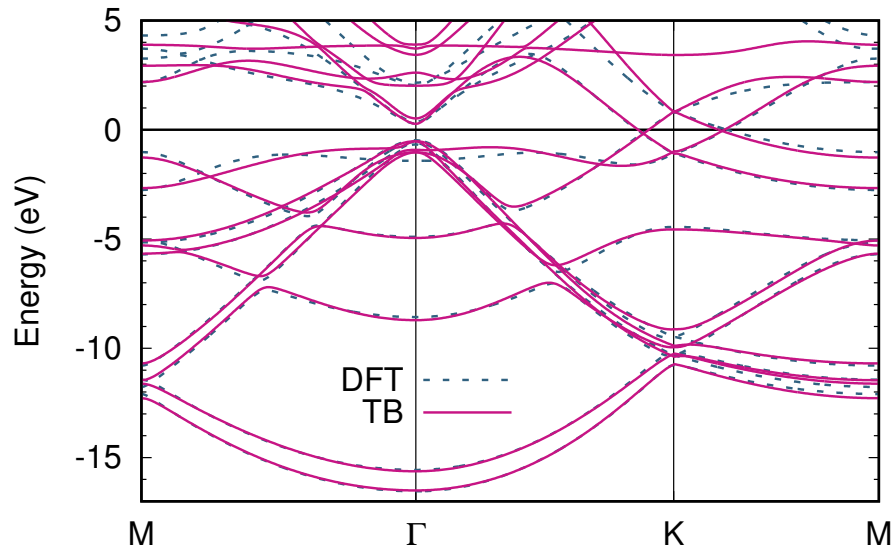


Figure 4.3: The fitted bandstructure of the TB model compared with the one obtained from DFT.

## 4.3   Effective low energy hamiltonian

The hexagonal Brillouin zone of the B6mmm has two inequivalent corners $K$ and $K'$. The four branches of its electronic spectrum form two Dirac cones at each $K$ point at different energies (See blue and red circles in Fig. 4.2). Fig. 4.4 shows the contour plot of the conduction and valence bands near the $K$ point. To recover the nodal line it is necessary to include the trigonal warping. As is apparent from Fig. 4.4 the conduction and valence bands have significant but opposite trigonal warping. To model the low energy spectrum around the $K$ point we use an effective mass and group velocity dependent hamiltonian model. The effective $4 \times 4$ model Hamiltonian near the $K$ point can be expressed in the following form [141–143]

$$H = \begin{pmatrix} \lambda & -\frac{\Pi^{\dagger 2}}{2m_e^*} + v_e\Pi & 0 & 0 \\ -\frac{\Pi^2}{2m_e^*} + v_e\Pi^\dagger & \lambda & 0 & 0 \\ 0 & 0 & -\lambda & -\frac{\Pi^{\dagger 2}}{2m_h^*} + v_h\Pi \\ 0 & 0 & -\frac{\Pi^2}{2m_h^*} + v_h\Pi^\dagger & -\lambda \end{pmatrix} \quad (4.5)$$

where $\Pi = p_x + i p_y$. $m_{e(h)}$ and $v_{e(h)}$ are respectively the effective mass and the group velocity of electrons and holes related to conduction and valence bands. The nodal line is formed by the intersection of two Dirac cones which are located above and below the Fermi level. The Dirac cones are related to the top and bottom honeycomb lattice layers and the energy shift between them is $2\lambda$. As is evident from Eq. (4.5) the block related to electrons is shifted by $\lambda$ and for holes is shifted by $-\lambda$. The low energy bands near the point $K$ are reproduced by taking $m_e = 0.174\hbar^2\text{Å}^{-2}eV^{-1} = 1.325m_0$, $m_h = 0.255\hbar^2\text{Å}^{-2}eV^{-1} = 1.942m_0$, $\hbar v_e = 4.744 eV\text{Å}$, $\hbar v_h = 6.184 eV\text{Å}$ and $\gamma = 0.992 eV$. Fig. 4.5 shows the valence and conduction bands as obtained from the Hamiltonian Eq. (4.5). By defining $k_x = k\cos\varphi$ and $k_y = k\sin\varphi$ we find the eigenvalues

$$E_c = \gamma - \frac{\hbar k}{2m_e}\sqrt{\hbar^2 k^2 + 4\hbar k m_e v_e \cos(3\varphi) + 4m_e^2 v_e^2} \quad (4.6)$$

$$E_v = -\gamma + \frac{\hbar k}{2m_h}\sqrt{\hbar^2 k^2 - 4\hbar k m_h v_h \cos(3\varphi) + 4m_h^2 v_h^2} \quad (4.7)$$

The intersection between the two bands defines the equation for the nodal line. After some simplifications we obtain the nodal line $k$ as a function of $\varphi$.

$$\hbar k(\varphi) = \frac{4\gamma}{v_e + v_h + \sqrt{\frac{4\gamma\cos(3\varphi)(m_e - m_h)}{m_e m_h} + (v_e + v_h)^2}} \quad (4.8)$$
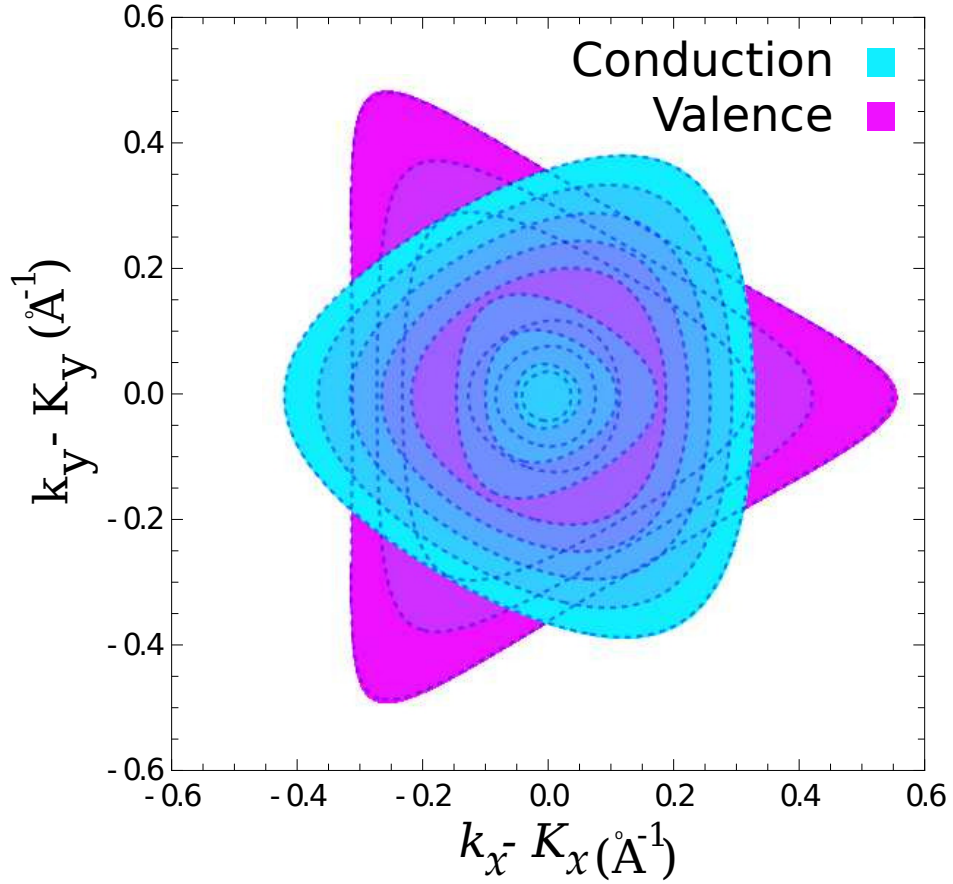
Figure 4.4: Contour plot of conduction and valence bands around the $K$ point.

This nodal line is presented in Fig. 4.5 by the red curve. The difference between maximum and minimum energy of the nodal line is $0.18eV$. Note that the different trigonal warping for valence and conduction bands is responsible for the breaking of the isoenergetic line and leads to form a non-flat nodal line with dispersion in energy.

One can find the velocities of electrons in conduction and valence band at the nodal line by taking respectively, the derivative of Eqs. (4.6) and (4.7) with respect to $k$. The equation gives us two different velocities which are related to the electrons inside (ie. holes) and outside (ie. electrons) the nodal line. Fig. 4.6 shows the velocities of electrons in B6mmm and graphene as a function of $\varphi$ in units of $m/s$ which reveals that the velocity of electrons is comparable to that of graphene. Note the difference between minimum and maximum of two velocities which is related to difference between trigonal warping directions shown in Fig. 4.4.
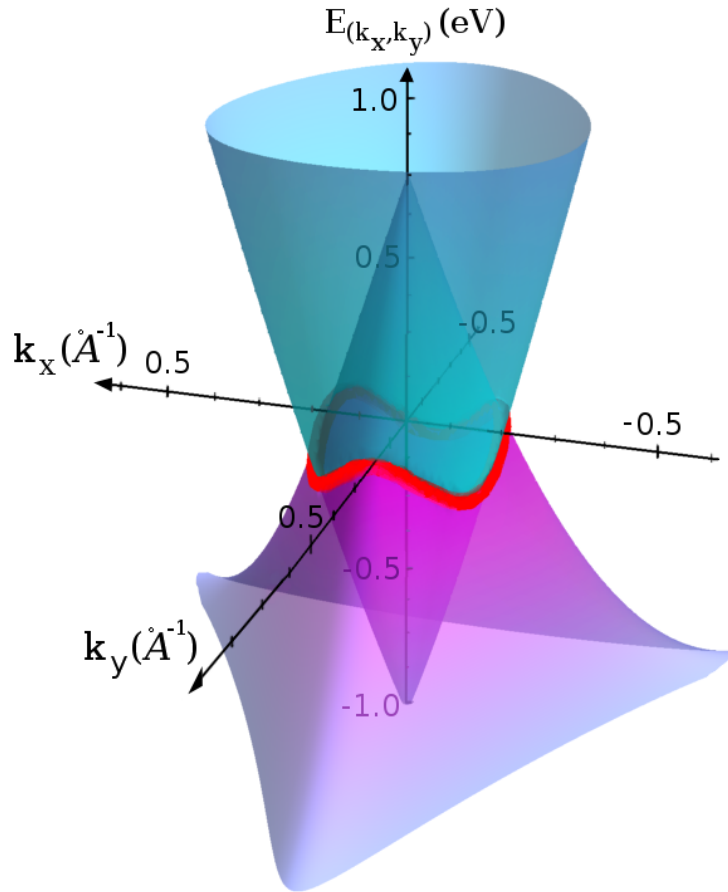
Figure 4.5: Valence and conduction bands. The solid red curve around the $K$ point shows the nodal line.

## 4.4   Data Availability

The supporting information and several examples are available at *tight-binding.com*. The examples and the supporting codes in additional programming languages, i.e. Matlab, Mathematica, Python, C, C++ and Fortran are also accessible through Code Generator tools in TBStudio.
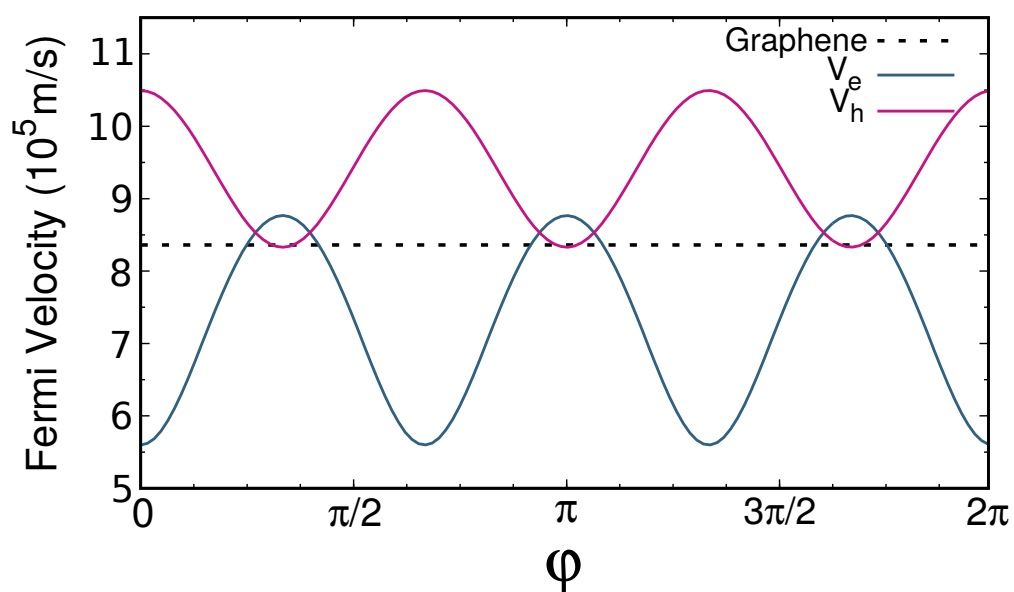
Figure 4.6: The Fermi velocity of the electrons (blue) and holes (red) at the nodal line. The dashed black horizontal line represents the velocity of electrons in graphene near the Fermi level.

# DIRAC NODAL LINES IN $Cu_2Si$ MONOLAYER

In the past decade, the discovery of topological insulators has ignited a lot of interest because of its unique physical properties [144, 145]. A characteristic feature of topological materials is the existence of topologically nontrivial surface states that are protected by time reversal symmetry. Recently, research interest has moved from traditional topological insulators to topological semimetals. In topological semimetals, the valence and conduction bands can touch at either discrete points or at extended lines, resulting in different semimetals. Three distinct kinds of topological semimetals exist: Dirac semimetals [146, 147], Weyl [148–151], and nodal line semimetals (NLS) [110, 152, 153] which have resulted in novel states of matter.

Nodal-line semimetals (NLSMs) are quantum materials with linear bands and symmetry-protected band degeneracies. NLSMs are three-dimensional graphene-like systems with low-energy relativistic excitations, but the bands touch as a closed loop in momentum space instead of points and the band crossing points form a continuous Dirac loop with a high density of states at the Fermi level. The surface states of nodal-line semimetals have drumhead-like surface flat bands. For example, the first Weyl semimetal phase discovered in the NbAs family [154–156] is rooted in nodal lines [157, 158]. Many kinds of three-dimensional (3D) nodal line bulk materials, such as $PtSn_4$ [159], $PbTaSe_2$ [160], and ZrSiS [161, 162], have been realized experimentally. A large number of theoretical studies exist [163–166] and numerous materials

have been predicted to show nodal line states: TlTaSe$_2$ [167], 3D-honeycomb graphene networks [110], Ca$_3$P$_2$ [168, 169], Cu$_4$PdN [170], and body-centered orthorhombic C$_{16}$ [171], [172, 174] Compared with 3D Dirac/Weyl semimetals, the band touching in NLSMs is not constrained to discrete points but extends along lines in the Brillouin zone (BZ). [152, 153, 173, 174] In contrast to the extended literature on 3D nodal line semimetals, the study of semimetal nodal line states in 2D materials is still in its infancy. The theoretical predictions of a nodal line band structure have been made for several 2D materials [175–177] but has only been confirmed experimentally for Cu$_2$Si monolayer. [178]

In this paper, firstly we investigate the Cu$_2$Si monolayer, which is composed of a honeycomb Cu lattice and a triangular Si lattice. In the free-standing form, all Cu and Si atoms are coplanar [178] and thus mirror reflection symmetry with respect to the x-y plane (M$_z$) is naturally expected. This is important for the existence of two-dimensional nodal lines. We use first principles calculations to obtain the single particle energy spectrum and construct a TB model via the Slater and Koster (SK) method [35] to reproduce the low energy bands around the Fermi energy. The SK scheme is a powerful method which is based on the linear combination of atomic orbitals (LCAO) method. Two Dirac nodal loops are found centred around the Γ point in reciprocal space with dispersion in energy. The gapless nodal loops are protected by mirror reflection symmetry. This intriguing band structures is accurately described by our TB model and both nodal loops survive in monolayer Cu$_2$Si even in the presence of a weak substrate-overlayer interaction. Our results provide new opportunities to understand nodal line structures and its corresponding surface states and can be used to realize high-speed spin-less devices.

## 5.1 Electronic structure: DFT

The electronic structure of Cu$_2$Si monolayer is calculated with geometric optimization using spin-polarized density functional theory (DFT) as implemented in the OpenMX Package. [37] This code finds the eigenvalues and

eigenfunctions of the Kohn-Sham equations self-consistently using norm-conserving pseudopotentials [179], and pseudoatomic orbitals (PAOs). [180, 181] In addition, we used the Perdew-Burke-Ernzerhof generalized gradient approximation (GGA) for exchange and correlation. [93] The **k**-points for sampling over the Brillouin zone (BZ) were generated using the Monkhorst-Pack scheme[182]. After convergence tests, we choose an energy cutoff of 300 Ry so that the total-energy converges below 1.0 meV/atom. In the first step, the atomic positions are optimized using a quasi-Newton algorithm for atomic force relaxation. The geometries were fully relaxed until the force acting on each atom was less than 1 meV/Å. The Brillouin zone (BZ) is sampled by a **k**-mesh grid of $23 \times 23 \times 1$ and scaled according to the size of the supercell. The $Cu_2Si$ monolayer is modelled as a periodic slab with a sufficiently large vacuum layer (20 Å) in order to avoid interaction between adjacent layers. In order to accurately describe the van der Waals (vdW) interaction in $Cu_2Si$, we adopted the empirical correction method presented by Grimme (DFT-D2), [183] which has been proven reliable for describing the long-range vdW interactions. Simulated scanning tunneling microscopy (STM) images were obtained using the Tersoff-Hamann theory [184] and were graphed using WSxM software [185].

The geometric atomic structure of $Cu_2Si$ monolayer, with its hexagonal primitive unit cell, indicated by the red parallelogram, is shown in Fig. 1(a). This structure contains 6 atoms per primitive unit cell in which P3m1 stands for the Space Group 164 included in the hexagonal crystal system. In $Cu_2Si$ with its 6-fold symmetry, each Si atom is coordinated with six Cu atoms and each Cu is coordinated with three Cu atoms and three Si atoms. After structure optimization the lattice constant was found 4.18Å, while the Cu-Si bond length and bond angels are 2.41 Å and 120°, respectively. These results are in agreement with a previous report.[178] Which also found, from the phonon dispersion that $Cu_2Si$ monolayer is dynamically stable. [178] The difference and total charge densities are shown in Fig. 1(b) and Fig. 1(c), respectively. The blue and yellow regions represent charge accumulation and depletion, respectively. The difference charge density shows a high charge density around the Si atoms, indicating charge transfer from Cu to Si atoms.
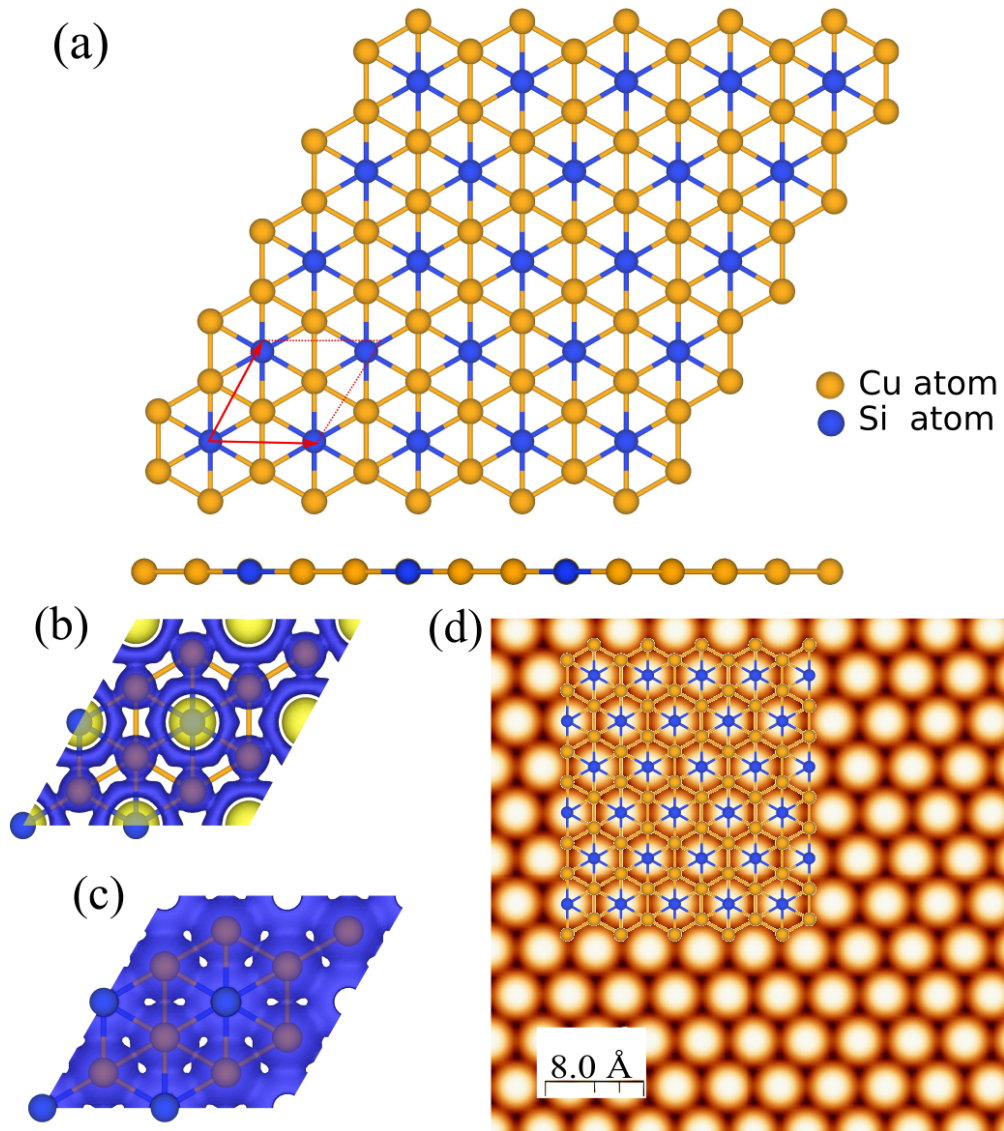
Figure 5.1: (a) Geometric atomic structure of Cu$_2$Si monolayer, with its hexagonal primitive unit cell indicated by the red parallelogram. Orange (blue) balls are Cu (Si) atoms. (b) Difference and (c) total charge densities. Blue and yellow regions represent charge accumulation and depletion, respectively. (d) Simulated STM image of Cu$_2$Si overlayered with the Cu$_2$Si lattice.

In order to provide visible guidance for experimental observations, first-principles DFT calculations were performed to calculate the STM image which is shown in Fig. 1(d). Our result shows that Si atoms are larger brighter spots than the Cu atoms. To correlate the STM image with the corresponding atomistic structure, we overlayered it with the Cu$_2$Si lattice structure.

The orbital-projected electronic band structure of Cu$_2$Si monolayer is shown in Fig. 2. The contributions of the orbitals $p_x$, $p_y$ and $p_z$ are shown by
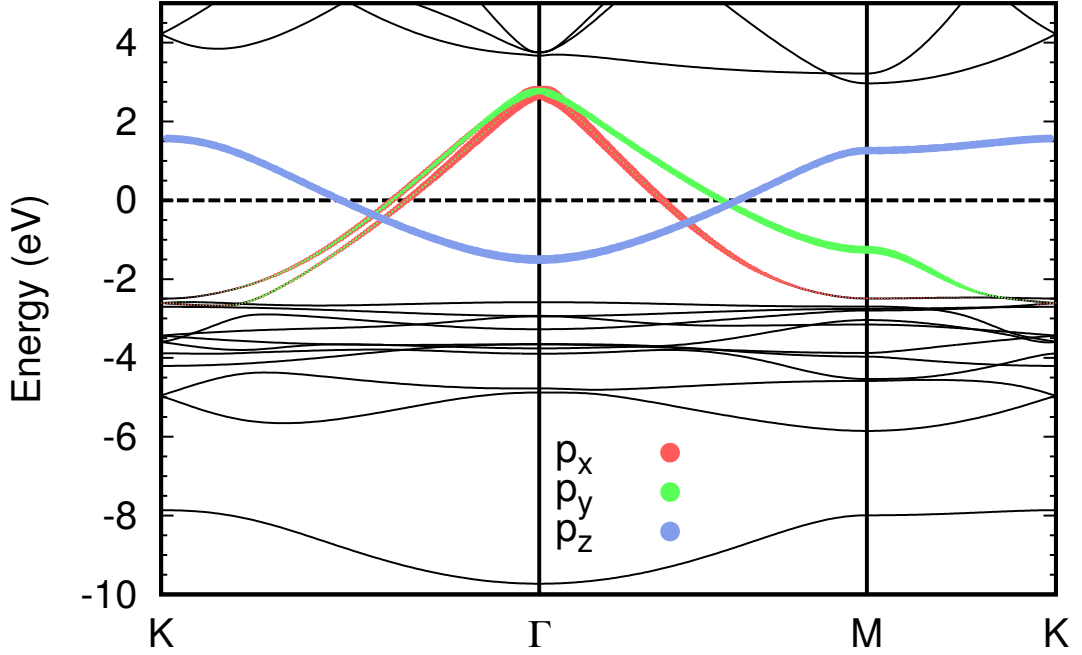
Figure 5.2: Orbital-projected electronic band structure of $Cu_2Si$ monolayer. The zero energy is set to the Fermi level energy (dashed-line).

different colors. Two nodal lines are created by the intersection of three bands formed by the $p_x$, $p_y$ and $p_z$ orbitals centered at the $\Gamma$ point in the Brillouin zone.

## 5.2 Tight-binding model

Now we construct a tight-binding model to reproduce the DFT band energies. We include only the potentials of atoms which are sensed by the neighboring atoms. To construct a TB model we consider the following matrix elements

$$H_{i\nu,i'\nu'} = <\phi_\nu(\mathbf{r}-\mathbf{r}_i)|H|\phi_{\nu'}(\mathbf{r}-\mathbf{r}_{i'})> . \tag{5.1}$$

Here $H$ is the single electron Hamiltonian and the integrals are evaluated over the unit cell in real space and $i$ and $\nu$ run over all atoms in the unit cell. We only take the orbitals $p_x$, $p_y$ and $p_z$ into account because we are searching for band energies near the Fermi level (see Fig. 2). The eigen energy equation for a single electron in the orthogonal basis can be written as follows

$$\sum_{v'}\sum_{i'}[H_{iv,i'v'}-\epsilon_k]c_{i'v'}(k)=0\,. \tag{5.2}$$

The interatomic matrix elements are found by fitting the known DFT band energies [186]. The matrix elements can be represented by the expectation values of the Hamiltonian in the basis of the directed orbitals in terms of four integrals ($v_{ss\sigma}$, $v_{sp\sigma}$, $v_{pp\sigma}$, $v_{pp\pi}$) defined as follows

$$
\begin{aligned}
<s|H|s> &= v_{ss\sigma}\,,\\
<s|H|p_i> &= n_i v_{sp\sigma}\,,\\
<p_i|H|p_j> &= (\delta_{ij}-n_i n_j)v_{pp\pi}+n_i n_j v_{pp\sigma}\,.
\end{aligned}
\tag{5.3}
$$

It should be noted that one needs to use the equation: $<l|H|l'>=(-1)^{l+l'}<l'|H|l>$ to evaluate the complex conjucate hopping matrix elements. In Eq. (5.4) $n_i$ is the directional cosines defined by the following equation

$$n_i = \frac{\mathbf{r}.\mathbf{e}_i}{|\mathbf{r}|}, \tag{5.4}$$

where $\mathbf{r}$ is the vector along the corresponding bond and $i$ runs over different Cartesian directions ($x$, $y$ and $z$). The unknown parameters are determined by a best fitting of the energy bands that are obtained by the DFT method. We calculate the values of the integrals up to distances of the first nearest neighbor sites.

The Cu$_2$Si lattice is a structure with a basis of two Cu and one Si atom. We assume a basis containing three $p_x$, $p_y$ and $p_z$ orbitals per atom, which generates a band structure with 9 bands. To calculate the TB Hamiltonian by using the eight Slater-Koster integrals one needs the distances and the directional cosines in Eq. (5.4) for the different bonds.

Using the Levenberg-Marquardt nonlinear fitting algorithm [187] we find the optimal Hamiltonian and overlap matrices. The Slater-Koster coefficients for the different copper-silicon bonds are given in Table 5.1 and the on-site energies for the atoms in Table 5.2.

Using Eq. (5.4) with the coefficients presented in Tables 5.1 and 5.2 one obtains the band structure shown in Fig. 5.3 which is compared to the band
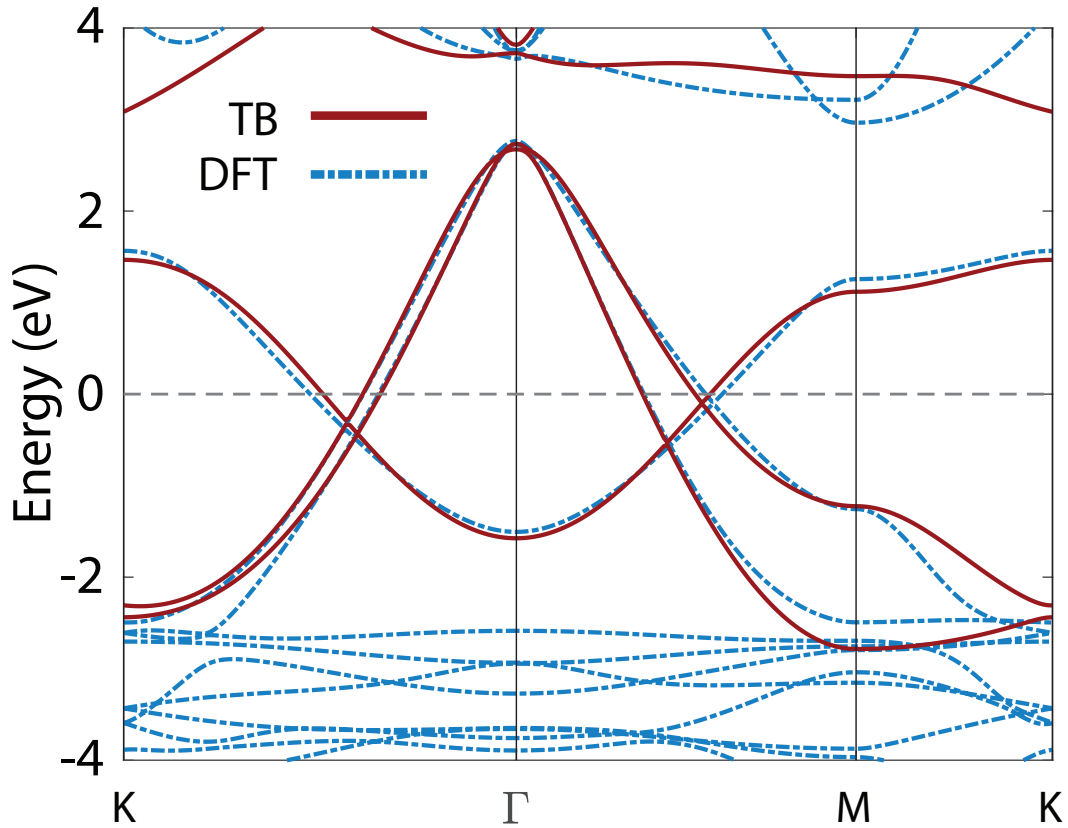
Figure 5.3: The fitted band structure of the TB model compared with the one obtained from DFT.

energies calculated by DFT. The tight-binding model closely fits the band-structure calculated by DFT in the energy range (-2,+2)eV and gives insight in its nodal line structure.

Most importantly, the $Cu_2Si$ structure exhibits two Dirac nodal lines with a Fermi velocity comparable to that of graphene. Fig. 5.4 shows a 3D plot of the band structure of $Cu_2Si$ calculated from the TB model near the Fermi level around the $\Gamma$ point. The non-flat thick curves are two nodal lines around the $\Gamma$ point which are enlarged in the inset zoom. Each nodal line exhibits a $0.22eV$ dispersion in energy. Fig. 5.5 shows the density plot of the second TB band. The blue contour line indicates the first nodal line which is due to the intersection between second and third TB bands and the red contour line is the second nodal line made of the crossing of the first and the second TB bands (see also Fig. 5.4).

To calculate the Hamiltonian and overlap matrix in terms of atomic orbitals we expand the Bloch functions as linear combinations of the orbitals
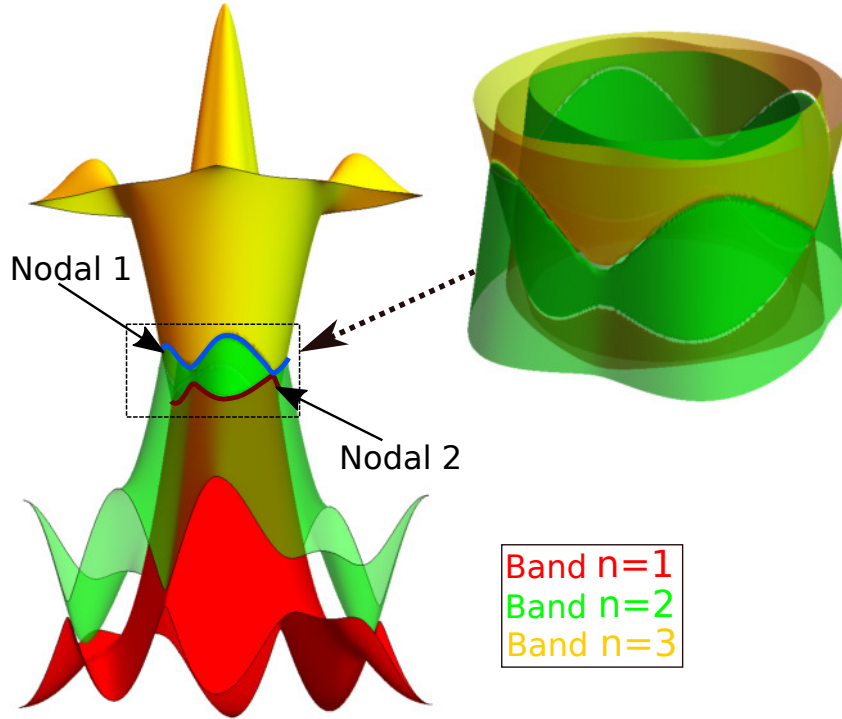
Figure 5.4: 3D plot of the band structure of Cu$_2$Si calculated by TB model near the Fermi level around the $\Gamma$ point.

Table 5.1: The Slater-Koster parameters for Cu$_2$Si in $eV$.

| bond type | $pp\sigma$ | $pp\pi$ |
|-----------|------------|---------|
| **Cu-Cu** | 0.360 | -0.516 |
| **Cu-Si** | -2.105 | 1.868 |

Table 5.2: The on-site energies of the copper and silicon atoms for the Cu$_2$Si structure in units of $eV$.

|      | $p_x$ | $p_y$ | $p_z$ |
|------|-------|-------|--------|
| **Cu** | 5.223 | 3.581 | 20.613 |
| **Si** | 2.849 | 3.054 | 1.467 |

$\varphi$ as follows

$$\psi_k(\mathbf{r}) = \sum_{v'} \sum_{i'} c_{i'v'}(k)\phi_{v,k}(\mathbf{r} - \mathbf{r}_i) \tag{5.5}$$

with

$$\phi_{v,\mathbf{k}}(\mathbf{r}) = \sum_{n\in\mathbb{Z}} \sum_{m\in\mathbb{Z}} e^{i\mathbf{k}.\mathbf{R}_{n,m}} \varphi_v(\mathbf{r} - \mathbf{R}_{n,m}) \tag{5.6}$$
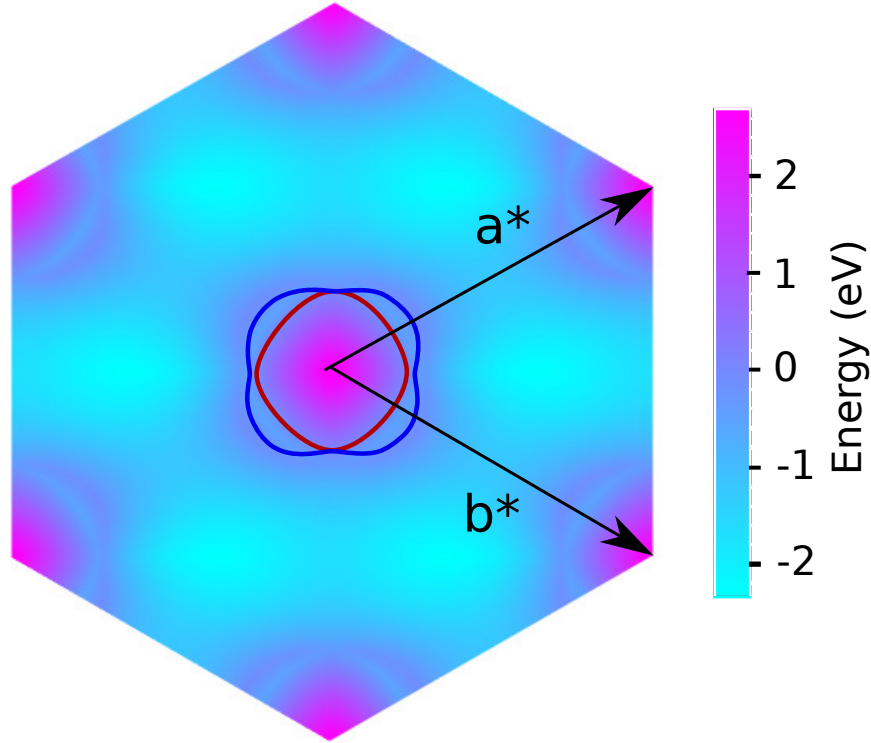
Figure 5.5: Density plot of the band $n = 2$ in first Brillouin zone. The blue and the red contours are the first and the second nodal lines. $a*$ and $b*$ are the reciprocal lattice unit vectors.

in which $\mathbf{R}_{n,m}$ is the discrete translation vector of the unit cell at $(m,n)$ of the Bravais lattice. In principle, $m$ and $n$ run over an infinite array of discrete points, in this work the TB model includes only the first nearest unit cell. In orthogonal TB modeling the overlap matrix $S$ is an identity matrix and the mono-electronic Hamiltonian $H$ may be rewritten as

$$\mathbf{H} = \sum_{n=-1}^{1} \sum_{m=-1}^{1} \mathbf{h}_{n,m} e^{i\mathbf{k}.\mathbf{R}_{m,n}}, \tag{5.7}$$

where $\mathbf{R}_{m,n}$ is the translation vector of the unit cell $(m,n)$. Since $\mathbf{H}$ is Hermitian therefore

$$\mathbf{h}_{-1,0} = \mathbf{h}_{1,0}^{\dagger}, \mathbf{h}_{0,-1} = \mathbf{h}_{0,1}^{\dagger},$$
$$\mathbf{h}_{-1,-1} = \mathbf{h}_{1,1}^{\dagger}, \mathbf{h}_{-1,1} = \mathbf{h}_{1,-1}^{\dagger}, \tag{5.8}$$

hence, we have only five independent matrices. We only need to determine the matrices $\mathbf{h}$ for the cells at $(0,0)$, $(1,0)$, $(0,1)$, $(1,1)$ and $(-1,1)$ and so the

other elements of the coupling matrices can be found from Eq. (5.8). Note that, in first nearest neighbor TB model for this structure there is no interaction between the primitive cell and the cell $(1,-1)$ and so $h_{1,-1}$ is zero. The SK values are presented in units of $eV$ and so the Hamiltonian matrix is also in eV. Since the number of atoms in the unit cell is 3 and each atom has 3 orbitals the Hamiltonian and the overlap matrix are of size $9 \times 9$. We use the SK coefficients presented in table 5.1 and calculate the Hamiltonian and extract respectively, the matrices $h_{0,0}$, $h_{1,0}$, $h_{0,1}$ and $h_{1,1}$ as follows

$$
\begin{array}{ccccccccc}
p_y & p_z & p_x & p_y & p_z & p_x & p_y & p_z & p_x
\end{array}
$$

$$
\begin{pmatrix}
3.05 & 0 & 0 & 0.87 & 0 & -1.72 & 0 & 0 & 0 \\
0 & 1.47 & 0 & 0 & 1.87 & 0 & 0 & 0 & 0 \\
0 & 0 & 2.85 & -1.72 & 0 & -1.11 & 0 & 0 & 0 \\
0.87 & 0 & -1.72 & 3.58 & 0 & 0 & -0.30 & 0 & 0.38 \\
0 & 1.87 & 0 & 0 & 20.61 & 0 & 0 & -0.52 & 0 \\
-1.72 & 0 & -1.11 & 0 & 0 & 5.22 & 0.38 & 0 & 0.14 \\
0 & 0 & 0 & -0.30 & 0 & 0.38 & 3.58 & 0 & 0 \\
0 & 0 & 0 & 0 & -0.52 & 0 & 0 & 20.61 & 0 \\
0 & 0 & 0 & 0.38 & 0 & 0.14 & 0 & 0 & 5.22
\end{pmatrix}
\begin{array}{c}
p_y \\ p_z \\ p_x \\ p_y \\ p_z \\ p_x \\ p_y \\ p_z \\ p_x
\end{array}
$$

$$
\begin{array}{ccccccccc}
p_y & p_z & p_x & p_y & p_z & p_x & p_y & p_z & p_x
\end{array}
$$

$$
\begin{pmatrix}
0 & 0 & 0 & 0 & 0 & 0 & 0 & 0 & 0 \\
0 & 0 & 0 & 0 & 0 & 0 & 0 & 0 & 0 \\
0 & 0 & 0 & 0 & 0 & 0 & 0 & 0 & 0 \\
0.87 & 0 & 1.72 & 0 & 0 & 0 & 0 & 0 & 0 \\
0 & 1.87 & 0 & 0 & 0 & 0 & 0 & 0 & 0 \\
1.72 & 0 & -1.11 & 0 & 0 & 0 & 0 & 0 & 0 \\
-2.11 & 0 & 0 & -0.30 & 0 & -0.38 & 0 & 0 & 0 \\
0 & 1.87 & 0 & 0 & -0.52 & 0 & 0 & 0 & 0 \\
0 & 0 & 1.87 & -0.38 & 0 & 0.14 & 0 & 0 & 0
\end{pmatrix}
\begin{array}{c}
p_y \\ p_z \\ p_x \\ p_y \\ p_z \\ p_x \\ p_y \\ p_z \\ p_x
\end{array}
$$

|        | $p_y$ | $p_z$ | $p_x$ | $p_y$ | $p_z$ | $p_x$ | $p_y$ | $p_z$ | $p_x$ |       |
|--------|-------|-------|-------|-------|-------|-------|-------|-------|-------|-------|
| ⎛      | 0     | 0     | 0     | 0     | 0     | 0     | 0     | 0     | 0     | ⎞ $p_y$ |
|        | 0     | 0     | 0     | 0     | 0     | 0     | 0     | 0     | 0     | $p_z$ |
|        | 0     | 0     | 0     | 0     | 0     | 0     | 0     | 0     | 0     | $p_x$ |
|        | −2.11 | 0     | 0     | 0     | 0     | 0     | 0     | 0     | 0     | $p_y$ |
|        | 0     | 1.87  | 0     | 0     | 0     | 0     | 0     | 0     | 0     | $p_z$ |
|        | 0     | 0     | 1.87  | 0     | 0     | 0     | 0     | 0     | 0     | $p_x$ |
|        | 0.87  | 0     | 1.72  | 0.36  | 0     | 0     | 0     | 0     | 0     | $p_y$ |
|        | 0     | 1.87  | 0     | 0     | −0.52 | 0     | 0     | 0     | 0     | $p_z$ |
| ⎝      | 1.72  | 0     | −1.11 | 0     | 0     | −0.52 | 0     | 0     | 0     | ⎠ $p_x$ |

|        | $p_y$ | $p_z$ | $p_x$ | $p_y$ | $p_z$ | $p_x$ | $p_y$ | $p_z$ | $p_x$ |       |
|--------|-------|-------|-------|-------|-------|-------|-------|-------|-------|-------|
| ⎛      | 0     | 0     | 0     | 0     | 0     | 0     | 0     | 0     | 0     | ⎞ $p_y$ |
|        | 0     | 0     | 0     | 0     | 0     | 0     | 0     | 0     | 0     | $p_z$ |
|        | 0     | 0     | 0     | 0     | 0     | 0     | 0     | 0     | 0     | $p_x$ |
|        | 0     | 0     | 0     | 0     | 0     | 0     | 0     | 0     | 0     | $p_y$ |
|        | 0     | 0     | 0     | 0     | 0     | 0     | 0     | 0     | 0     | $p_z$ |
|        | 0     | 0     | 0     | 0     | 0     | 0     | 0     | 0     | 0     | $p_x$ |
|        | 0.87  | 0     | −1.72 | 0     | 0     | 0     | 0     | 0     | 0     | $p_y$ |
|        | 0     | 1.87  | 0     | 0     | 0     | 0     | 0     | 0     | 0     | $p_z$ |
| ⎝      | −1.72 | 0     | −1.11 | 0     | 0     | 0     | 0     | 0     | 0     | ⎠ $p_x$ |

# 5.3   Data Availability

The supporting information for tight-binding model and its results are available in TBStudio software developed based on the Slater-Koster method. The software has been made available at tight-binding.com. The results of b-AsP is accessible in example folder of TBStudio. The supporting codes are gives in additional programming languages i. e. Matlab, Mathematica, Python, C, C++ and Fortran which are also accessible through Code Generator tools in TBStudio.

# GALLENENE $a_{100}$ AND $b_{010}$ MONOLAYERS

Following the successful synthesis of graphene [188, 189] from its bulk crystal, graphite, two-dimensional (2D) materials have gained a lot of interest in nanodevice applications owing to their extraordinary properties [190–193]. In recent years, researchers have paid special attention to the synthesis of monolayers of other mono-atomic crystals such as silicene [194–196], germanene [197–200], stanene [201, 202], phosphorene [203] and borophene [204] due to their specific electronic properties [205–209].

A wide range of 2D materials ranging from graphene to topological insulators [67–72] share the extraordinary phenomenon that electrons behave as relativistic particles in their low-energy excitations. This emergent behavior of fermions in condensed matter systems has been classified as "Dirac materials" which have attracted both experimental and theoretical interest. Recently, fully metallic gallium-based 2D crystals, named as 'Gallenene' have been synthesized on different substrates [210].

Gallium is a metallic element and it is known to exhibit metallicity in its bulk crystal [211]. It was also reported to be a non-toxic liquid metal at room temperature [212, 213]. In its bulk form, gallium exhibits various types of phases such as boron-like molecular and close-packed metallic which are known to exist under non-standard pressure and temperature [212, 214, 215]. Moreover, the extreme covalent bonding character of the $Ga_2$ pairs causes the pairs to exhibit dimer-like behavior. The $\alpha$-Ga, a phase of bulk-gallium, is

known as the only one which reveals both metallic and molecular character at zero pressure [212, 216, 217].

We construct a tight-binding (TB) model whose parameters are determined through a nonlinear fitting algorithm of the energy bands that are obtained by *ab-initio* methods. The TB model can provide us the hoppings and overlaps between different orbitals of the atoms. The Slater and Koster scheme (SK) [35] and the Naval Research Laboratory (NRL) method [85], as an extension of the SK approach, are two powerful methods for reproducing the first-principles data in terms of a set of non-interacting single-particles. The SK method gives the hopping between the orbitals for each bond separately while NRL also gives the hoppings as a function of distance up to a certain cut-off radius. In 1954 J. C. Slater and G. F. Koster [85] represented the expectation values of the matrix elements of the Hamiltonian in the basis of the directed orbitals in terms of eight integrals ($v_{ss\sigma}$, $v_{sp\sigma}$, $v_{pp\sigma}$, $v_{pp\pi}$, $s_{ss\sigma}$, $s_{sp\sigma}$, $s_{pp\sigma}$, $s_{pp\pi}$).

The understanding of electronic transport of materials is one of the interesting fields of research among 2D systems. A significant exploratory research in 2D materials has been done using Green's function theory for which we need the TB model. Here, we apply the SK method and present the coefficients for different bonds.

The Slater-Koster integrals for different Ga-Ga bonds are found up to the second nearest neighbors. The $b_{010}$-Gallenene structure is more compact than the $a_{100}$-Gallenene and consequently the orbitals are substantially different from the pure atomic like shape. Compaction of structures can affect significantly the overlap between orbitals and result in a non-unitary overlap matrix. $a_{100}$-Gallenene exhibits a graphene-like planar structure and can be modelled by an orthogonal basis while for the $b_{010}$-Gallenene a non-orthogonal basis set is needed.

## 6.1   Computational Methodology

For structural optimization and electronic-band structure calculations of monolayers of $a_{010}$- and $b_{100}$-Gallenene crystals, first principle calculations were performed in the framework of density functional theory (DFT) as im-

plemented in the Vienna *ab-initio* simulation package (VASP) [38–40]. The Perdew-Burke-Ernzerhof (PBE) [93] form of generalized gradient approximation (GGA) was adopted to describe electron exchange and correlation. The electronic-band structures were calculated at the GGA level.

The kinetic energy cut-off for plane-wave expansion was set to 500 eV and the energy was minimized until its variation in subsequent steps became $10^{-8}$ eV. The Gaussian smearing method was employed for the total energy calculations and the width of the smearing was chosen as 0.05 eV. Total Hellmann-Feynman forces in the primitive unit cell was reduced to $10^{-7}$ eV/Å for the structural optimization. $19 \times 19 \times 1$ $\Gamma$ centered $k$-point samplings were used in the primitive unit cells. To avoid interaction between the neighboring layers, our calculations were implemented with a vacuum space of 15 Å.

## 6.2 Structural and Electronic Properties

In this section, the structural and electronic properties of mono-atomic monolayers of gallium, $a_{100}$- and $b_{010}$-Gallenene, are discussed in detail. The optimized unit cell of each crystal structure has four Ga atoms as shown in Figs. 6.1(a) and (b). As mentioned by Kockat *et al.* [210], the relaxed crystal structures of both monolayers exhibit imaginary frequencies through the whole Brillouin Zone (BZ) which reveals the dynamical instability in their free-standing forms. However, it was also demonstrated that both of the monolayer crystals can be stabilized upon application of a biaxial strain (6% and 2% for $a_{100}$- and $b_{010}$-Gallenene, respectively). Therefore, in this work we consider biaxially straining, i.e. we investigate the dynamically stable structures, which can be realized by using an appropriate substrate.

The monolayer of $a_{100}$-Gallenene has a honeycomb structure with a rectangular primitive unit cell. The lattice constants $a$ and $b$ are found to be 7.87 and 4.65 Å, respectively. The Ga-Ga bond lengths are nearly equal because the two nearest neighbors of a Ga atom are both at 2.66 Å ($\delta_1$) and the third one is at 2.67 Å ($\delta_2$). These bond lengths are larger than those between other group-IV atoms in a group-IV mono-atomic monolayer that is attributed to the larger atomic radius of Ga. Moreover, different interior angles (122.43°

and 118.80° for $\theta_1$ and $\theta_2$, respectively) in $a_{100}$-Gallenene suggest that the hybridization in the crystal structure is not completely $sp^2$ despite the planar structure. Different from the 2-atom primitive hexagonal unit cell of graphene which belongs to the space group symmetry of $P\bar{6}/mmm$, the primitive unit cell of $a_{100}$-Gallenene is slightly distorted which belongs to $Pb$am space group symmetry. In addition, the point symmetry of $a_{100}$-Gallenene turns into $D_{2h}$ which is known to be $D_{6h}$ for graphene.

The monolayer $b_{010}$-Gallenene resembles a zigzag rhombic lattice which exhibits lower symmetry than $a_{100}$-Gallenene. The lattice constants $a$ and $b$ in this case are calculated to be 4.74 and 4.92 Å, respectively. The Ga-Ga bond length is 2.73 Å which is larger than that of $a_{100}$-Gallenene due to the buckled structure of $b_{010}$-Gallenene. In the quasi-2D multi-decker structure the vertical direction between Ga-dimers, or the buckling height, is calculated to be 1.19 Å. Such buckling can also be seen in other mono-atomic monolayer crystals such as silicene, germanene, stanene, and black phosphorus.
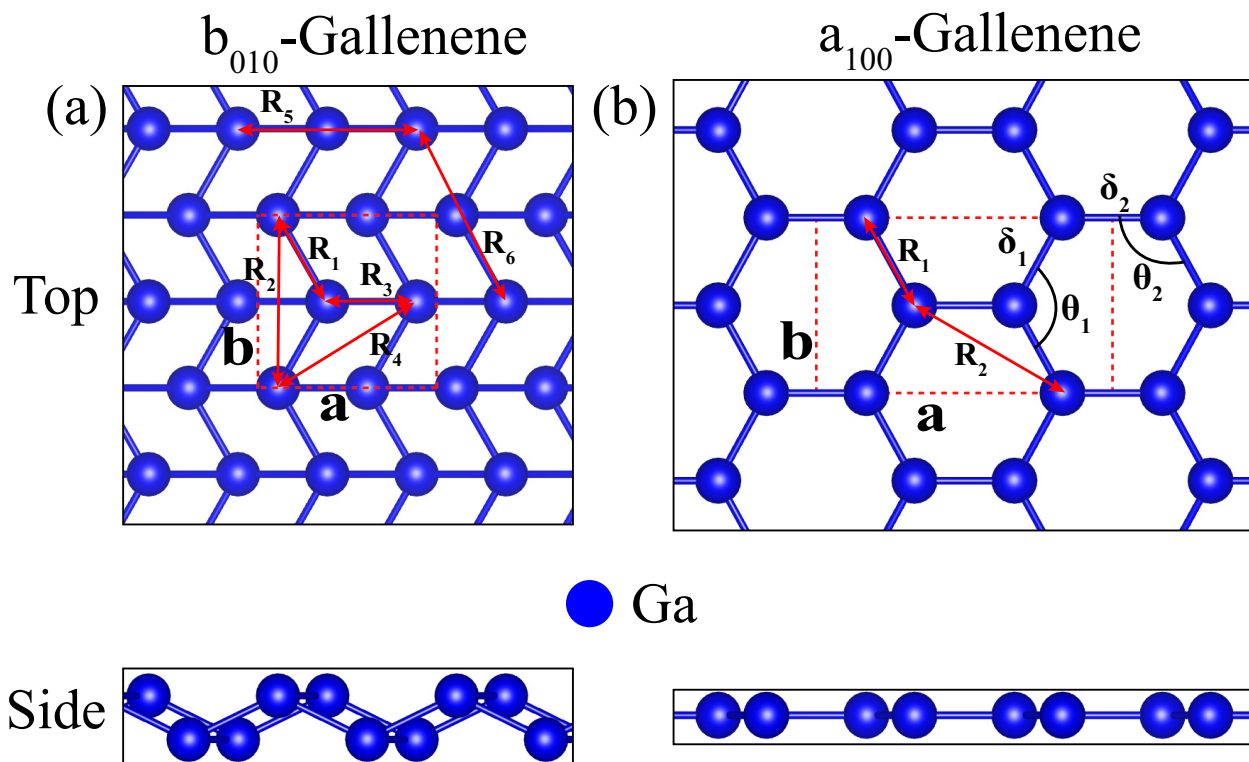


Figure 6.1: The optimized structure of (a) $a_{100}$-Gallenene and (b) $b_{010}$-Gallenene. The unit cell is given by the dotted box. $R_i$ denotes the distance between the Ga atoms.
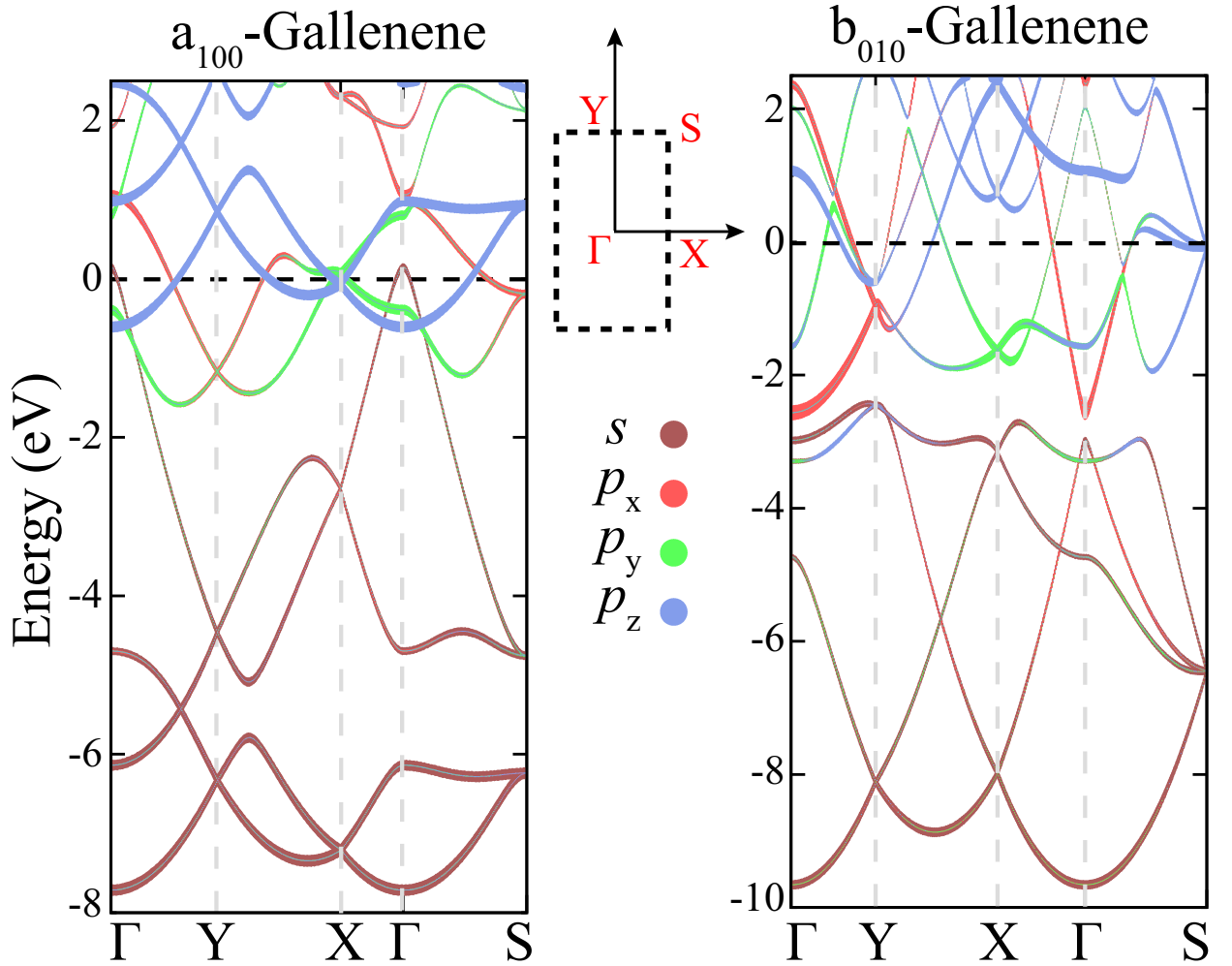
Figure 6.2: The electronic-band structure of $a_{100}$-Gallenene (left side) and $b_{010}$-Gallenene (right side). The different colors of the bands refer to the different orbital contribution. The dashed rectangle indicates the BZ with the high symmetry points.

In order to analyze the electronic properties of monolayers of $a_{100}$- and $b_{010}$-Gallenene, the orbital projected electronic-band structures are calculated within DFT-based methods (see Figs. 6.2(a) and (b)). It is clear that both monolayer crystals exhibit metallic character because of the finite number of bands crossing the Fermi level. As shown in Fig. 6.2(a), the unoccupied $p_z$ orbitals in planar $a_{100}$-Gallenene creates the bands which lie above the Fermi level. In the case of $b_{010}$-Gallenene, the $p_z$ orbitals are hybridized with the in-plane orbitals due to the buckled crystal structure. Therefore, the bands are highly dispersive in monolayer $b_{010}$-Gallenene.

## 6.3 Tight-binding model
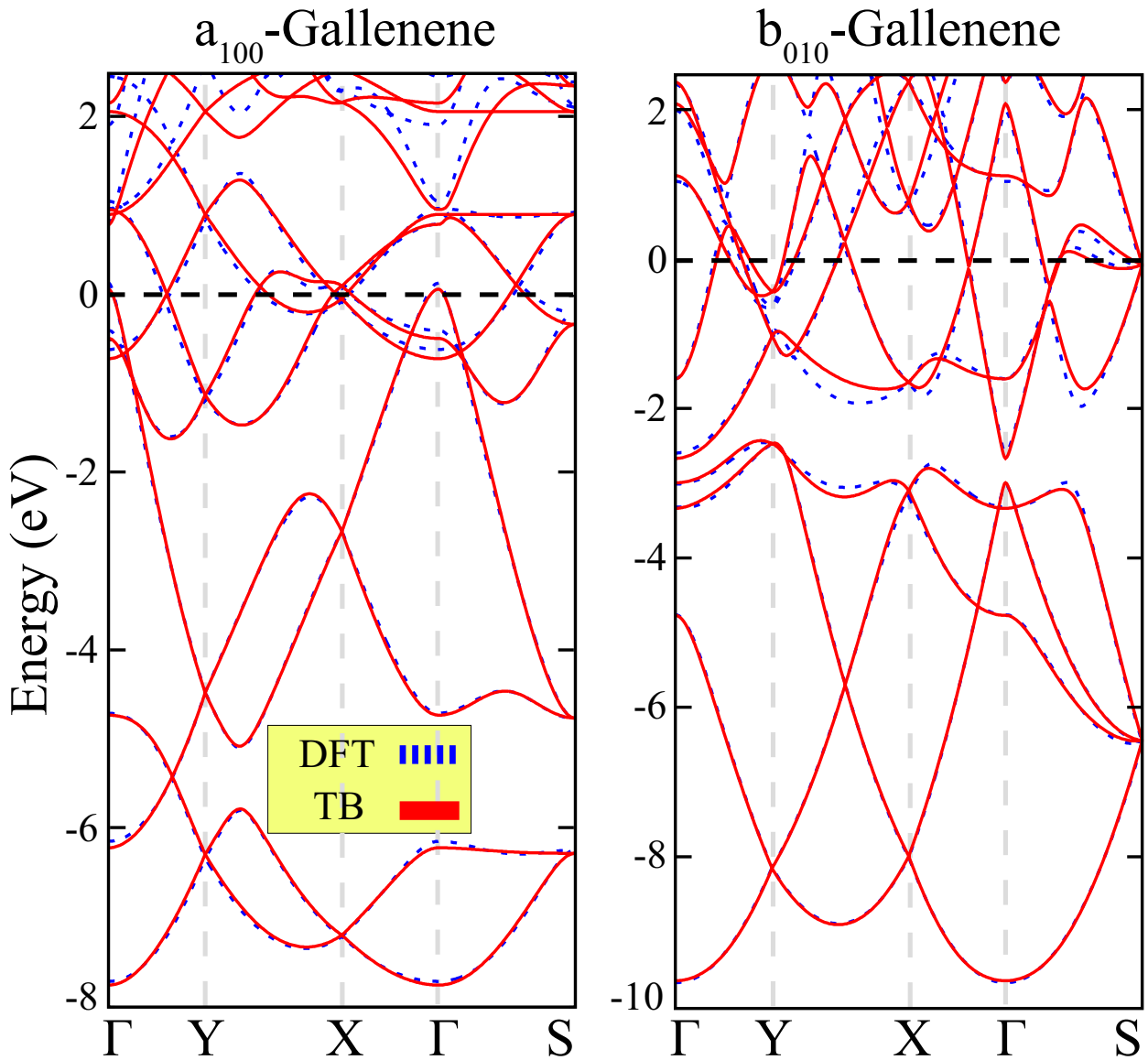


Figure 6.3: The band structure of $a_{100}$-Gallenene (left side) and $b_{010}$-Gallenene (right side) calculated within DFT (dashed blue lines) and from the TB model (solid red lines).

In DFT, we have in principle an infinite number of atoms with an infinite number of orbitals to explain the electronic structure of the different crystal structures. With the linear combination of atomic orbitals (LCAO), we are able to limit the system up to a finite number of atoms and a finite number of orbitals per atom and thus, the Bloch theorem can be effectively applied through a TB model. We use these orbitals as the basis set to represent

the wave function. The Bloch function with a well-defined $\mathbf{k}$ vector can be generally expanded as linear combinations of the orbitals $\varphi$ as follows

$$\psi_k(\mathbf{r}) = \sum_{v'} \sum_{i'} c_{i'v'}(k)\phi_{v,k}(\mathbf{r} - \mathbf{r}_i) \tag{6.1}$$

in which $i$ and $v$ run over the atoms in the unit cell and the orbitals $s$, $p_x$ ,$p_y$ and $p_z$, respectively. In the case of $a_{100}$-Gallenene and $b_{010}$-Gallenene we have four orbitals per atom and so 16 orbitals per unit cell. $\phi_{v,\mathbf{k}}(\mathbf{r})$ is defined as follows

$$\phi_{v,\mathbf{k}}(\mathbf{r}) = \sum_{n\in\mathbb{Z}} \sum_{m\in\mathbb{Z}} e^{i\mathbf{k}.\mathbf{R}_{n,m}} \varphi_v(\mathbf{r} - \mathbf{R}_{n,m}) \tag{6.2}$$

where $\mathbf{R}_{n,m}$ is the discrete translation vector of the unit cell at $(m,n)$. We limit the interactions up to the first nearest unit cell. We follow the SK scheme in combination with the usual Levenberg-Marquardt nonlinear fitting algorithm [86] to find the best hoppings for both Hamiltonian and overlap matrices.

For both structures, we have a basis of four Ga atoms and we assume a basis of four orbitals ($s$, $p_x$, $p_y$ and $p_z$) per atom, which generates a band structure with 8 valence and 8 conduction bands. So, we have in total 16 bands and we focus on the first 11 bands in the case of $a_{100}$-Gallenene and the first 10 bands for $b_{010}$-Gallenene. The generalized eigenvalue equation for the TB model may be written as follows [88];

$$\sum_{v'} \sum_{i'} [H_{iv,i'v'} - \epsilon_k S_{iv,i'v'}]c_{i'v'}(k) = 0, \tag{6.3}$$

in which $H$ is the mono-electronic Hamiltonian and $S$ is the overlap matrix which is dimensionless. The basis can be formed not orthonormal [89–91], but in the case of an orthogonal basis set ($b_{100}$-Gallenene) the overlap matrix is a unity matrix and can be ignored from the expression. The expectation values for the Hamiltonian and overlap matrix can be written in terms of distances in real space as follows

$$H_{iv,i'v'} = <\phi_v(r - r_i)|H|\phi_{v'}(r - r_{i'})>,$$
$$S_{iv,i'v'} = <\phi_v(r - r_i)|\phi_{v'}(r - r_{i'})> . \tag{6.4}$$

The integrals are calculated over the whole unit cell and $i$ and $v$ run over the atoms in the unit cell and the orbitals $s$, $p_x$, $p_y$ and $p_z$, respectively.

Theoretically, the inter-atomic matrix elements in Eq. (6.4) can in principle be calculated directly from the known wave functions, but alternatively we can use the fitting algorithm to find the best values for the integrals. The expectation values may be written in terms of the directional cosines ($n_i = \mathbf{r}.\mathbf{e}_i/|\mathbf{r}|$) as follows;

$$< s|H|s> = v_{ss\sigma},$$

$$< s|H|p_i> = n_i v_{sp\sigma},$$

$$< p_i|H|p_j> = (\delta_{ij} - n_i n_j)v_{pp\pi} + n_i n_j v_{pp\sigma},$$

where $\mathbf{r}$ is the vector along the bond while $i$ is $x$, $y$ and $z$. The corresponding expressions for the overlap matrix can be found by replacing $H$ by $S$ and $v$ by $s$. Note that one should consider the rule of angular quantum number ($< l|H|l'> = (-1)^{l+l'} < l'|H|l >$) to evaluate complex conjugated hopping matrix elements.

| $R$ | $V_{ss\sigma}$ | $V_{sp\sigma}$ | $V_{pp\sigma}$ | $V_{pp\pi}$ | $S_{ss\sigma}$ | $S_{sp\sigma}$ | $S_{pp\sigma}$ | $S_{pp\pi}$ |
|---|---|---|---|---|---|---|---|---|
| $R_1$ | -1.304 | -1.605 | 2.313 | -0.579 | 0 | 0 | 0 | 0 |
| $R_2$ | 0.016 | 0.034 | 0.227 | -0.058 | 0 | 0 | 0 | 0 |

| $R$ | $V_{ss\sigma}$ | $V_{sp\sigma}$ | $V_{pp\sigma}$ | $V_{pp\pi}$ | $S_{ss\sigma}$ | $S_{sp\sigma}$ | $S_{pp\sigma}$ | $S_{pp\pi}$ |
|---|---|---|---|---|---|---|---|---|
| $R_1$ | -1.003 | -2.167 | 1.944 | -0.662 | 0.030 | 0.205 | -0.334 | 0.270 |
| $R_2$ | -0.147 | -0.113 | 0.608 | -0.030 | 0.027 | 0.015 | -0.071 | 0.055 |
| $R_3$ | -1.176 | -2.353 | 1.300 | -0.795 | 0.017 | 0.141 | -0.367 | 0.082 |
| $R_4$ | 0.303 | -0.146 | 0.636 | -0.063 | -0.034 | -0.003 | -0.035 | -0.025 |

Table 6.1: The Slater-Koster parameters for $a_{100}$-Gallenene (top) and $b_{010}$-Gallenene (bottom). The $V$ parameters are in $eV$, and the $S$ parameters are dimensionless.

| | $a_{100}$-Gallenene | | | | $b_{010}$-Gallenene | | | |
|---|---|---|---|---|---|---|---|---|
| | $s$ | $p_x$ | $p_y$ | $p_z$ | $s$ | $p_x$ | $p_y$ | $p_z$ |
| **Ga** | -3.934 | 2.969 | 2.992 | 1.377 | -4.378 | -0.099 | 0.601 | 0.682 |

Table 6.2: The on-site energies for $a_{100}$-Gallenene and $b_{010}$-Gallenene in units of $eV$.

To calculate the TB Hamiltonian by using the eight Slater-Koster integrals, one needs to know the inter-atomic distances. In Fig. 6.1 the distance between

two Ga atoms is shown by $R_i$ where $i$ refers to different types of bonds. After optimizing the atomic positions we find the distances $R_1 = 2.655$Å, $R_2 = 2.656$Å, $R_3 = 4.572$Å and $R_4 = 4.654$Å for $a_{100}$-Gallenene and $R_1 = 2.732$Å, $R_2 = 4.744$Å, $R_3 = 2.876$Å and $R_4 = 4.649$Å for $b_{010}$-Gallenene.

The complicated electronic dispersion bands and the compact structure of $b_{010}$-Gallenene exhibit a $sp^3$ hybridization. By making a comparison between atomic packing factor (APF) [218] of $a_{100}$-Gallenene and $b_{010}$-Gallenene one can find $APF_{b_{010}} = 1.71APF_{a_{100}}$, which is the reason why we choose a non-orthogonal basis set for the structure of $b_{010}$-Gallenene. For both structures we have found the Slater-Koster integrals of Ga-Ga bonds up to the second nearest neighbors which result in a satisfactory fitting of the band structure (see Fig. 6.3). In Table 6.1, we list the Slater-Koster parameters of both systems in terms of bond length and bond type as obtained by fitting the DFT energy bands shown in Fig. 6.3. The on-site parameters of Ga atoms are presented in Table 6.2. The TB model for $b_{010}$-Gallenene can be also defined orthogonally but with taking more neighbors into acount. To explain the system orthogonally we should add the hopping between the orbitals of Ga atoms with the distance $R_5$ and $R_6$ (see Fig. 6.1). The SK parameters and onsites of the orthogonal TB model of $b_{010}$-Gallenene are presented in Tables 6.3 and 6.4.

| $R$ | $V_{ss\sigma}$ | $V_{sp\sigma}$ | $V_{pp\sigma}$ | $V_{pp\pi}$ |
|---|---|---|---|---|
| $R_1$ | -0.612 | -1.855 | 0.966 | -0.634 |
| $R_2$ | -0.176 | 0.042 | -0.163 | 0.126 |
| $R_3$ | -0.771 | -1.433 | 1.148 | -0.831 |
| $R_4$ | 0.013 | 0.073 | -0.431 | 0.126 |
| $R_5$ | -0.025 | 0.098 | -0.100 | 0.108 |
| $R_6$ | -0.249 | -0.175 | 0.156 | 0.019 |

Table 6.3: Orthogonal Slater-Koster parameters for $b_{010}$-Gallenene in $eV$.

The bandstructure of orthogonal TB model of $b_{010}$-Gallenene is presented in Fig. 6.4. It can be seen that taking more neighbors into account is equivalent to a define non-orthogonal basis set for orbitals that both cases can result in more real interactions between Ga atoms.

Using the Slater-Koster parameters one can calculate the coupling ma-
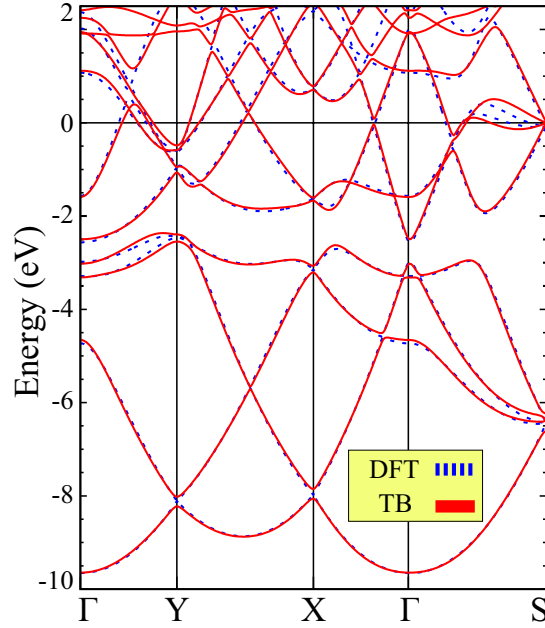
Figure 6.4: The electronic-band structure of $b_{010}$-Gallenene using orthogonal SK parameters.

| | $a_{100}$-Gallenene | | | |
|---|---|---|---|---|
| | $s$ | $p_x$ | $p_y$ | $p_z$ |
| **Ga** | -3.188 | 1.052 | 1.907 | 1.393 |

Table 6.4: The on-site energies orthogonal TB model of $b_{010}$-Gallenene in units of $eV$.

trices between different unit cells in terms of hoppings between different orbitals.

## 6.4   Transmission and Density of states

Electronic transport is one of the most interesting properties of 2d materials. The method used in this study is based on the Green's function approach in the tight-binding approximation calculated in aforementioned sections. For a 2D system, transmission and density of states (DOS) have been calculated in $x$ and $y$ directions. Green's function method is a powerful method to study the electronic properties in which the most important property of physical observables in transport, such as electrical current, is the transmission. The tight-binding description of transmission through a junction has been inter-

esting for scientists to observe how much an electron wave packet would transmit in a specific energy. One needs the hamiltonian of the system which is expressed in the tight-binding approximation. The routine method based upon a formulation for the conductance in terms of Green's functions $G$ is the well known Fisher-Lee linear-response [219] for the conductance of a finite lattice embedded between the leads. We represent the result of $a_{100}$-Gallenene and $b_{010}$-Gallenene for $x$ and $y$ directions separately. At this point it is necessary to discuss that, for a ribbon which is studied in the current work, the transmission $T(\epsilon)$ can be calculated as follows

$$T(\epsilon) = Re(Tr(\Sigma_l.G.\Sigma_r.G^\dagger)) \qquad (6.5)$$

To truly have complete information about a solid, we should know all possible states. The number of states as a function of energy that are available to be occupied is important for calculations of the effects based on the band theory like transition probability [220], conductivity calculation and computing scattering rates [221, 222]. The Green's function of the hamiltonian of the system is a key concept with important links to the concept of density of state as follows

$$DOS(\epsilon) = \frac{-1}{\pi} Im(Tr(G)) \qquad (6.6)$$

Using the SK parameters mentioned in Sec. 6.3 one can calculate the TB Hamiltonian. Note that the Hamiltonian matrix for a ribbon can be generated from the blocks of a 2D Hamiltonian matrix. Fig 6.5 shows the band structure of the ribbon of the structures in $x$ and $y$ directions. $a_{100}$-Gallenene in both $x$ and $y$ directions show metal bihavior while $b_{010}$-Gallenene ribbons are semiconductor.

Using Eq. 6.5 and Eq. 6.6 we calculated the transmission and density of states of the corresponding ribbons. Fig. 6.6 indicates the transmission of the ribbons of $a_{100}$-Gallenene and $b_{010}$-Gallenene in $x$ and $y$ directions. $b_{010}$-Gallenene in $x$ direction shows an interesting linear transmission related to the conduction band in Fig. 6.5 (c) near the Fermi level. The zero transmission comes from the $0.35(eV)$ band gap in its band-structure. As shown in Fig. 6.5
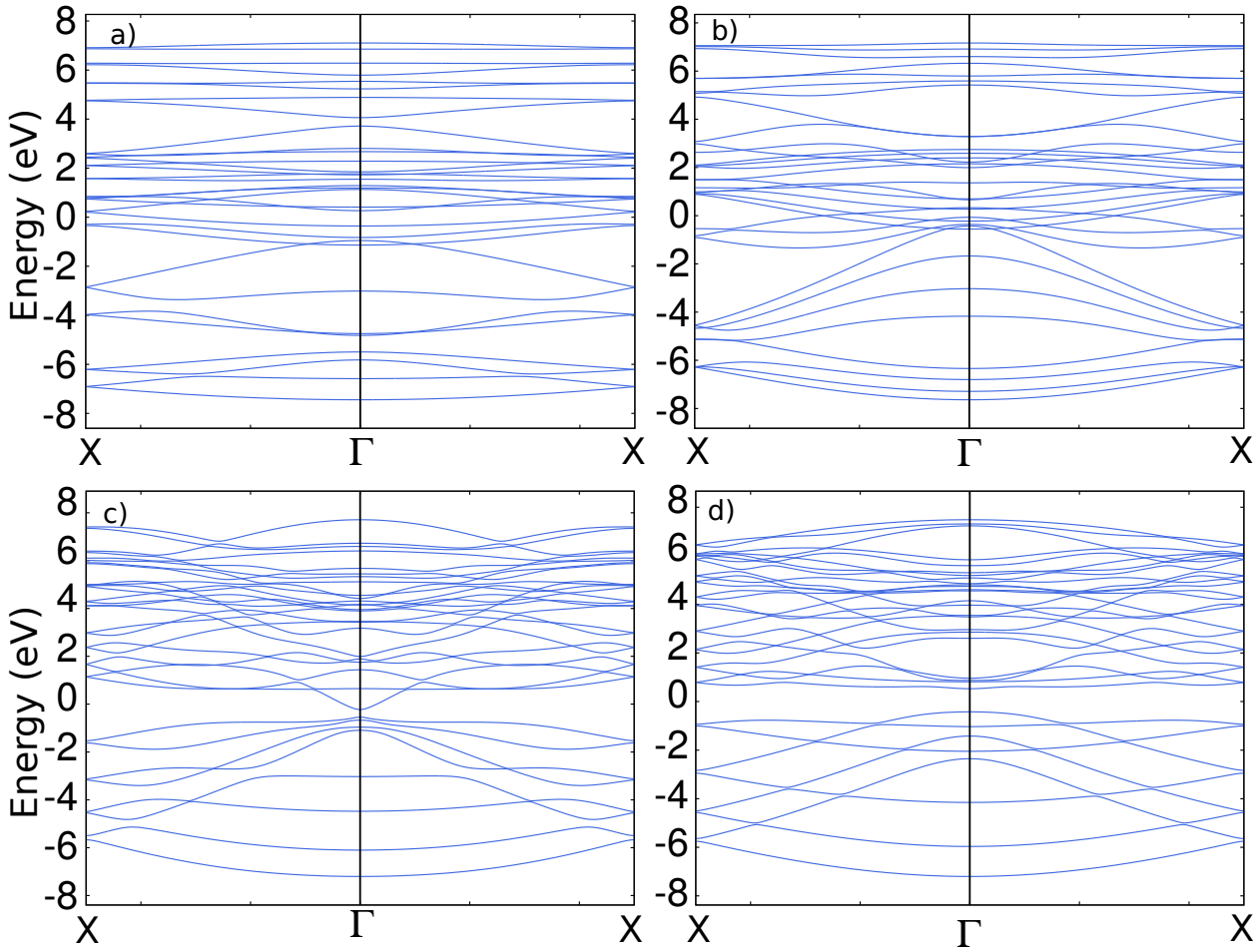
Figure 6.5: The electronic-band structure of the ribbons of $a_{100}$-Gallenene in $x$ (a) and $y$ (b) directions and $b_{010}$-Gallenene in $x$ (c) and $y$ (d) directions.

(d) $b_{010}$-Gallenene in $y$ direction has a $0.97(eV)$ band gap which is three times of its ribbon in $x$ direction.

Also the density of states for the ribbons are presented in Fig. 6.7. $a_{100}$-Gallenene in $x$ direction shows a linear density of states near the Fermi level which is an evidence to have a Dirac point in Fermi level. As shown in Fig. 6.5 (a) the $x$ direction ribbon of $a_{100}$-Gallenene has a Dirac point around $X$ point in reciprocal lattice. The gaps for the ribbons $b_{010}$-Gallenene in $x$ and $y$ directions are in agreement with the band-structures shown in Figs. 6.5 (c) and (d). It should be noted that the linear transmission related to the ribbon $b_{010}$-Gallenene in $x$ direction shows a constant density of state in Fig. 6.7 (c) near the Fermi level.
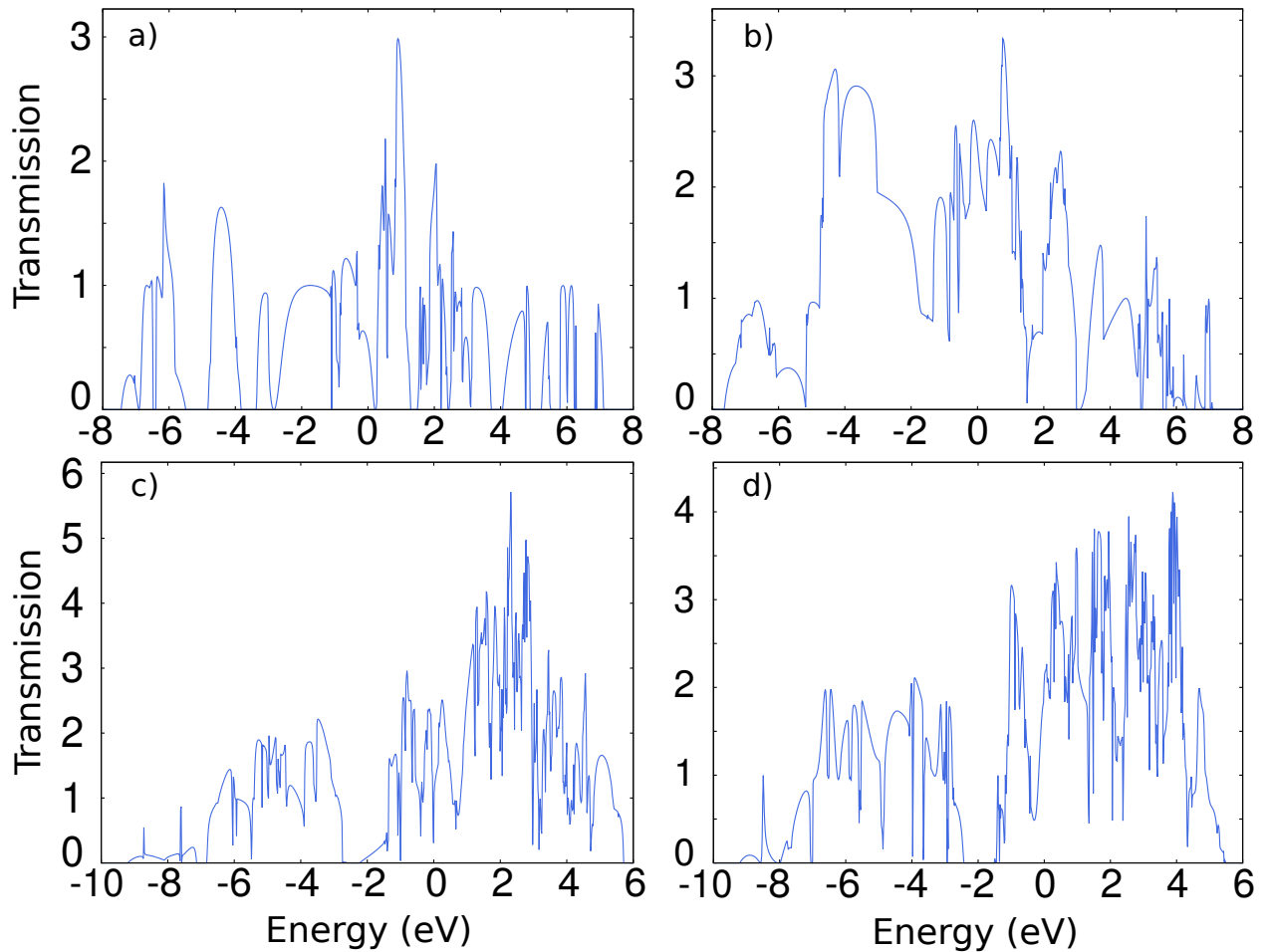
Figure 6.6: Transmission of the ribbons of $a_{100}$-Gallenene in $x$ (a) and $y$ (b) directions and $b_{010}$-Gallenene in $x$ (c) and $y$ (d) directions.

## 6.5 Data Availability

The supporting information and several examples are available at *tight-binding.com*. The examples and the supporting codes in additional programming languages, i.e. Matlab, Mathematica, Python, C, C++ and Fortran are also accessible through Code Generator tools in TBStudio.
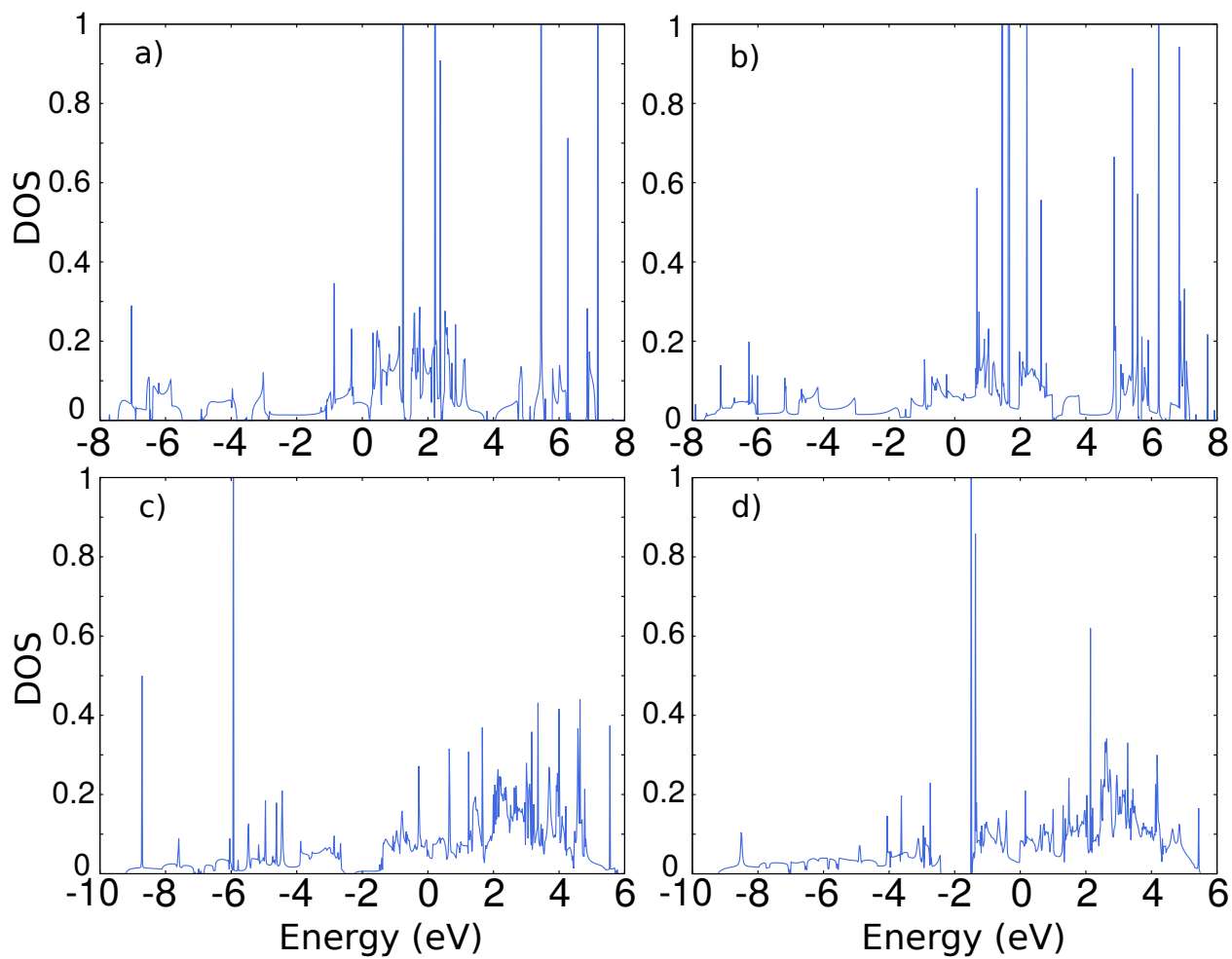
Figure 6.7: Density of states for the ribbons of $a_{100}$-Gallenene in $x$ (a) and $y$ (b) directions and $b_{010}$-Gallenene in $x$ (c) and $y$ (d) directions.

# MACHINE LEARNING APPROACH

I n the last three decades, machine learning has become more and more important for different processes. The role of artificial intelligence (AI) and machine learning is steadily increasing and is expected to further increase in the near future. Traditionally, people use machine learning for feature selection which can be performed independently with learning of classifier parameters [223]. Identification, classification, clustering or interpreting massive datasets are only some examples which show the power of AI and the ability of machines to learn.

Depending on the purpose of use, machine learning is a tool which can be used based on a wide range of theories [224], but generally machine learning has two types of generating outputs: a) identifying group membership which predicts the class of objects that may correspond to some range of values. In other words we are not searching for an exact value and b) estimating a response which predicts a value from a continuous set.

Machine learning algorithms have been used for a number of purposes in condensed matter physics [225–227]. For example, there are a number of reports on prediction and analyzing the band gap of materials [228, 229]. Several novel approaches have been presented as a correction to energy bands based on density functional theory (DFT) [230, 231]. Also some efforts have been made using machine learning together with neural networks to identify phase transitions [232].

Occasionally, a set of sequential training examples can help us to predict a new state much faster and more precisely. Such a learning technique is called supervised learning [233, 234]. Supervised learner is a model including a learning approach which maps a set of inputs to a set of outputs based on a sequential input-output pair trainings. Sequential supervised learning infers new information from the training data consisting of a set of labeled training examples which can be used for mapping new unseen instances.

Here, we show how one can use a supervised learning model to calculate the band structure of a material. Linear combination of atomic orbitals (LCAO) [235] is a good candidate to setup our approach because this method is powerful, fast and easy to establish. The most important justification to setup LCAO is that the combination of this method with Green's function theory can be also used for non-periodic systems. Besides, in the case of systems with a huge number of atoms there are a variety of cost and time efficiency motivations which can lead one to use the LCAO method.

This paper is organized as follows. Sec. 7.1 describes the physical background behind this paper. Sec. 7.2 explains our neural network in details and in Sec. 7.3 we show how to use and train it. As an example, we construct a tight-binding (TB) model for the BiTeCl structure using the neural network in Sec. 7.4.

## 7.1 Physical support

The system can be described by a set of non-interacting single-particles using the LCAO technique. Slater and Koster (SK) have shown [35] that it is possible to reproduce first-principles data using SK integrals. The SK integrals for Hamiltonian and overlap matrix elements can be expressed as follows

$$
\begin{aligned}
h_{ll'}^{mm'}(\vec{r}) &= \left\langle \varphi_l^m(\vec{x}+\vec{r})|H(\vec{x}+\vec{r})|\varphi_{l'}^{m'}(\vec{x})\right\rangle, \\
s_{ll'}^{mm'}(\vec{r}) &= \left\langle \varphi_l^m(\vec{x}+\vec{r})|\varphi_{l'}^{m'}(\vec{x})\right\rangle,
\end{aligned}
\tag{7.1}
$$

in which $\varphi_l^m$ is the real spherical harmonic which can be explained in terms of complex spherical harmonic $Y_l^m$. The bond between two atoms is defined by

the vector $\vec{r}$. The SK scheme has been successfully applied to construct tight-binding Hamiltonian of different systems [236, 237]. The integrals (7.1) will be taken over the whole 3D space. Respectively, $h_{ll'}^{mm'}(\vec{r})$ and $s_{ll'}^{mm'}(\vec{r})$ stand for the Hamiltonian and overlap matrix elements defined between two orbitals related to two different atoms as a function of $\vec{r}$. So we need to design a neural network which works with the distance between two atoms as input. We need to find a good set of parameters to explain the physics of the system. We claim here that a neuron with an exponential activation function describes orbital interactions very well and a single layer neural network made of these neurons can describe the TB model of a structure. The input of ANN $s$ shows the strain factor which is directly connected to the separation between two typical atoms. Using the input parameter one can control the size of unit-cell from one step ($a(s_i)$) to the next step ($a(s_{i+1})$). The free parameters $w_i$ and $b_i$ are weights and bias values of the neural network.

## 7.2 Artificial neural network

Inspired by the structure of the brain, it is possible to design artificial neural networks (ANN) which are able to learn from a specific training for a specific purpose. Generally, ANNs include some artificial neurons with a bias value and some links between the neurons with a weight. Weights and biases are the learnable parameters of the designed model. The aim of our paper is different from learning a concept or comparison-based learning. According to the fact that the electronic energy dispersion is closely related to the coefficients of the periodic potential, we need an associated learning algorithm which analyze data used for regression.

One can use DFT results to train the ANN and find a set of weights and bias values in order to compute outputs which match the desired outputs for a collection of labeled training data items. We found that we can make simple training examples using strain as a label. In other word we train the ANN using different structures which are the strained version of the original or target structure. The strain factor is defined by $s_i = a_i'/a_i$ where $a$ and $a'$ are, respectively, the optimized lattice parameters and that of training

example in $i^{th}$ direction. $s_i$ can be chosen from one to infinity. The strain can be uniform or non-uniform in each direction. Besides, we need a supervised learning algorithm to generalize from the training data to unseen situations in a reasonable way. During the training it can be seen that the atoms are gathered from infinity and form the original structure. It should be noted that infinity refers to a strain factor in which the atoms have the smallest overlap but not that small that it will result in flat bands. When the atoms are far from each other the bands are orthogonal and the SK parameters can be found easily resulting in reliable weights and biases. That is why we should train the ANN from infinity to one.

The behavior of SK parameters as a function of strain factor are non-linear. A single layer multi-output neural network technique was used to describe a TB model. Fig. 7.1 shows schematically the ANN which can learn from different structures generated by different strain values. The input of the ANN is the strain factor $s_i$ labeled by training step $i$ and the distance between atoms will be controlled by the strain factor. The presented ANN have $m$ outputs for a structure including $m$ different bond types and ($y_j$) is the norm ($R_n$) of the n-vector SK parameters of the $j^{th}$ defined TB bond type. For instance, we need only one output for a carbon-carbon bond in first nearest neighbor TB model of graphene.

The presented ANN is based on a collection of connected nodes with its bias $b_i$. Each connection, like the synapses in a biological brain, transmit a signal from one artificial neuron to other nodes depending on its weight $w_i$ and its activation function. Branches indicate one bond in the structure including its SK parameters that can be the input of the Hamiltonian or the input of the overlap matrix. Once a set of good weights and bias values have been found, the resulting ANN model can make predictions on any new strained structure or the optimized structure obtained from experimental or first-principles approaches.
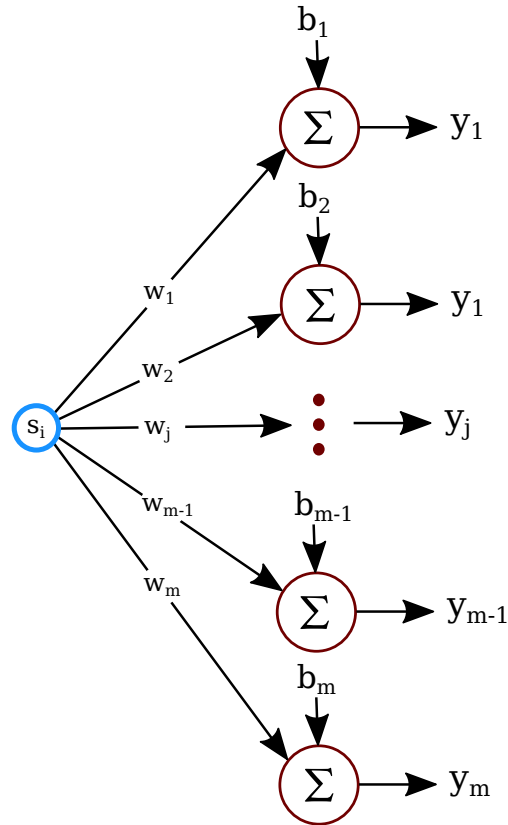
Figure 7.1: Architecture of the proposed neural network. The links with zero weight between the layers are not shown. $s_i$ and $y_j$ are input and outputs of the network, respectively.

## 7.3 Training ANN and Genetic Algorithm to Overcome Local Minima

In setting up a supervised learning we need a set of labeled training examples as $(s_1, \epsilon^1_{nk\sigma}), \ldots, (s_N, \epsilon^N_{nk\sigma})$ in which $\epsilon_{nk\sigma}$ is the energy of $n^{th}$ band and $k^{th}$ wave vector with spin $\sigma$. Respectively, $s$ and $N$ are the factor of strain and the number of training examples.

As mentioned the input of the ANN is the factor of strain which changes the distance between the atoms and as a result there is no need to care about the optimization of the example structures during the training. In each training step the weights and the bias variables would be changed.

For the case of pure mathematical problems the initial weights and bias values of a typical neural network may be initialized as random numbers to break the symmetry of the problem, but when we encounter a non-physical

a)



b)



c)
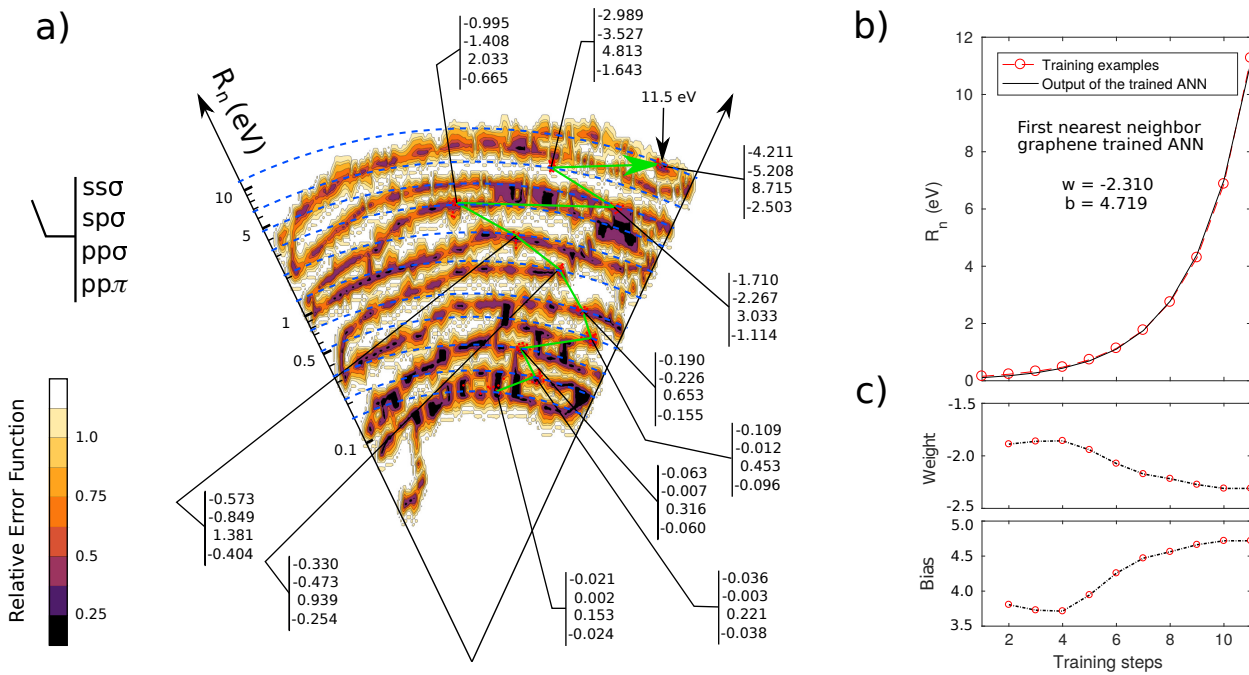
Figure 7.2: a) Local minimums for graphene with different strain factors. Green path shows the machine learning path. $R_n$ is the radius of an n-dimensional sphere in energy space in unit of eV. The best fitting of the TB model for an optimized graphene is located on the surface of a 4D sphere with 11.5 eV energy. b) The radius of the 4-vector SK parameters of graphene first nearest bond in different training steps and the output of the trained ANN. c) The convergence of the weight and bias of the neuron corresponding to the graphene C-C bond during the training procedure.

result, it is better to initialize them from the physics of the problem. The weights and bias values was initialized to zero using the fact that the overlap between two atoms which are far from each other is negligible.

After initialization the ANN, one should calculate the TB model bands using the outputs of the ANN using the SK table. In Appendix C, one can find how to calculate SK parameters for any orbital. In this step, the difference between predicted energies and actual ones will be measured through the usual mean square loss function. The loss function gives us the square deviation, in each $n$ and $k$, which is a function of the internal parameters of the ANN.

During the training, the ANN should be modified by backward propagation of errors via an optimization algorithm. We work with the usual back-propagation methods to generate new weights and bias values and consequently, we are limited to generate training examples using only uni-

form strain. Using the Levenberg-Marquardt optimization algorithm [86] we generate modified SK parameters as follows

$$\vec{v}_{s+1} = \vec{v}_s - (\mathbf{J}_s^T.\mathbf{J}_s + \mu\mathbf{I})^{-1}\mathbf{J}_s\vec{r}(\vec{v}_s), \tag{7.2}$$

where $\vec{r}$ is the residuals vector which is referred to deviation from the reference data and $\vec{v}$ is a vector including those onsite energies, Hamiltonian and overlap SK parameters are not set to be constant by the user.

In machine learning there is always the possibility of converging to a local minimum. The lack of training examples can be the cause of the appearance of local minima and one should prepare enough examples to avoid such a problem. Note that a local minimum in band structure fitting happens when a band made of a typical orbital calculated by the TB model is mistakenly converged to another orbital. It means one should be aware of the contribution of different orbitals in forming the band structure.

This problem can also be seen as a misshapen orbital in non-orthogonal basis functions [89]. For instance, during regression, the shape of an orbital may be reshaped to generate a band formed by the mixing of two orbitals. In such cases, despite the fact that we could find a set of orbitals that regenerate the energies, the model can not explain the quiddity of the solid and may result in wrong physical behaviors.

Our supervised learning algorithm allows the user to change the optimizing performance via the validation-testing process. During the training, one can adjust the parameters of regression and determine the trust region. Because, in dissimilar training examples, the quality of regression and the number of bands to fit may be different. Also the validation-testing process allows the user to change the number of nearest neighbors and to switch between the orthogonal and non-orthogonal basis functions.

The complexity of an optimization problem depends on the number of independent variables. For instance, an orthogonal ($S = 1$) TB model for graphene including $s$ and $p$ orbitals has four unknown SK integrals. To train the corresponding ANN, we change the strain factor from $s = 3.0$ to $s = 1.0$. We found that the local minimums are located near the surface of an $n$-dimensional sphere in the parameter space that $n$ is the number of

SK integrals for a typical bond. Fig. 7.2 (a) represents the local minimums during the search for a good TB model for graphene in which we mapped the error function to a 2D figure. Each point in Fig. 7.2 corresponds a 4-vector SK parameters. It is practically impossible to find adequate SK parameters using random numbers in such a large parameter space, because there are too many local minimum points. For a structure including more atoms and orbitals, the problem is clearly very difficult, as the number of local minimums may be exponential in the number of independent variables which corresponds to the number of defined TB bonds. With that in mind, we need a local minimum escaping technique. The aforementioned information lead us using Genetic algorithm (GA), in each step of the ANN training algorithm. GA is effective when very little is known about the search space. GA repeatedly modifies a population of individual solutions that in each step, individuals at random is selected from the current population to be parents and uses them to produce the children for the next generation. Basically, solutions of a problem are evolved over the generations, and the solutions are allowed to compete, crossover and mutate.

Mutation is an important operation in GA that helps to maintain the genetic diversity of the population in order to achieve a good solution to an optimization problem. Normally, people generate solutions randomly to form initial population, but we propose the machine learning approach to find the values of independent variables near the best fit. So the solution will be located in a good $n$-dimensional sphere in unit of (eV). With this we prevent seeking an n-vector SK parameters in vain and searching blindly in the dark. This kind of directed mutation introduces new points in the population guided by the information acquired from the previous machine learning steps. The green path in fig. 7.2 shows the location of the suggested SK parameters by machine learning approach in the surface of different ($n$)-dimensional spheres for different strain factors. The value of $pp\pi = -2.503\,eV$, at the end of the green path, is the famous $p_z$ carbon-carbon hopping of graphene in its first nearest neighbor TB model.

In the case of finding a TB model we need to predict the next steps from some training steps. Mathematically, it means we need to extrapolate the

next steps using the training steps which are done before. Fig. 7.2 (b) shows the output of a trained ANN for graphene TB model using the last results of $w$ and $b$. The evolution of $w$ and $b$ values are presented in Fig. 7.2 (c) which shows that, during the training procedure, the weight and bias values improve. After training the values are converged to $w = -2.310$ and $b = 4.719$. Note, the final TB model can be practically predicted after $8^{th}$ training step. The whole story can be explained by the fact that it is impossible to find the SK parameters directly for the optimized structure only using a randomly chosen SK parameters and searching blindly without having any information about the order of their energies, specially for a TB model including large number independent fitting parameters. In next section, we show the results of machine learning for an example of 55 unknown parameters for a non-orthogonal TB model of BiTeCl including SOC.

## 7.4 Application to find TB model for BiTeCl

We illustrate how the ANN works by applying it to on example. We show how one can find the TB model for BiTeCl structure. Regardless the importance of this material because of its topological behavior, BiTeCl has a complex structure made of three different atoms including more than thirty valence bands which makes it very difficult to find a reliable TB model by using the usual fitting methods. We pick this example to illustrate how powerful is our method.

The properties of topological insulators has been of interest and important for application and the lack of a TB model for BiTeCl motivated us to study this example. Promising applications of topological insulators range from spin transistors in quantum based computers and spintronic devices to optoelectronic and magnetoelectronic devices [238, 239] and quantum spin Hall effect and quantum anomalous Hall effect in such materials show the importance of the role of spin-orbit coupling in their properties [240, 241].

From first-principles calculations using the OpenMX package [37] we obtain the band structures of BiTeCl. Numerical integrations in the Brillouin zone were evaluated with the Monkhorst-Pack mesh ($15 \times 15 \times 1$). We applied
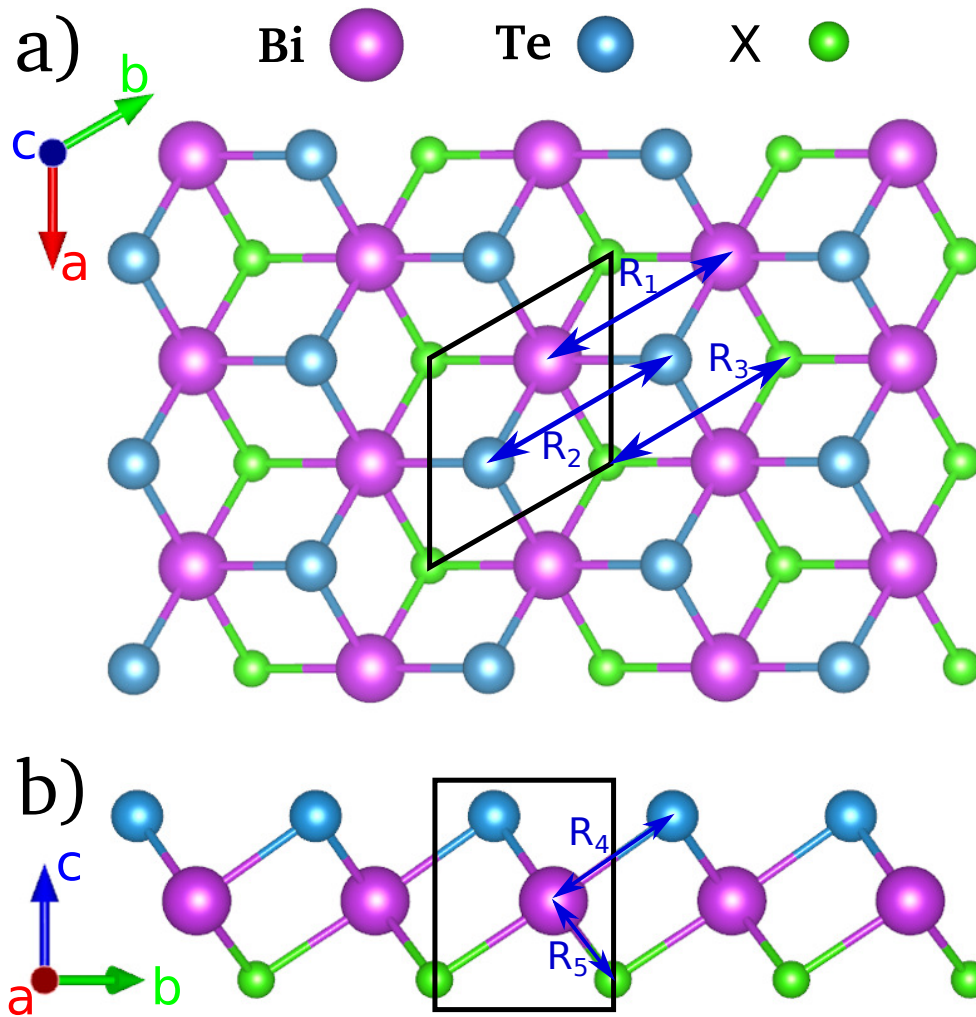
Figure 7.3: a) Top and b) side view of the structure of BiTeCl. The black box indicates the unit cell. **a**, **b** and **c** are lattice vectors and $\mathbf{R}_i$ show the nearest neighbor atoms which are used in constructing the TB model.

the generalized gradient approximation for the exchange-correlation energy, using PBE functional [93, 94] with a cutoff energy of 400 eV for the plane-wave basis. Fig. 7.3 represents the optimized structure of BiTeCl. The nearest neighbor atoms which should be included in the TB model are shown by the vectors $\mathbf{R}_i$ and the black box is the unit cell.

Let's return to the algorithm by taking the strain factor as $s_x = s_y = s_z = 2.0$ and the weights and bias values are zero. This is the beginning point to train the ANN. One can construct the TB model using the outputs of the ANN and find a new set of SK parameters, repeatedly, by changing the strain factor step by step to $s_x = s_y = s_z = 1.0$. To generate training examples, we decrease the values of $s_i$ to 1.0 to gather the atoms in all directions. In each step we
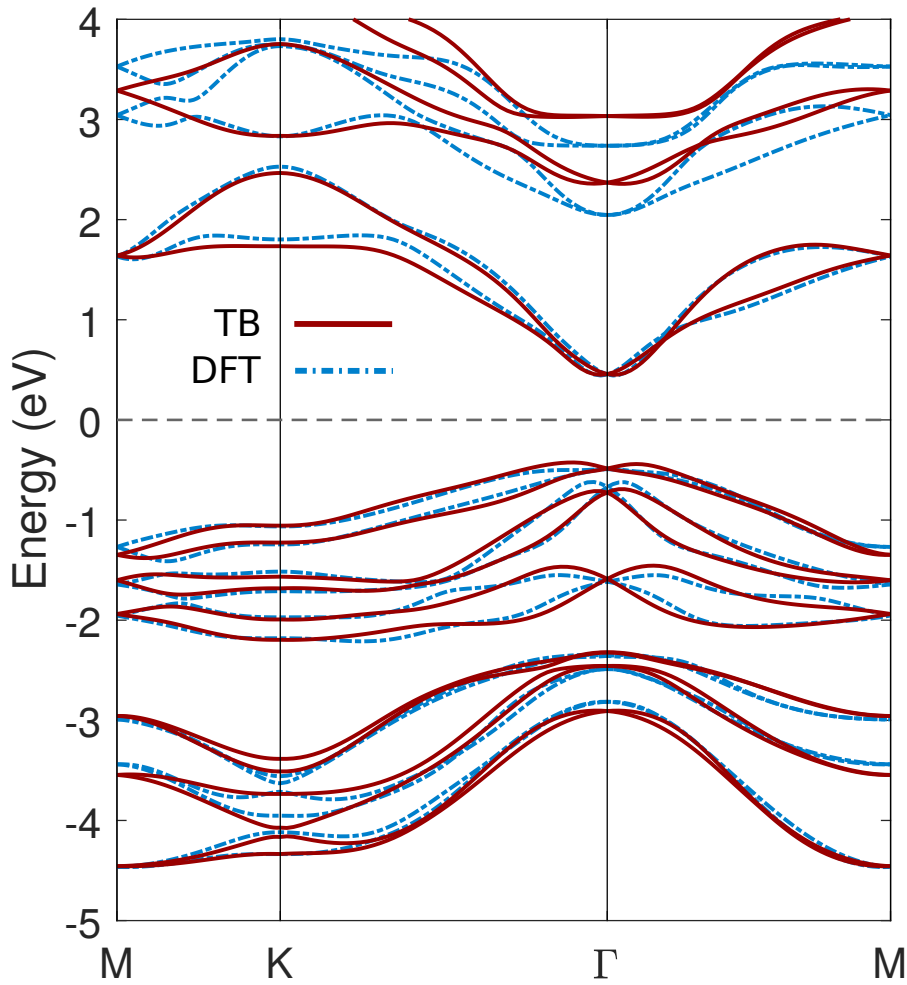
Figure 7.4: The band structures calculated by the TB model for BiTeCl structure using the SK parameters presented in Tables 7.1 and 7.2 which are compared with the DFT results.

compress the three honeycomb lattices made of $Bi$, $Te$ and $Cl$ atoms and let the atoms to be close enough to see each others.

In this work we found also overlap matrix $S$ for BiTeCl. The band structure of the TB models for BiTeCl is shown in Fig. 7.4 using the final SK parameters, on-site energies and spin-orbit coupling for different atoms from Tables 7.1 and 7.2. Very good agreement with the DFT results is obtained. In Appendix C the TB Hamiltonian and overlap matrix of BiTeCl structure are presented explicitly including the hopping between all $s$ and $p$ orbitals.

Table 7.1: The SK parameters for BiTeCl in $eV$.

| Bond type | $\mathbf{R}$ | SK integrals | | | | Overlap integrals | | | |
|---|---|---|---|---|---|---|---|---|---|
| | | $ss\sigma$ | $sp\sigma$ | $pp\sigma$ | $pp\pi$ | $ss\sigma$ | $sp\sigma$ | $pp\sigma$ | $pp\pi$ |
| Bi-Bi | $\mathbf{R}_1$ | -1.867 | -0.076 | 0.484 | 0.037 | 0.144 | -0.022 | -0.056 | 0.005 |
| Te-Te | $\mathbf{R}_2$ | -1.038 | -0.639 | 0.431 | 0.031 | 0.074 | 0.060 | -0.029 | 0.007 |
| Cl-Cl | $\mathbf{R}_3$ | 0.086 | 0.005 | -0.111 | -0.186 | -0.008 | -0.010 | 0.064 | 0.070 |
| Bi-Te | $\mathbf{R}_4$ | -1.917 | 0.992 | 1.867 | -0.679 | 0.141 | -0.030 | -0.246 | -0.027 |
| Bi-Cl | $\mathbf{R}_4$ | 4.744 | -0.655 | -2.100 | 0.116 | -0.327 | 0.117 | 0.213 | -0.060 |

Table 7.2: The onsite energies and spin-orbit coupling for BiTeCl in $eV$.

| Atom | $s$ | $p_x$ | $p_y$ | $p_z$ | $\alpha_{so}^p$ |
|---|---|---|---|---|---|
| **Bi** | -11.130 | -0.994 | -1.138 | -0.243 | -1.348 |
| **Te** | -11.121 | -2.052 | -2.244 | -1.964 | -0.634 |
| **Cl** | -14.207 | -1.375 | -1.488 | -1.840 | 0.005 |

# 7.5   Training Example

The contribution of the orbitals and atoms in different bands helps one to construct the TB model in a reasonable way. Fig. 7.5 shows nine bands near the Fermi level for BiTeCl without SOC in $s_x = s_y = s_z = 1.6$. The nine bands are made of the orbitals $p_x$, $p_y$ and $p_z$. Note that when the atoms are far from each other the orbitals have an atomic-like shape and consequently the orbitals are distinguishable in the band structure.  One can constuct the TB model as a function of SK integrals. Thease integrals can be generated using our proposed ANN. The output of the ANN in the main paper is an array $(y_1, y_2, ..., y_5)$ which are related to Bi-Bi, Te-Te, Cl-Cl, Bi-Te and Bi-Cl bond types. If the exact coefficients ($w_1, ..., w_5$ and $b_1, ..., w_5$) for the TB ANN (which includes 5 neurons) are known one can find hopping for a pair of atoms with the distance $r$. So the aim is finding $w_1$, $w_2$ and etc. coefficients. Training a neural network refers to finding weights and bias values. Normally, neural networks are capable of discovering latent structures within unstructured data and there are a lot of ways to find the unknown coefficients that are a kind of regression. The goal in using an ANN is to arrive at the point of least error as fast as possible. A labeled dataset can help our training process since we have a regularity trend which is supported by the physics behind the orbitals. A supervised learning, which means some examples that are
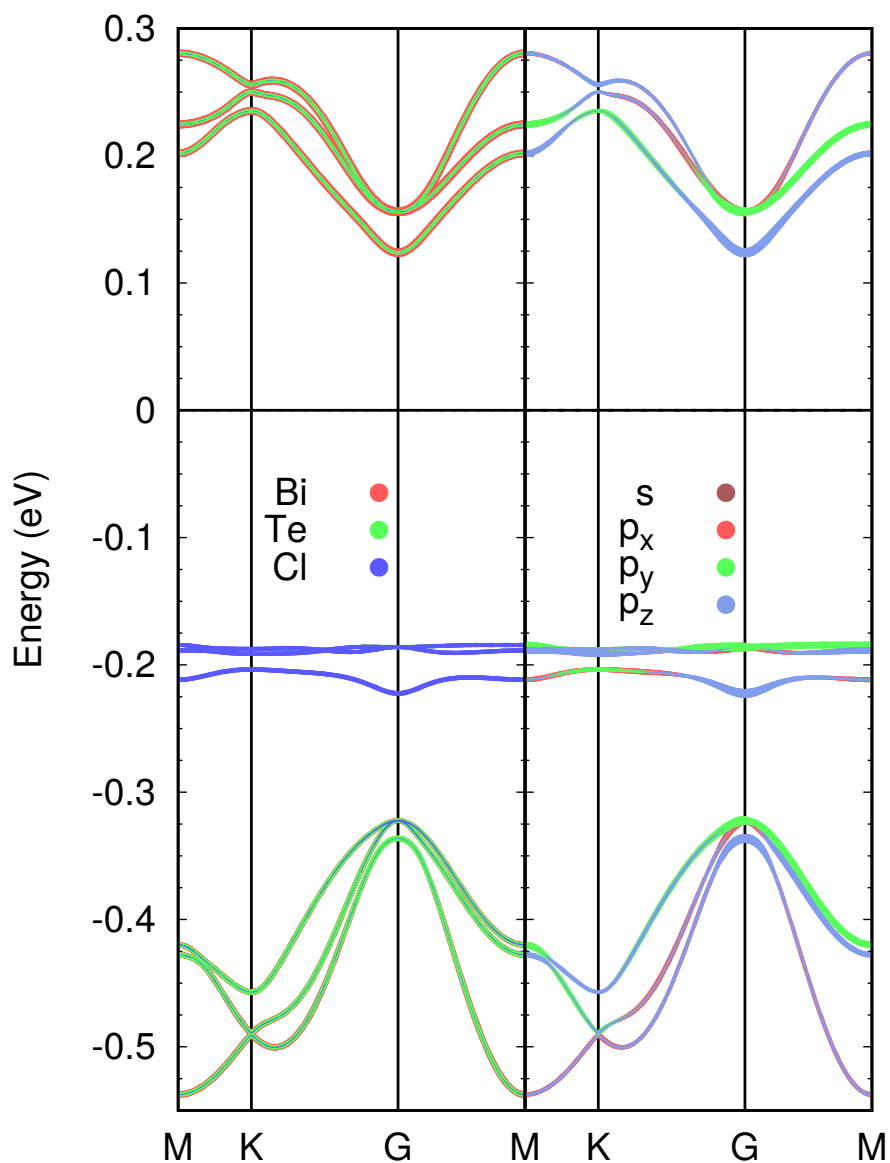
Figure 7.5: The bandstructure of BiTeCl without SOC showing the contribution of Bi, Te and Cl atoms by the different colors.

labeled, can be chosen to be fast and accurate enough. The training examples are tagged by the strain which in the case of BiTeCl we start from s=1.6 to s=1 and fit the band structure of training examples. Fig. 7.6 shows some steps of the training proccess. One can see how the TB band structure varies to the target DFT band stucture.
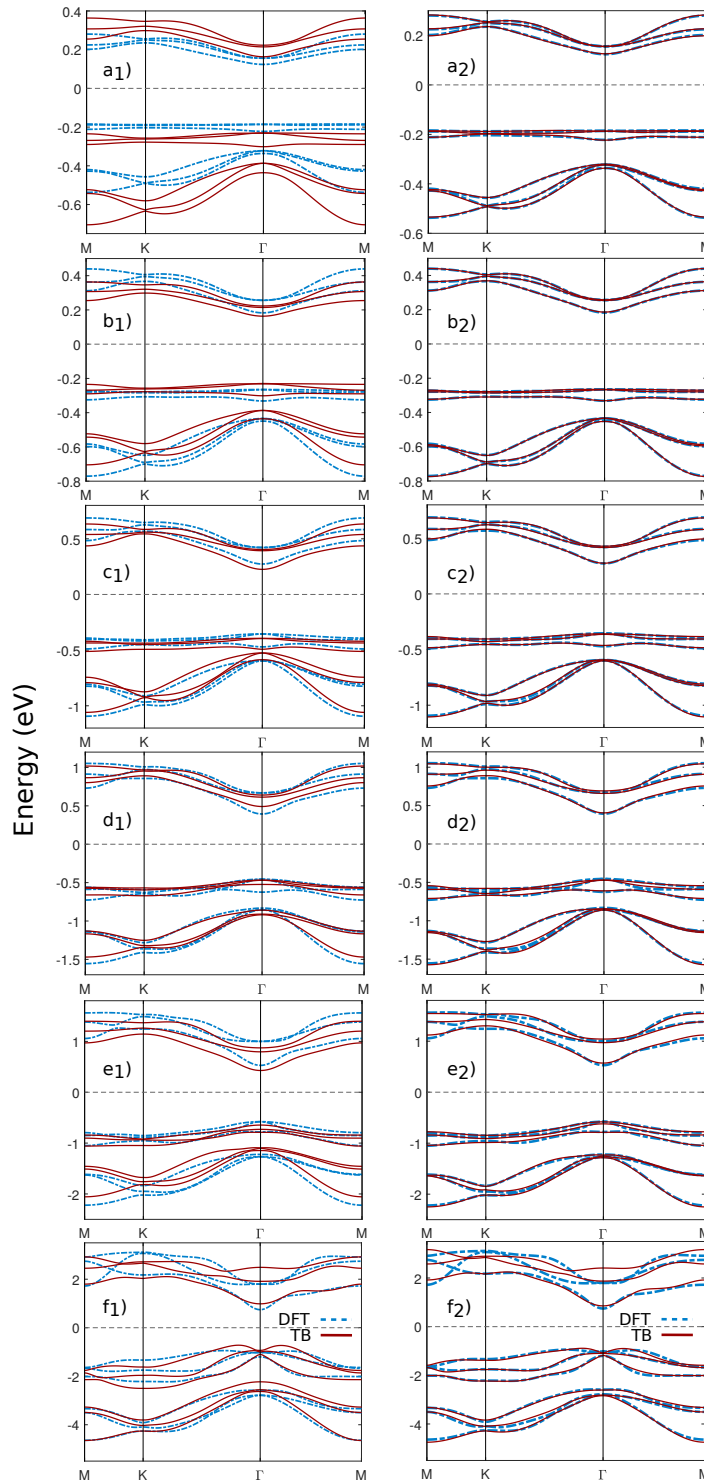
Figure 7.6: The evolution of the band structure of TB model during some training steps of the ANN for BiTeCl without SOC. $b_1$, $c_1$, $d_1$, $e_1$ and $f_1$ show the results based on guesstimate from previous steps $a_2$, $b_2$, $c_2$, $d_2$ and $e_2$, respectively. $f_2$ shows the target band structure at the optimized structure of BiTeCl.

# 7.6 Explicit Form for the Tight-binding Hamiltonian of BiTeCl

To calculate the Hamiltonian in terms of atomic orbitals we expand the Bloch functions as linear combinations of the orbitals $\varphi$ as follows

$$\psi_k(\mathbf{r}) = \sum_{v'} \sum_{i'} c_{i'v'}(k)\phi_{v,k}(\mathbf{r} - \mathbf{r}_i) \tag{7.3}$$

with

$$\phi_{v,\mathbf{k}}(\mathbf{r}) = \sum_{n\in\mathbb{Z}} \sum_{m\in\mathbb{Z}} e^{i\mathbf{k}.\mathbf{R}_{n,m}} \varphi_v(\mathbf{r} - \mathbf{R}_{n,m}) \tag{7.4}$$

in which $\mathbf{R}_{n,m}$ is the discrete translation vector of the unit cell at $(m,n)$ of the Bravais lattice. In principle, $m$ and $n$ run over an infinite array of discrete points, in this work the TB model includes only the first nearest unit cell. Table 7.3 represents the 2D lattice vectors of the BiTeCl structure. The atoms of the unit cell can be identified by their indexes as presented in Table 7.4.

| Vector | x | y | z |
|:---:|:---:|:---:|:---:|
| **a** | 2.147 | 3.729 | 0 |
| **b** | 2.147 | -3.729 | 0 |

Table 7.3: The lattice vectors for BiTeCl structure in units of Å.

| Index | Atom | x | y | z |
|:---:|:---:|:---:|:---:|:---:|
| 1 | Bi | 2.147 | -1.243 | 1.643 |
| 2 | Te | 2.147 | 1.243 | 3.408 |
| 3 | Cl | 0 | 0 | 0 |

Table 7.4: The indices and positions of the atoms in units of Å applied for constructing the TB model in this work.

The mono-electronic Hamiltonian $\mathbf{H}$ and overlap matrix $\mathbf{S}$ may be rewritten as

$$\mathbf{H} = \sum_{n=-1}^{1} \sum_{m=-1}^{1} \mathbf{h}_{n,m} e^{i\mathbf{k}.\mathbf{R}_{m,n}},$$

$$\mathbf{S} = \sum_{n=-1}^{1} \sum_{m=-1}^{1} \mathbf{s}_{n,m} e^{i\mathbf{k}.\mathbf{R}_{m,n}}, \qquad (7.5)$$

where $\mathbf{R}_{m,n}$ is the translation vector of the unit cell $(m,n)$. Since $\mathbf{H}$ is Hermitian therefore

$$\mathbf{h}_{-1,0} = \mathbf{h}_{1,0}^{\dagger}, \mathbf{h}_{0,-1} = \mathbf{h}_{0,1}^{\dagger},$$

$$\mathbf{h}_{-1,-1} = \mathbf{h}_{1,1}^{\dagger}, \mathbf{h}_{-1,1} = \mathbf{h}_{1,-1}^{\dagger}. \qquad (7.6)$$

And the same equations are valid for $\mathbf{s}$. Hence, we have 10 independent matrices. We only need to determine $\mathbf{h}$ and $\mathbf{s}$ for the cells at $(0,0)$, $(1,0)$, $(0,1)$, $(1,1)$ and $(-1,1)$. Note that the matrices $\mathbf{h}_{-1,1}$ and $\mathbf{h}_{1,-1}$ are zero for hexagonal BiTeCl structure. Since the number of atoms in the unit cell is three and each atom has four orbitals the Hamiltonian matrix is of size $12 \times 12$. Taking SOC into accounts leads us to the total Hamiltonian of BiTeCl as follows

$$\mathbf{H}_{Total} = \mathbf{H} \times I_{2\times 2} + \mathbf{H}^{SOC}. \qquad (7.7)$$

One needs to calculate the second term using the SOC parameters presented in the main paper. We use the SK coefficients presented in the paper and calculate $\mathbf{H}$ and $\mathbf{S}$ and extract the matrices $\mathbf{h}_{0,0}$, $\mathbf{h}_{0,1}$, $\mathbf{h}_{1,0}$, $\mathbf{h}_{1,1}$, $\mathbf{s}_{0,0}$, $\mathbf{s}_{0,1}$, $\mathbf{s}_{1,0}$ and $\mathbf{s}_{1,1}$ for BiTeCl as following (respectively, $\mathbf{h}_{0,0}$, $\mathbf{h}_{0,1}$, $\mathbf{h}_{1,0}$, $\mathbf{h}_{1,1}$, $\mathbf{s}_{0,0}$, $\mathbf{s}_{0,1}$, $\mathbf{s}_{1,0}$ and $\mathbf{s}_{1,1}$)

| | $s$ | $p_y$ | $p_z$ | $p_x$ | $s$ | $p_y$ | $p_z$ | $p_x$ | $s$ | $p_y$ | $p_z$ | $p_x$ | |
|---|---|---|---|---|---|---|---|---|---|---|---|---|---|
| | −11.130 | 0 | 0 | 0 | −1.917 | 0.809 | 0.575 | 0 | 4.744 | −0.274 | 0.362 | 0.473 | $s$ |
| | 0 | −1.138 | 0 | 0 | −0.809 | 1.014 | 1.202 | 0 | 0.274 | −0.271 | 0.511 | 0.668 | $p_y$ |
| | 0 | 0 | −0.243 | 0 | −0.575 | 1.202 | 0.174 | 0 | −0.362 | 0.511 | −0.559 | −0.883 | $p_z$ |
| | 0 | 0 | 0 | −0.994 | 0 | 0 | 0 | −0.679 | −0.473 | 0.668 | −0.883 | −1.037 | $p_x$ |
| | −1.917 | −0.809 | −0.575 | 0 | −11.121 | 0 | 0 | 0 | 0 | 0 | 0 | 0 | $s$ |
| | 0.809 | 1.014 | 1.202 | 0 | 0 | −2.244 | 0 | 0 | 0 | 0 | 0 | 0 | $p_y$ |
| | 0.575 | 1.202 | 0.174 | 0 | 0 | 0 | −1.964 | 0 | 0 | 0 | 0 | 0 | $p_z$ |
| | 0 | 0 | 0 | −0.679 | 0 | 0 | 0 | −2.052 | 0 | 0 | 0 | 0 | $p_x$ |
| | 4.744 | 0.274 | −0.362 | −0.473 | 0 | 0 | 0 | 0 | −14.207 | 0 | 0 | 0 | $s$ |
| | −0.274 | −0.271 | 0.511 | 0.668 | 0 | 0 | 0 | 0 | 0 | −1.488 | 0 | 0 | $p_y$ |
| | 0.362 | 0.511 | −0.559 | −0.883 | 0 | 0 | 0 | 0 | 0 | 0 | −1.840 | 0 | $p_z$ |
| | 0.473 | 0.668 | −0.883 | −1.037 | 0 | 0 | 0 | 0 | 0 | 0 | 0 | −1.375 | $p_x$ |

| | $s$ | $p_y$ | $p_z$ | $p_x$ | $s$ | $p_y$ | $p_z$ | $p_x$ | $s$ | $p_y$ | $p_z$ | $p_x$ | |
|---|---|---|---|---|---|---|---|---|---|---|---|---|---|
| | −1.867 | 0.066 | 0 | −0.038 | −1.917 | −0.405 | 0.575 | 0.700 | 4.744 | 0.547 | 0.361 | 0 | $s$ |
| | −0.066 | 0.373 | 0 | −0.194 | 0.405 | −0.255 | −0.603 | −0.733 | −0.547 | −1.426 | −1.019 | 0 | $p_y$ |
| | 0 | 0 | 0.037 | 0 | −0.575 | −0.603 | 0.177 | 1.041 | −0.361 | −1.019 | −0.557 | 0 | $p_z$ |
| | 0.038 | −0.194 | 0 | 0.148 | −0.700 | −0.733 | 1.041 | 0.587 | 0 | 0 | 0 | 0.116 | $p_x$ |
| | 0 | 0 | 0 | 0 | −1.038 | 0.554 | 0 | −0.319 | 0 | 0 | 0 | 0 | $s$ |
| | 0 | 0 | 0 | 0 | −0.554 | 0.331 | 0 | −0.173 | 0 | 0 | 0 | 0 | $p_y$ |
| | 0 | 0 | 0 | 0 | 0 | 0 | 0.031 | 0 | 0 | 0 | 0 | 0 | $p_z$ |
| | 0 | 0 | 0 | 0 | 0.319 | −0.173 | 0 | 0.131 | 0 | 0 | 0 | 0 | $p_x$ |
| | 0 | 0 | 0 | 0 | 0 | 0 | 0 | 0 | 0.086 | −0.004 | 0 | 0.002 | $s$ |
| | 0 | 0 | 0 | 0 | 0 | 0 | 0 | 0 | 0.004 | −0.129 | 0 | −0.032 | $p_y$ |
| | 0 | 0 | 0 | 0 | 0 | 0 | 0 | 0 | 0 | 0 | −0.186 | 0 | $p_z$ |
| | 0 | 0 | 0 | 0 | 0 | 0 | 0 | 0 | −0.002 | −0.032 | 0 | −0.167 | $p_x$ |

| | s | $p_y$ | $p_z$ | $p_x$ | s | $p_y$ | $p_z$ | $p_x$ | s | $p_y$ | $p_z$ | $p_x$ | |
|---|---|---|---|---|---|---|---|---|---|---|---|---|---|
| | −1.867 | −0.066 | 0 | −0.038 | 0 | 0 | 0 | 0 | 0 | 0 | 0 | 0 | s |
| | 0.066 | 0.373 | 0 | 0.194 | 0 | 0 | 0 | 0 | 0 | 0 | 0 | 0 | $p_y$ |
| | 0 | 0 | 0.037 | 0 | 0 | 0 | 0 | 0 | 0 | 0 | 0 | 0 | $p_z$ |
| | 0.038 | 0.194 | 0 | 0.148 | 0 | 0 | 0 | 0 | 0 | 0 | 0 | 0 | $p_x$ |
| | −1.917 | 0.405 | −0.575 | 0.700 | −1.038 | −0.554 | 0 | −0.319 | 0 | 0 | 0 | 0 | s |
| | −0.405 | −0.255 | −0.603 | 0.733 | 0.554 | 0.331 | 0 | 0.173 | 0 | 0 | 0 | 0 | $p_y$ |
| | 0.575 | −0.603 | 0.177 | −1.041 | 0 | 0 | 0.031 | 0 | 0 | 0 | 0 | 0 | $p_z$ |
| | −0.700 | 0.733 | −1.041 | 0.587 | 0.319 | 0.173 | 0 | 0.131 | 0 | 0 | 0 | 0 | $p_x$ |
| | 0 | 0 | 0 | 0 | 0 | 0 | 0 | 0 | 0.086 | 0.004 | 0 | 0.002 | s |
| | 0 | 0 | 0 | 0 | 0 | 0 | 0 | 0 | −0.004 | −0.129 | 0 | 0.032 | $p_y$ |
| | 0 | 0 | 0 | 0 | 0 | 0 | 0 | 0 | 0 | 0 | −0.186 | 0 | $p_z$ |
| | 0 | 0 | 0 | 0 | 0 | 0 | 0 | 0 | −0.002 | 0.032 | 0 | −0.167 | $p_x$ |

| | s | $p_y$ | $p_z$ | $p_x$ | s | $p_y$ | $p_z$ | $p_x$ | s | $p_y$ | $p_z$ | $p_x$ | |
|---|---|---|---|---|---|---|---|---|---|---|---|---|---|
| | −1.867 | 0 | 0 | −0.076 | 0 | 0 | 0 | 0 | 4.744 | −0.274 | 0.362 | −0.473 | s |
| | 0 | 0.037 | 0 | 0 | 0 | 0 | 0 | 0 | 0.274 | −0.271 | 0.511 | −0.668 | $p_y$ |
| | 0 | 0 | 0.037 | 0 | 0 | 0 | 0 | 0 | −0.362 | 0.511 | −0.559 | 0.883 | $p_z$ |
| | 0.076 | 0 | 0 | 0.484 | 0 | 0 | 0 | 0 | 0.473 | −0.668 | 0.883 | −1.037 | $p_x$ |
| | 0 | 0 | 0 | 0 | −1.038 | 0 | 0 | −0.639 | 0 | 0 | 0 | 0 | s |
| | 0 | 0 | 0 | 0 | 0 | 0.031 | 0 | 0 | 0 | 0 | 0 | 0 | $p_y$ |
| | 0 | 0 | 0 | 0 | 0 | 0 | 0.031 | 0 | 0 | 0 | 0 | 0 | $p_z$ |
| | 0 | 0 | 0 | 0 | 0.639 | 0 | 0 | 0.431 | 0 | 0 | 0 | 0 | $p_x$ |
| | 0 | 0 | 0 | 0 | 0 | 0 | 0 | 0 | 0.086 | 0 | 0 | 0.005 | s |
| | 0 | 0 | 0 | 0 | 0 | 0 | 0 | 0 | 0 | −0.186 | 0 | 0 | $p_y$ |
| | 0 | 0 | 0 | 0 | 0 | 0 | 0 | 0 | 0 | 0 | −0.186 | 0 | $p_z$ |
| | 0 | 0 | 0 | 0 | 0 | 0 | 0 | 0 | −0.005 | 0 | 0 | −0.111 | $p_x$ |

| $s$ | $p_y$ | $p_z$ | $p_x$ | $s$ | $p_y$ | $p_z$ | $p_x$ | $s$ | $p_y$ | $p_z$ | $p_x$ | |
|---|---|---|---|---|---|---|---|---|---|---|---|---|
| 1 | 0 | 0 | 0 | 0.141 | −0.025 | −0.018 | 0 | −0.327 | 0.049 | −0.065 | −0.085 | $s$ |
| 0 | 1 | 0 | 0 | 0.025 | −0.173 | −0.103 | 0 | −0.049 | −0.012 | −0.063 | −0.082 | $p_y$ |
| 0 | 0 | 1 | 0 | 0.018 | −0.103 | −0.101 | 0 | 0.065 | −0.063 | 0.023 | 0.109 | $p_z$ |
| 0 | 0 | 0 | 1 | 0 | 0 | 0 | −0.027 | 0.085 | −0.082 | 0.109 | 0.082 | $p_x$ |
| 0.141 | 0.025 | 0.018 | 0 | 1 | 0 | 0 | 0 | 0 | 0 | 0 | 0 | $s$ |
| −0.025 | −0.173 | −0.103 | 0 | 0 | 1 | 0 | 0 | 0 | 0 | 0 | 0 | $p_y$ |
| −0.018 | −0.103 | −0.101 | 0 | 0 | 0 | 1 | 0 | 0 | 0 | 0 | 0 | $p_z$ |
| 0 | 0 | 0 | −0.027 | 0 | 0 | 0 | 1 | 0 | 0 | 0 | 0 | $p_x$ |
| −0.327 | −0.049 | 0.065 | 0.085 | 0 | 0 | 0 | 0 | 1 | 0 | 0 | 0 | $s$ |
| 0.049 | −0.012 | −0.063 | −0.082 | 0 | 0 | 0 | 0 | 0 | 1 | 0 | 0 | $p_y$ |
| −0.065 | −0.063 | 0.023 | 0.109 | 0 | 0 | 0 | 0 | 0 | 0 | 1 | 0 | $p_z$ |
| −0.085 | −0.082 | 0.109 | 0.082 | 0 | 0 | 0 | 0 | 0 | 0 | 0 | 1 | $p_x$ |

| $s$ | $p_y$ | $p_z$ | $p_x$ | $s$ | $p_y$ | $p_z$ | $p_x$ | $s$ | $p_y$ | $p_z$ | $p_x$ | |
|---|---|---|---|---|---|---|---|---|---|---|---|---|
| 0.144 | 0.019 | 0 | −0.011 | 0.141 | 0.012 | −0.018 | −0.021 | −0.327 | −0.098 | −0.065 | 0 | $s$ |
| −0.019 | −0.040 | 0 | 0.026 | −0.012 | −0.064 | 0.052 | 0.063 | 0.098 | 0.130 | 0.125 | 0 | $p_y$ |
| 0 | 0 | 0.005 | 0 | 0.018 | 0.052 | −0.101 | −0.089 | 0.065 | 0.125 | 0.023 | 0 | $p_z$ |
| 0.011 | 0.026 | 0 | −0.010 | 0.021 | 0.063 | −0.089 | −0.136 | 0 | 0 | 0 | −0.060 | $p_x$ |
| 0 | 0 | 0 | 0 | 0.074 | −0.052 | 0 | 0.030 | 0 | 0 | 0 | 0 | $s$ |
| 0 | 0 | 0 | 0 | 0.052 | −0.020 | 0 | 0.016 | 0 | 0 | 0 | 0 | $p_y$ |
| 0 | 0 | 0 | 0 | 0 | 0 | 0.007 | 0 | 0 | 0 | 0 | 0 | $p_z$ |
| 0 | 0 | 0 | 0 | −0.030 | 0.016 | 0 | −0.002 | 0 | 0 | 0 | 0 | $p_x$ |
| 0 | 0 | 0 | 0 | 0 | 0 | 0 | 0 | −0.008 | 0.009 | 0 | −0.005 | $s$ |
| 0 | 0 | 0 | 0 | 0 | 0 | 0 | 0 | −0.009 | 0.066 | 0 | 0.002 | $p_y$ |
| 0 | 0 | 0 | 0 | 0 | 0 | 0 | 0 | 0 | 0 | 0.070 | 0 | $p_z$ |
| 0 | 0 | 0 | 0 | 0 | 0 | 0 | 0 | 0.005 | 0.002 | 0 | 0.069 | $p_x$ |

| | $s$ | $p_y$ | $p_z$ | $p_x$ | $s$ | $p_y$ | $p_z$ | $p_x$ | $s$ | $p_y$ | $p_z$ | $p_x$ | |
|---|---|---|---|---|---|---|---|---|---|---|---|---|---|
| | 0.144 | −0.019 | 0 | −0.011 | 0 | 0 | 0 | 0 | 0 | 0 | 0 | 0 | $s$ |
| | 0.019 | −0.040 | 0 | −0.026 | 0 | 0 | 0 | 0 | 0 | 0 | 0 | 0 | $p_y$ |
| | 0 | 0 | 0.005 | 0 | 0 | 0 | 0 | 0 | 0 | 0 | 0 | 0 | $p_z$ |
| | 0.011 | −0.026 | 0 | −0.010 | 0 | 0 | 0 | 0 | 0 | 0 | 0 | 0 | $p_x$ |
| | 0.141 | −0.012 | 0.018 | −0.021 | 0.074 | 0.052 | 0 | 0.030 | 0 | 0 | 0 | 0 | $s$ |
| | 0.012 | −0.064 | 0.052 | −0.063 | −0.052 | −0.020 | 0 | −0.016 | 0 | 0 | 0 | 0 | $p_y$ |
| | −0.018 | 0.052 | −0.101 | 0.089 | 0 | 0 | 0.007 | 0 | 0 | 0 | 0 | 0 | $p_z$ |
| | 0.021 | −0.063 | 0.089 | −0.136 | −0.030 | −0.016 | 0 | −0.002 | 0 | 0 | 0 | 0 | $p_x$ |
| | 0 | 0 | 0 | 0 | 0 | 0 | 0 | 0 | −0.008 | −0.009 | 0 | −0.005 | $s$ |
| | 0 | 0 | 0 | 0 | 0 | 0 | 0 | 0 | 0.009 | 0.066 | 0 | −0.002 | $p_y$ |
| | 0 | 0 | 0 | 0 | 0 | 0 | 0 | 0 | 0 | 0 | 0.070 | 0 | $p_z$ |
| | 0 | 0 | 0 | 0 | 0 | 0 | 0 | 0 | 0.005 | −0.002 | 0 | 0.069 | $p_x$ |

| | $s$ | $p_y$ | $p_z$ | $p_x$ | $s$ | $p_y$ | $p_z$ | $p_x$ | $s$ | $p_y$ | $p_z$ | $p_x$ | |
|---|---|---|---|---|---|---|---|---|---|---|---|---|---|
| | 0.144 | 0 | 0 | −0.022 | 0 | 0 | 0 | 0 | −0.327 | 0.049 | −0.065 | 0.085 | $s$ |
| | 0 | 0.005 | 0 | 0 | 0 | 0 | 0 | 0 | −0.049 | −0.012 | −0.063 | 0.082 | $p_y$ |
| | 0 | 0 | 0.005 | 0 | 0 | 0 | 0 | 0 | 0.065 | −0.063 | 0.023 | −0.109 | $p_z$ |
| | 0.022 | 0 | 0 | −0.056 | 0 | 0 | 0 | 0 | −0.085 | 0.082 | −0.109 | 0.082 | $p_x$ |
| | 0 | 0 | 0 | 0 | 0.074 | 0 | 0 | 0.060 | 0 | 0 | 0 | 0 | $s$ |
| | 0 | 0 | 0 | 0 | 0 | 0.007 | 0 | 0 | 0 | 0 | 0 | 0 | $p_y$ |
| | 0 | 0 | 0 | 0 | 0 | 0 | 0.007 | 0 | 0 | 0 | 0 | 0 | $p_z$ |
| | 0 | 0 | 0 | 0 | −0.060 | 0 | 0 | −0.029 | 0 | 0 | 0 | 0 | $p_x$ |
| | 0 | 0 | 0 | 0 | 0 | 0 | 0 | 0 | −0.008 | 0 | 0 | −0.010 | $s$ |
| | 0 | 0 | 0 | 0 | 0 | 0 | 0 | 0 | 0 | 0.070 | 0 | 0 | $p_y$ |
| | 0 | 0 | 0 | 0 | 0 | 0 | 0 | 0 | 0 | 0 | 0.070 | 0 | $p_z$ |
| | 0 | 0 | 0 | 0 | 0 | 0 | 0 | 0 | 0.010 | 0 | 0 | 0.064 | $p_x$ |

Note that coupling matrices $\mathbf{h}_{1,-1}$ and $\mathbf{s}_{1,-1}$ are zero for our TB model.

# SUMMARY AND OUTLOOK

Using the simplified LCAO method in combination with first-principles calculations, we construct a tight-binding (TB) model in the two-centre approximation for two-dimensional materials. The Slater and Koster (SK) approach are applied to calculate the TB Hamiltonian of these systems. We obtain expressions for the Hamiltonian and overlap matrix elements between different orbitals for the different atoms and present the SK coefficients in orthogonal and non-orthogonal basis sets. We present Tight-Binding Studio (TBStudio) software package for calculating TB Hamiltonian from a set of Bloch energy bands obtained from first principle theories such as density functional theory, Hartree-Fock calculations or Semi-empirical band structure theory. This will be helpful for scientists who are interested in studying electronic properties of structures using Green's function theory in TB approximation. TBStudio is a cross-platform application written in C++ with a graphical user interface design that is user-friendly and easy to work with. This software is powered by Linear Algebra Package C interface library for solving the eigenvalue problems and the standard high performance OpenGL graphic library for real time plotting. TBStudio and its examples together with the tutorials are available for download from *tight-binding.com*. Using this software we find TB model for borophene and hydrogenated borophene (borophane) in a non-orthogonal basis set. We also calculated the Dirac low-energy Hamiltonian of borophane which describes the physics within the anisotropic Dirac cone and

derived an analytical expression for the density of states. The full expression for the Hamiltonian and overlap matrices for borophene and borophane are given in the supplementary information. We also study Bilayer borphene. Bilayer hexagonal borphene is bound together through pillars which is a novel topological semimetal. Using density functional theory, we investigated the origin of nodal line and identified its electronic properties as a Dirac material. A TB model was constructed based on the Slater-Koster approach in order to explain the band energies. In order to describe the nodal line we presented an effective $4 \times 4$ low-energy model Hamiltonian near the $K$ point and presented an analytical equation for the nodal line as a function of azimuthal angle around the center of the nodal line. The nodal line in the spectrum is a result of two inter-penetrating Dirac cones. Due to the different trigonal warping of the two Dirac cones the nodal line is not isoenergetic with an energy dispersion.

Furthermore, a novel method is proposed to construct TB models for solids using machine learning techniques. The approach is based on the LCAO method and Slater-Koster (SK) integrals and a single layer multi-output neural network in order to obtain the optimal SK parameters. A single layer multi-output neural network model was designed to construct the TB model for solids. The input variable for the proposed Artificial Neural Networks (ANN) is the strain factor which is connected to the distance between two typical atoms and the outputs are the SK parameters. By training the ANN the weights and biases improve and the final result can predict the band structure. We constructed the ANN for BiTeCl structure and studied the values of weights and biases during the training including spin-orbit coupling which plays an important role in their electronic properties. The proposed ANN predicted successfully the band structures as shown by a comparison with DFT results.

Also we studied the double Dirac nodal line found in $Cu_2Si$ monolayer. We show that an effective four band model Hamiltonian describes the spectrum near the nodal line accurately. The Dirac nodal lines in $Cu_2Si$ form two concentric loops centered around the $\Gamma$ point and are protected by mirror reflection symmetry. Our results show that the nodal lines are created by

edge states and are very robust against perturbations and impurities. Our results establish $Cu_2Si$ as a new platform to study novel physical properties in two-dimensional Dirac materials and provide new opportunities to realize high-speed low-dissipation devices.

# SAMENVATTING

Met behulp van de vereenvoudigde LCAO-methode in combinatie met berekeningen met de eerste principes, construeren we een Tight-Binding (TB) model in de tweecenterbenadering voor tweedimensionale materialen. De Slater en Koster (SK) -benadering wordt toegepast om de TB Hamiltoniaan van deze systemen te berekenen. We verkrijgen uitdrukkingen voor de Hamiltoniaanse en overlappende matrixelementen tussen verschillende orbitalen voor de verschillende atomen en presenteren de SK-coëfficiënten in orthogonale en niet-orthogonale basissets. Een nieuw softwarepakket Tight-Binding Studio (TBStudio) werd geconstead voor het berekenen van TB Hamiltonianen uit een reeks Bloch-energiebanden die zijn verkregen op basis van eerste principe theorieën zoals dichtheidstheorie, Hartree-Fock-berekeningen of Semi-empirische bandstructuurtheorie. Dit zal nuttig zijn voor wetenschappers die geïnteresseerd zijn in het bestuderen van elektronische eigenschappen van structuren met behulp van Green se functies in een TB benadering. TBStudio is een platformoverschrijdende applicatie geschreven in C++ met een grafisch gebruikersinterfaceontwerp dat gebruiksvriendelijk en gemakkelijk is om mee te werken. Deze software wordt aangedreven door de Linear Algebra Package C-interfacebibliotheek voor het oplossen van de eigenwaardeproblemen en standaard hoogwaardige OpenGL grafische bibliotheek voor realtime plotten. TBStudio en zijn voorbeelden samen met de tutorials kunnen worden gedownload van *tight-binding.com*. Met behulp van

deze software vinden we het TB-model voor borofeen en gehydrogeneerd boro-feen (borofaan) in een niet-orthogonale basisset. We berekenden ook de Dirac lage-energie Hamiltoniaan van borofaan die de fysica binnen de anisotrope Dirac-kegel beschrijft en er werd een analytische uitdrukking afgeleid voor de dichtheid van toestanden. De volledige uitdrukking voor de Hamiltoniaanse en overlappende matrices voor borofeen en borofaan worden gegeven in de aanvullende informatie. We bestuderen ook bilaag borofeen. Bilaag zeshoekig borfeen bestaad uit een dublede laag broofeen aan elkaar gebonden door pijlers, dat een nieuw topologisch semimetaal is Met behulp van dichtheid functionaal theorie, hebben we de oorsprong van knooppunten onderzocht en de elektronische eigenschappen ervan geïdentificeerd als een Dirac-materiaal. Een TB model werd gebouwd op basis van de Slater-Koster-aanpak om de bandenergieën te verklaren. Om de knooplijn te beschrijven, presenteerden we een effectief $4 \times 4$ laag-energiemodel Hamiltonian nabij het $K$ punt en pre-senteerden we een analytische vergelijking voor de knooplijn als een functie van de azimutale hoek rond het midden van de knooplijn. De knooplijn in het spectrum is een gevolg van twee doordringende Dirac-kegels. Vanwege de verschillende trigonale kromming van de twee Dirac-kegels is de knooplijn niet iso-energetisch en besit het een energiedispersie.

Verder wordt een nieuwe methode voorgesteld om TB modellen voor vaste stoffen te construeren met behulp van machine learning-technieken. De aan-pak is gebaseerd op de LCAO-methode en Slater-Koster (SK) -integralen en een enkellagig multi-output neuraal netwerk om de optimale SK-parameters te verkrijgen. Een enkellagig multi-output neuraal netwerkmodel werd ont-worpen om het model voor vaste stoffen te construeren. De ingangsvariabele voor de voorgestelde Artificial Neural Networks (ANN) is de spanningsfactor die is verbonden met de afstand tussen twee typische atomen en de outputs zijn de SK-parameters. Door de ANN te trainen verbeteren de gewichten en het eindresultaat geeft o.a. de bandstructuur. We hebben de ANN voor BiTeCl-structuur geconstrueerd en de waarden van gewichten bestudeerd tijdens de training, inclusief spin-orbit-koppeling die een belangrijke rol speelt in hun elektronische eigenschappen. De voorgestelde ANN voorspelde met succes de bandstructuren, zoals blijkt uit een vergelijking met DFT-resultaten.

We hebben ook de dubbele Dirac knooplijn bestudeerd in $Cu_2Si$ monolaag. We laten zien dat een effectief vierbandsmodel Hamiltoniaan het spectrum nabij de knooplijn nauwkeurig beschrijft. De Dirac knooppunten in $Cu_2Si$ vormen twee concentrische lussen gecentreerd rond het $\Gamma$ punt en die worden beschermd door spiegelreflectiesymmetrie. Onze resultaten laten zien dat de knooppunten worden gecreëerd door randtoestanden en zeer robuust zijn tegen storingen en onzuiverheden. Onze resultaten voorspellen dat $Cu_2Si$ gebruikt kan worden als een nieuw platform om nieuwe fysische eigenschappen in tweedimensionale Dirac-materialen te bestuderen. Dit biedt nieuwe kansen om hoge-snelheid-apparaten te realiseren.

# APPENDIX A: ANALYTICAL EXPRESSION FOR THE GREEN'S FUNCTION FOR AN ANISOTROPIC DIRAC HAMILTONIAN

Considering the Dirac equation mentioned in section 3.2, we calculate the Green's function for a general anisotropic Dirac cone which is tilted in the x-direction. We are interested in finding an analytical expression for the Green's function which is needed to calculate the density of states. We start from the definition of the Green's function in the reciprocal representation as follows

$$G(\mathbf{k}, \varepsilon) = (\varepsilon I - H_{\mathbf{k}})^{-1}. \tag{A.1}$$

The density of states is defined as the imaginary part of the diagonal elements of the retarded Green's function, one can evaluate these components by using Eq. (**??**) and Eq. (A.1) as below

$$G_{1,1}(\mathbf{k}, \varepsilon) = G_{2,2}(\mathbf{k}, \varepsilon) = \frac{\varepsilon - k_x v_t}{(\varepsilon - k_x v_t)^2 - k_x^2 v_x^2 - k_y^2 v_y^2}. \tag{A.2}$$

It is useful to evaluate the real space Green's function $G(\mathbf{r} - \mathbf{r}', \varepsilon)$ by taking the Fourier transform. One motivation for calculating the Fourier transform of Green's function comes from the fact that we can easily derive the density of states from the imaginary part of the diagonal elements of Green's function

in real space as follows

$$DOS(\varepsilon) = \frac{-1}{\pi} Im(G_{1,1}(\mathbf{r} = \mathbf{r}', \varepsilon) + G_{2,2}(\mathbf{r} = \mathbf{r}', \varepsilon)). \tag{A.3}$$

Corresponding real space Green's function is defined by the two dimensional Fourier transformation

$$G(\mathbf{r} - \mathbf{r}', \varepsilon) = \frac{1}{\Omega} \int d\mathbf{k}^2 e^{i\mathbf{k}.(\mathbf{r}-\mathbf{r}')} G(\mathbf{k}, \varepsilon) \tag{A.4}$$

where, $\Omega$ denotes the area of the first Brillouin zone. We define $k^2 = (v_x k_x)^2 + (v_y k_y)^2$ and $v_x k_x = k \cos\varphi$ and transform cartesian to polar coordinates.

$$G_{1,1}(0, \varepsilon) = \frac{1}{\Omega} \int_0^{2\pi} d\varphi \int_0^{k_c} k\, dk \frac{\varepsilon - \frac{v_t}{v_x} k \cos\varphi}{(\varepsilon - \frac{v_t}{v_x} k \cos\varphi)^2 - k^2}. \tag{A.5}$$

Here, $k_c = \varepsilon_c/(1 - v_t/v_x)$ where $\varepsilon_c$ is the cut-off energy for evaluating the integral. After some simplifications one can derive the Green's function expression as follows

$$G_{1,1}(0, \varepsilon) = \frac{1}{\Omega}(g(\varepsilon) + g(-\varepsilon)) \tag{A.6}$$

with

$$g(\varepsilon) = \frac{i\pi v_x}{v_y \left(v_t^2 - v_x^2\right)} \left( \sqrt{-\varepsilon^2} - \sqrt{\frac{k_c^2 v_t^2}{v_x^2} - (k_c - \varepsilon)^2} + \frac{\varepsilon v_x}{\sqrt{v_t^2 - v_x^2}} \log \frac{v_x \sqrt{v_t^2 - v_x^2} \sqrt{\frac{k_c^2 v_t^2}{v_x^2} - (k_c - \varepsilon)^2} + k_c \left(v_t^2 - v_x^2\right) + \varepsilon v_x^2}{\sqrt{-\varepsilon^2} v_x \sqrt{v_t^2 - v_x^2} + \varepsilon v_x^2} \right). \tag{A.7}$$

To extract the imaginary part of the Green's function we applied the Cauchy principal value $\frac{1}{x+i\eta} = P(\frac{1}{x}) - i\pi\delta(x)$ in which $\eta$ is an infinitely small quantity. After using the property of the Dirac delta function for the integrals over $k$ and $\varphi$, the imaginary part of Eq. (A.6) becomes

$$Im(G_{1,1}(0, \varepsilon)) = \frac{-\pi^2 v_x^2}{\Omega v_y (v_x^2 - v_t^2)^{\frac{3}{2}}} |\varepsilon| \Theta(\varepsilon_c - |\varepsilon|) \tag{A.8}$$

# APPENDIX B: EXPLICIT FORM FOR THE TIGHT-BINDING HAMILTONIAN OF BOROPHENE

Starting from Eqs. (1) and (2) in the main article we are able to present explicitly both the Hamiltonian and overlap matrix. We can expand the Bloch functions as linear combinations of the orbitals $\varphi$ as follows

$$\psi_k(\mathbf{r}) = \sum_{v'} \sum_{i'} c_{i'v'}(k)\phi_{v,k}(\mathbf{r} - \mathbf{r}_i) \tag{B.1}$$

with

$$\phi_{v,\mathbf{k}}(\mathbf{r}) = \sum_{n\in\mathbb{Z}} \sum_{m\in\mathbb{Z}} e^{i\mathbf{k}.\mathbf{R}_{n,m}} \varphi_v(\mathbf{r} - \mathbf{R}_{n,m}) \tag{B.2}$$

in which $\mathbf{R}_{n,m}$ is the discrete translation vector of the unit cell at $(m,n)$ of the Bravais lattice. Although $m$ and $n$ run over an infinite array of discrete points, in this work the TB model includes only the first nearest unit cell. Fig. B.1 shows a schematic representation of the TB model $8 \times 8$ Hamiltonian. The mono-electronic Hamiltonian $H$ and the overlap matrix $S$ may be rewritten as

$$\mathbf{H} = \sum_{n=-1}^{1} \sum_{m=-1}^{1} \mathbf{h}_{n,m} e^{i(nak_x + mbk_y)} \tag{B.3}$$

and

109

Figure B.1: Schematic representation of the TB model for borophene and borophane. The white cells indicate independent unit cells.

$$\mathbf{S} = \sum_{n=-1}^{1} \sum_{m=-1}^{1} \mathbf{s}_{n,m} e^{i(nak_x + mbk_y)}. \tag{B.4}$$

Since $\mathbf{H}$ and $\mathbf{S}$ are Hermitian therefore

$$\mathbf{h}_{n,m} = \mathbf{h}_{m,n}^{\dagger},$$
$$\mathbf{s}_{n,m} = \mathbf{s}_{m,n}^{\dagger}. \tag{B.5}$$

hence, we have only five independent matrices. As shown in Fig. B.1 we must determine only the matrices $\mathbf{h}$ and $\mathbf{s}$ for the cells at $(0,0)$, $(1,0)$, $(0,1)$, $(1,1)$ and $(-1,1)$. Using the SK coefficients presented in the main paper we can calculate the Hamiltonian and the overlap matrix and extract the matrices $\mathbf{h}$ and $\mathbf{s}$. In the case of borophene the elements of the Hamiltonian can be written as follows

$$\mathbf{h}_{0,0} = \begin{pmatrix} & s & p_x & p_y & p_z & s & p_x & p_y & p_z \\ -4.949 & 0 & 0 & 0 & -2.410 & 1.624 & 2.851 & -1.713 \\ 0 & 1.601 & 0 & 0 & -1.624 & 0.030 & 1.483 & -0.891 \\ 0 & 0 & -1.298 & 0 & -2.851 & 1.483 & 1.789 & -1.565 \\ 0 & 0 & 0 & 2.998 & 1.713 & -0.891 & -1.565 & 0.126 \\ -2.410 & -1.624 & -2.851 & 1.713 & -4.949 & 0 & 0 & 0 \\ 1.624 & 0.030 & 1.483 & -0.891 & 0 & 1.601 & 0 & 0 \\ 2.851 & 1.483 & 1.789 & -1.565 & 0 & 0 & -1.298 & 0 \\ -1.713 & -0.891 & -1.565 & 0.126 & 0 & 0 & 0 & 2.997 \end{pmatrix} \begin{matrix} s \\ p_x \\ p_y \\ p_z \\ s \\ p_x \\ p_y \\ p_z \end{matrix}$$

$$\mathbf{h}_{1,0} = \begin{pmatrix} & s & p_x & p_y & p_z & s & p_x & p_y & p_z \\ -3.728 & -4.391 & 0 & 0 & -2.410 & -1.624 & 2.851 & -1.713 \\ 4.391 & 4.445 & 0 & 0 & 1.624 & 0.030 & -1.483 & 0.891 \\ 0 & 0 & -2.298 & 0 & -2.851 & -1.483 & 1.789 & -1.565 \\ 0 & 0 & 0 & -2.298 & 1.713 & 0.891 & -1.565 & 0.126 \\ 0 & 0 & 0 & 0 & -3.728 & -4.391 & 0 & 0 \\ 0 & 0 & 0 & 0 & 4.391 & 4.445 & 0 & 0 \\ 0 & 0 & 0 & 0 & 0 & 0 & -2.298 & 0 \\ 0 & 0 & 0 & 0 & 0 & 0 & 0 & -2.298 \end{pmatrix} \begin{matrix} s \\ p_x \\ p_y \\ p_z \\ s \\ p_x \\ p_y \\ p_z \end{matrix}$$

$$\mathbf{h}_{0,1} = \begin{pmatrix} & s & p_x & p_y & p_z & s & p_x & p_y & p_z \\ -0.279 & 0 & -0.825 & 0 & -2.410 & 1.624 & -2.851 & -1.713 \\ 0 & -0.543 & 0 & 0 & -1.624 & 0.030 & -1.483 & -0.891 \\ 0.825 & 0 & 1.914 & 0 & 2.851 & -1.483 & 1.789 & 1.565 \\ 0 & 0 & 0 & -0.543 & 1.713 & -0.891 & 1.565 & 0.126 \\ 0 & 0 & 0 & 0 & -0.279 & 0 & -0.825 & 0 \\ 0 & 0 & 0 & 0 & 0 & -0.543 & 0 & 0 \\ 0 & 0 & 0 & 0 & 0.825 & 0 & 1.914 & 0 \\ 0 & 0 & 0 & 0 & 0 & 0 & 0 & -0.543 \end{pmatrix} \begin{matrix} s \\ p_x \\ p_y \\ p_z \\ s \\ p_x \\ p_y \\ p_z \end{matrix}$$

$$
\mathbf{h}_{1,1} =
\begin{array}{cccccccc}
s & p_x & p_y & p_z & s & p_x & p_y & p_z \\
\end{array}
\left(
\begin{array}{cccccccc}
0 & 0 & 0 & 0 & -2.410 & -1.624 & -2.851 & -1.713 \\
0 & 0 & 0 & 0 & 1.624 & 0.030 & 1.483 & 0.891 \\
0 & 0 & 0 & 0 & 2.851 & 1.483 & 1.789 & 1.565 \\
0 & 0 & 0 & 0 & 1.713 & 0.891 & 1.565 & 0.126 \\
0 & 0 & 0 & 0 & 0 & 0 & 0 & 0 \\
0 & 0 & 0 & 0 & 0 & 0 & 0 & 0 \\
0 & 0 & 0 & 0 & 0 & 0 & 0 & 0 \\
0 & 0 & 0 & 0 & 0 & 0 & 0 & 0 \\
\end{array}
\right)
\begin{array}{c}
s \\ p_x \\ p_y \\ p_z \\ s \\ p_x \\ p_y \\ p_z
\end{array}
$$

and for the overlap matrix we have

$$
\mathbf{s}_{0,0} =
\begin{array}{cccccccc}
s & p_x & p_y & p_z & s & p_x & p_y & p_z \\
\end{array}
\left(
\begin{array}{cccccccc}
1 & 0 & 0 & 0 & 0.019 & -0.074 & -0.129 & 0.078 \\
0 & 1 & 0 & 0 & 0.074 & -0.075 & -0.067 & 0.040 \\
0 & 0 & 1 & 0 & 0.129 & -0.067 & -0.154 & 0.070 \\
0 & 0 & 0 & 1 & -0.078 & 0.040 & 0.070 & -0.079 \\
0.019 & 0.074 & 0.129 & -0.078 & 1 & 0 & 0 & 0 \\
-0.074 & -0.075 & -0.067 & 0.040 & 0 & 1 & 0 & 0 \\
-0.129 & -0.067 & -0.154 & 0.070 & 0 & 0 & 1 & 0 \\
0.078 & 0.040 & 0.070 & -0.079 & 0 & 0 & 0 & 1 \\
\end{array}
\right)
\begin{array}{c}
s \\ p_x \\ p_y \\ p_z \\ s \\ p_x \\ p_y \\ p_z
\end{array}
$$

$$
\mathbf{s}_{1,0} =
\begin{array}{cccccccc}
s & p_x & p_y & p_z & s & p_x & p_y & p_z \\
\end{array}
\left(
\begin{array}{cccccccc}
0.213 & 0.287 & 0 & 0 & 0.019 & 0.074 & -0.129 & 0.078 \\
-0.287 & -0.384 & 0 & 0 & -0.074 & -0.075 & 0.067 & -0.040 \\
0 & 0 & 0.063 & 0 & 0.129 & 0.067 & -0.154 & 0.070 \\
0 & 0 & 0 & 0.063 & -0.078 & -0.040 & 0.070 & -0.079 \\
0 & 0 & 0 & 0 & 0.213 & 0.287 & 0 & 0 \\
0 & 0 & 0 & 0 & -0.287 & -0.384 & 0 & 0 \\
0 & 0 & 0 & 0 & 0 & 0 & 0.063 & 0 \\
0 & 0 & 0 & 0 & 0 & 0 & 0 & 0.063 \\
\end{array}
\right)
\begin{array}{c}
s \\ p_x \\ p_y \\ p_z \\ s \\ p_x \\ p_y \\ p_z
\end{array}
$$

$$
\mathbf{s}_{0,1} =
\begin{array}{cccccccc}
s & p_x & p_y & p_z & s & p_x & p_y & p_z \\
\end{array}
$$

$$
\mathbf{s}_{0,1} =
\left(
\begin{array}{cccccccc}
-0.034 & 0 & -0.022 & 0 & 0.019 & -0.074 & 0.129 & 0.078 \\
0 & 0.034 & 0 & 0 & 0.074 & -0.075 & 0.067 & 0.040 \\
0.022 & 0 & 0.017 & 0 & -0.129 & 0.067 & -0.154 & -0.070 \\
0 & 0 & 0 & 0.034 & -0.078 & 0.040 & -0.070 & -0.079 \\
0 & 0 & 0 & 0 & -0.034 & 0 & -0.022 & 0 \\
0 & 0 & 0 & 0 & 0 & 0.034 & 0 & 0 \\
0 & 0 & 0 & 0 & 0.022 & 0 & 0.017 & 0 \\
0 & 0 & 0 & 0 & 0 & 0 & 0 & 0.034 \\
\end{array}
\right)
\begin{array}{c}
s \\ p_x \\ p_y \\ p_z \\ s \\ p_x \\ p_y \\ p_z
\end{array}
$$

$$
\mathbf{s}_{1,1} =
\left(
\begin{array}{cccccccc}
0 & 0 & 0 & 0 & 0.019 & 0.074 & 0.129 & 0.078 \\
0 & 0 & 0 & 0 & -0.074 & -0.075 & -0.067 & -0.040 \\
0 & 0 & 0 & 0 & -0.129 & -0.067 & -0.154 & -0.070 \\
0 & 0 & 0 & 0 & -0.078 & -0.040 & -0.070 & -0.079 \\
0 & 0 & 0 & 0 & 0 & 0 & 0 & 0 \\
0 & 0 & 0 & 0 & 0 & 0 & 0 & 0 \\
0 & 0 & 0 & 0 & 0 & 0 & 0 & 0 \\
0 & 0 & 0 & 0 & 0 & 0 & 0 & 0 \\
\end{array}
\right)
\begin{array}{c}
s \\ p_x \\ p_y \\ p_z \\ s \\ p_x \\ p_y \\ p_z
\end{array}
$$

Note that we construct the TB model up to the third nearest neighbor sites and so there is no interaction between cells $(0,0)$ and $(-1,1)$, so $\mathbf{h}_{-1,1} = \mathbf{s}_{-1,1} = \mathbf{0}$. Other elements of the coupling matrices can be found by the relation mentioned in Eq. (B.5).

## B.1 Explicit form for the tight-binding Hamiltonian of borophane

In the case of borophane we should add two $s$ atomic orbitals for the hydrogens as follows

$$
\psi_{\mathbf{k}}(\mathbf{r}) = \sum_{v'} \sum_{i'} c_{i'v'}(\mathbf{k}) \phi_{v',\mathbf{k}}(\mathbf{r} - \mathbf{r}_i)
$$
$$
+ c_{H_1,s}(\mathbf{k}) \phi_{s,\mathbf{k}}(\mathbf{r} - \mathbf{r}_{H_1})
$$
$$
+ c_{H_2,s}(\mathbf{k}) \phi_{s,\mathbf{k}}(\mathbf{r} - \mathbf{r}_{H_2}) \tag{B.6}
$$

in which $H_1$ and $H_2$ indicate the index of hydrogen atoms in the unit cell. So, Eqs. (B.3) and (B.4) would not be changed and only the size of the Hamiltonian and overlap matrix is changed to $10 \times 10$. The elements of the Hamiltonian can be written as follows

$\mathbf{h}_{0,0} =$

|  | $s$ | $p_x$ | $p_y$ | $p_z$ | $s$ | $p_x$ | $p_y$ | $p_z$ | $s_H$ | $s_H$ |  |
|---|---|---|---|---|---|---|---|---|---|---|---|
|  | −3.131 | 0. | 0. | 0. | −2.822 | −1.527 | −2.228 | 1.275 | 4.523 | 0. | $s$ |
|  | 0. | 3.861 | 0. | 0. | 1.527 | 0.102 | 1.130 | −0.647 | 0. | 0. | $p_x$ |
|  | 0. | 0. | 0.103 | 0. | 2.228 | 1.130 | 0.976 | −0.943 | 0. | 0. | $p_y$ |
|  | 0. | 0. | 0. | −1.015 | −1.275 | −0.647 | −0.943 | −0.132 | −3.941 | 0. | $p_z$ |
|  | −2.822 | 1.527 | 2.228 | −1.275 | −3.131 | 0. | 0. | 0. | 0. | 4.523 | $s$ |
|  | −1.527 | 0.102 | 1.130 | −0.647 | 0. | 3.861 | 0. | 0. | 0. | 0. | $p_x$ |
|  | −2.228 | 1.130 | 0.976 | −0.943 | 0. | 0. | 0.103 | 0. | 0. | 0. | $p_y$ |
|  | 1.275 | −0.647 | −0.943 | −0.132 | 0. | 0. | 0. | −1.015 | 0. | 3.941 | $p_z$ |
|  | 4.523 | 0. | 0. | −3.941 | 0. | 0. | 0. | 0. | 7.575 | 0. | $s_H$ |
|  | 0. | 0. | 0. | 0. | 4.523 | 0. | 0. | 3.941 | 0. | 7.575 | $s_H$ |

$\mathbf{h}_{1,0} =$

|  | $s$ | $p_x$ | $p_y$ | $p_z$ | $s$ | $p_x$ | $p_y$ | $p_z$ | $s_H$ | $s_H$ |  |
|---|---|---|---|---|---|---|---|---|---|---|---|
|  | −0.742 | 1.710 | 0. | 0. | −2.822 | 1.527 | −2.228 | 1.275 | 0. | 0. | $s$ |
|  | −1.709 | 2.076 | 0. | 0. | −1.527 | 0.102 | −1.130 | 0.647 | 0. | 0. | $p_x$ |
|  | 0. | 0. | −1.381 | 0. | 2.228 | −1.130 | 0.976 | −0.943 | 0. | 0. | $p_y$ |
|  | 0. | 0. | 0. | −1.381 | −1.275 | 0.647 | −0.943 | −0.132 | 0. | 0. | $p_z$ |
|  | 0. | 0. | 0. | 0. | −0.742 | 1.709 | 0. | 0. | 0. | 0. | $s$ |
|  | 0. | 0. | 0. | 0. | −1.710 | 2.076 | 0. | 0. | 0. | 0. | $p_x$ |
|  | 0. | 0. | 0. | 0. | 0. | 0. | −1.381 | 0. | 0. | 0. | $p_y$ |
|  | 0. | 0. | 0. | 0. | 0. | 0. | 0. | −1.381 | 0. | 0. | $p_z$ |
|  | 0. | 0. | 0. | 0. | 0. | 0. | 0. | 0. | 0. | 0. | $s_H$ |
|  | 0. | 0. | 0. | 0. | 0. | 0. | 0. | 0. | 0. | 0. | $s_H$ |

$\mathbf{h}_{0,1} =$

|  | $s$ | $p_x$ | $p_y$ | $p_z$ | $s$ | $p_x$ | $p_y$ | $p_z$ | $s_H$ | $s_H$ |  |
|---|---|---|---|---|---|---|---|---|---|---|---|
|  | −0.064 | 0. | 0.692 | 0. | −2.822 | −1.527 | 2.228 | 1.275 | 0. | 0. | $s$ |
|  | 0. | −0.428 | 0. | 0. | 1.527 | 0.102 | −1.130 | −0.647 | 0. | 0. | $p_x$ |
|  | −0.692 | 0. | 0.993 | 0. | −2.228 | −1.130 | 0.976 | 0.943 | 0. | 0. | $p_y$ |
|  | 0. | 0. | 0. | −0.428 | −1.275 | −0.647 | 0.943 | −0.132 | 0. | 0. | $p_z$ |
|  | 0. | 0. | 0. | 0. | −0.064 | 0. | 0.692 | 0. | 0. | 0. | $s$ |
|  | 0. | 0. | 0. | 0. | 0. | −0.428 | 0. | 0. | 0. | 0. | $p_x$ |
|  | 0. | 0. | 0. | 0. | −0.692 | 0. | 0.993 | 0. | 0. | 0. | $p_y$ |
|  | 0. | 0. | 0. | 0. | 0. | 0. | 0. | −0.428 | 0. | 0. | $p_z$ |
|  | 0. | 0. | 0. | 0. | 0. | 0. | 0. | 0. | 0. | 0. | $s_H$ |
|  | 0. | 0. | 0. | 0. | 0. | 0. | 0. | 0. | 0. | 0. | $s_H$ |

$$\mathbf{h}_{1,1} =$$

| | $s$ | $p_x$ | $p_y$ | $p_z$ | $s$ | $p_x$ | $p_y$ | $p_z$ | $s_H$ | $s_H$ | |
|---|---|---|---|---|---|---|---|---|---|---|---|
| | 0. | 0. | 0. | 0. | −2.822 | 1.527 | 2.228 | 1.275 | 0. | 0. | $s$ |
| | 0. | 0. | 0. | 0. | −1.527 | 0.102 | 1.130 | 0.647 | 0. | 0. | $p_x$ |
| | 0. | 0. | 0. | 0. | −2.228 | 1.130 | 0.976 | 0.943 | 0. | 0. | $p_y$ |
| | 0. | 0. | 0. | 0. | −1.275 | 0.647 | 0.943 | −0.132 | 0. | 0. | $p_z$ |
| | 0. | 0. | 0. | 0. | 0. | 0 | 0 | 0 | 0 | 0 | $s$ |
| | 0 | 0 | 0 | 0 | 0 | 0 | 0 | 0 | 0 | 0 | $p_x$ |
| | 0 | 0 | 0 | 0 | 0 | 0 | 0 | 0 | 0 | 0 | $p_y$ |
| | 0 | 0 | 0 | 0 | 0 | 0 | 0 | 0 | 0 | 0 | $p_z$ |
| | 0 | 0 | 0 | 0 | 0 | 0 | 0 | 0 | 0 | 0 | $s_H$ |
| | 0 | 0 | 0 | 0 | 0 | 0 | 0 | 0 | 0 | 0 | $s_H$ |

and for the overlap matrix we have

$$\mathbf{s}_{0,0} =$$

| $s$ | $p_x$ | $p_y$ | $p_z$ | $s$ | $p_x$ | $p_y$ | $p_z$ | $s_H$ | $s_H$ |
|---|---|---|---|---|---|---|---|---|---|
| 1 | 0 | 0 | 0 | −0.049 | 0.003 | 0.005 | −0.003 | −0.113 | 0 |
| 0 | 1 | 0 | 0 | −0.003 | −0.031 | −0.060 | 0.034 | 0 | 0 |
| 0 | 0 | 1 | 0 | −0.005 | −0.060 | −0.077 | 0.050 | 0 | 0 |
| 0 | 0 | 0 | 1 | 0.003 | 0.034 | 0.050 | −0.019 | −0.347 | 0 |
| −0.049 | −0.003 | −0.005 | 0.003 | 1 | 0 | 0 | 0 | 0 | −0.113 |
| 0.003 | −0.031 | −0.060 | 0.034 | 0 | 1 | 0 | 0 | 0 | 0 |
| 0.005 | −0.060 | −0.077 | 0.050 | 0 | 0 | 1 | 0 | 0 | 0 |
| −0.003 | 0.034 | 0.050 | −0.019 | 0 | 0 | 0 | 1 | 0 | 0.347 |
| −0.113 | 0 | 0 | −0.347 | 0 | 0 | 0 | 0 | 1 | 0 |
| 0 | 0 | 0 | 0 | −0.113 | 0 | 0 | 0.347 | 0 | 1 |

$$\mathbf{s}_{1,0} =$$

| | $s$ | $p_x$ | $p_y$ | $p_z$ | $s$ | $p_x$ | $p_y$ | $p_z$ | $s_H$ | $s_H$ | |
|---|---|---|---|---|---|---|---|---|---|---|---|
| | 0.150 | −0.212 | 0 | 0 | −0.049 | −0.003 | 0.005 | −0.003 | 0 | 0 | $s$ |
| | 0.212 | −0.421 | 0 | 0 | 0.003 | −0.031 | 0.060 | −0.034 | 0 | 0 | $p_x$ |
| | 0 | 0 | 0.049 | 0 | −0.005 | 0.060 | −0.077 | 0.050 | 0 | 0 | $p_y$ |
| | 0 | 0 | 0 | 0.049 | 0.002 | −0.034 | 0.050 | −0.019 | 0 | 0 | $p_z$ |
| | 0 | 0 | 0 | 0 | 0.150 | −0.212 | 0 | 0 | 0 | 0 | $s$ |
| | 0 | 0 | 0 | 0 | 0.212 | −0.421 | 0 | 0 | 0 | 0 | $p_x$ |
| | 0 | 0 | 0 | 0 | 0 | 0 | 0.049 | 0 | 0 | 0 | $p_y$ |
| | 0 | 0 | 0 | 0 | 0 | 0 | 0 | 0.049 | 0 | 0 | $p_z$ |
| | 0 | 0 | 0 | 0 | 0 | 0 | 0 | 0 | 0 | 0 | $s_H$ |
| | 0 | 0 | 0 | 0 | 0 | 0 | 0 | 0 | 0 | 0 | $s_H$ |

$$
\mathbf{s}_{0,1} =
\begin{array}{c}
\begin{array}{cccccccccc}
s & p_x & p_y & p_z & s & p_x & p_y & p_z & s_H & s_H
\end{array} \\
\left(
\begin{array}{cccccccccc}
0.062 & 0 & -0.102 & 0 & -0.049 & 0.003 & -0.005 & -0.003 & 0 & 0 \\
0 & 0.037 & 0 & 0 & -0.003 & -0.031 & 0.060 & 0.034 & 0 & 0 \\
0.102 & 0 & -0.056 & 0 & 0.005 & 0.060 & -0.077 & -0.050 & 0 & 0 \\
0 & 0 & 0 & 0.037 & 0.003 & 0.034 & -0.050 & -0.019 & 0 & 0 \\
0 & 0 & 0 & 0 & 0.062 & 0 & -0.102 & 0 & 0 & 0 \\
0 & 0 & 0 & 0 & 0 & 0.037 & 0 & 0 & 0 & 0 \\
0 & 0 & 0 & 0 & 0.102 & 0 & -0.056 & 0 & 0 & 0 \\
0 & 0 & 0 & 0 & 0 & 0 & 0 & 0.037 & 0 & 0 \\
0 & 0 & 0 & 0 & 0 & 0 & 0 & 0 & 0 & 0 \\
0 & 0 & 0 & 0 & 0 & 0 & 0 & 0 & 0 & 0
\end{array}
\right)
\begin{array}{c}
s \\ p_x \\ p_y \\ p_z \\ s \\ p_x \\ p_y \\ p_z \\ s_H \\ s_H
\end{array}
\end{array}
$$

$$
\mathbf{s}_{1,1} =
\begin{array}{c}
\begin{array}{cccccccccc}
s & p_x & p_y & p_z & s & p_x & p_y & p_z & s_H & s_H
\end{array} \\
\left(
\begin{array}{cccccccccc}
0 & 0 & 0 & 0 & -0.049 & -0.003 & -0.005 & -0.003 & 0 & 0 \\
0 & 0 & 0 & 0 & 0.003 & -0.031 & -0.060 & -0.034 & 0 & 0 \\
0 & 0 & 0 & 0 & 0.005 & -0.060 & -0.077 & -0.050 & 0 & 0 \\
0 & 0 & 0 & 0 & 0.003 & -0.034 & -0.050 & -0.019 & 0 & 0 \\
0 & 0 & 0 & 0 & 0 & 0 & 0 & 0 & 0 & 0 \\
0 & 0 & 0 & 0 & 0 & 0 & 0 & 0 & 0 & 0 \\
0 & 0 & 0 & 0 & 0 & 0 & 0 & 0 & 0 & 0 \\
0 & 0 & 0 & 0 & 0 & 0 & 0 & 0 & 0 & 0 \\
0 & 0 & 0 & 0 & 0 & 0 & 0 & 0 & 0 & 0 \\
0 & 0 & 0 & 0 & 0 & 0 & 0 & 0 & 0 & 0
\end{array}
\right)
\begin{array}{c}
s \\ p_x \\ p_y \\ p_z \\ s \\ p_x \\ p_y \\ p_z \\ s_H \\ s_H
\end{array}
\end{array}
$$

APPENDIX

# C

# APPENDIX C: EXPLICIT FORM FOR THE TIGHT-BINDING HAMILTONIAN AND OVERLAP MATRIX OF B6MMM

To calculate the Hamiltonian and overlap matrix in terms of atomic orbitals we expand the Bloch functions as linear combinations of the orbitals $\varphi$ as follows

$$\psi_k(\mathbf{r}) = \sum_{v'} \sum_{i'} c_{i'v'}(k)\phi_{v,k}(\mathbf{r} - \mathbf{r}_i) \tag{C.1}$$

with

$$\phi_{v,\mathbf{k}}(\mathbf{r}) = \sum_{n \in \mathbb{Z}} \sum_{m \in \mathbb{Z}} e^{i\mathbf{k}.\mathbf{R}_{n,m}} \varphi_v(\mathbf{r} - \mathbf{R}_{n,m}) \tag{C.2}$$

in which $\mathbf{R}_{n,m}$ is the discrete translation vector of the unit cell at $(m,n)$ of the Bravais lattice. In principle, $m$ and $n$ run over an infinite array of discrete points, in this work the TB model includes only the first nearest unit cell. Table C.1 represents the 2D lattice vectors of the B6mmm structure. The atoms of the unit cell can be identified by their indexes as presented in Table C.2

and the top and bottom layers are distinguished by $\gamma = 1$ and $\gamma = -1$, respectively.

The mono-electronic Hamiltonian $H$ and the overlap matrix $S$ may be rewritten as

|   | $x$ | $y$ | $z$ |
|---|---|---|---|
| **a** | 1.422 | 2.471 | 0 |
| **b** | 1.422 | -2.471 | 0 |

Table C.1: The lattice vectors for B6mmm structure in units of Å.

| index | $\gamma$ | $x$ | $y$ | $z$ |
|---|---|---|---|---|
| 1 | -1 | 1.422 | 0.824 | 0.971 |
| 2 | -1 | 1.422 | -0.824 | 0.971 |
| 3 | -1 | 0 | 0 | 1.887 |
| 4 | 1 | 1.422 | 0.824 | 4.510 |
| 5 | 1 | 1.422 | -0.824 | 4.510 |
| 6 | 1 | 0 | 0 | 3.590 |

Table C.2: The indices and positions of the atoms in units of Å applied for constructing the TB model in this work. $\gamma = 1$ and $\gamma = -1$ means the top and bottom layers, respectively.

$$\mathbf{H} = \sum_{n=-1}^{1} \sum_{m=-1}^{1} \mathbf{h}_{n,m} e^{i\mathbf{k}.\mathbf{R}_{m,n}}, \tag{C.3}$$

where $\mathbf{R}_{m,n}$ is the translation vector of the unit cell $(m,n)$ and

$$\mathbf{S} = \sum_{n=-1}^{1} \sum_{m=-1}^{1} \mathbf{s}_{n,m} e^{i\mathbf{k}.\mathbf{R}_{m,n}}. \tag{C.4}$$

Since $\mathbf{H}$ and $\mathbf{S}$ are Hermitian therefore

$$\mathbf{h}_{-1,0} = \mathbf{h}_{1,0}^{\dagger}, \mathbf{h}_{0,-1} = \mathbf{h}_{0,1}^{\dagger},$$
$$\mathbf{h}_{-1,-1} = \mathbf{h}_{1,1}^{\dagger}, \mathbf{h}_{-1,1} = \mathbf{h}_{1,-1}^{\dagger},$$
$$\mathbf{s}_{-1,0} = \mathbf{s}_{1,0}^{\dagger}, \mathbf{s}_{0,-1} = \mathbf{s}_{0,1}^{\dagger},$$
$$\mathbf{s}_{-1,-1} = \mathbf{s}_{1,1}^{\dagger}, \mathbf{s}_{-1,1} = \mathbf{s}_{1,-1}^{\dagger}. \tag{C.5}$$

hence, we have only five independent matrices. We only need to determine the matrices $\mathbf{h}$ and $\mathbf{s}$ for the cells at $(0,0)$, $(1,0)$, $(0,1)$, $(1,1)$ and $(-1,1)$. Since the number of atoms in the unit cell is six and each atom has four orbitals the

Hamiltonian and the overlap matrix are of size $24 \times 24$. For simplicity, $\mathbf{h}_{n,m}$ and $\mathbf{s}_{n,m}$ may be written as follows

$$\mathbf{h}_{m,n} = \begin{pmatrix} \mathbf{a}_{m,n(\gamma=-1)} & \mathbf{b}^{\dagger}_{m,n} \\ \mathbf{b}_{m,n} & \mathbf{a}_{m,n(\gamma=1)} \end{pmatrix} \tag{C.6}$$

and

$$\mathbf{s}_{m,n} = \begin{pmatrix} \mathbf{c}_{m,n(\gamma=-1)} & \mathbf{d}^{\dagger}_{m,n} \\ \mathbf{d}_{m,n} & \mathbf{c}_{m,n(\gamma=1)} \end{pmatrix} \tag{C.7}$$

in which $\mathbf{a}$, $\mathbf{b}$, $\mathbf{c}$ and $\mathbf{d}$ are $12 \times 12$ matrices. We use the SK coefficients presented in the main paper and calculate the Hamiltonian and the overlap matrix and extract the matrices as follows (respectively, $\mathbf{a}_{0,0}(\gamma)$, $\mathbf{a}_{1,0}(\gamma)$, $\mathbf{a}_{0,1}(\gamma)$, $\mathbf{a}_{1,1}(\gamma)$, $\mathbf{b}_{0,0}$, $\mathbf{c}_{0,0}(\gamma)$, $\mathbf{c}_{1,0}(\gamma)$, $\mathbf{c}_{0,1}(\gamma)$, $\mathbf{c}_{1,1}(\gamma)$ and $\mathbf{d}_{0,0}$)

| $s$ | $p_x$ | $p_y$ | $p_z$ | $s$ | $p_x$ | $p_y$ | $p_z$ | $s$ | $p_x$ | $p_y$ | $p_z$ |
|---|---|---|---|---|---|---|---|---|---|---|---|
| $-3.130$ | $0$ | $0$ | $0$ | $-6.667$ | $0.001$ | $-5.527$ | $0$ | $-0.974$ | $-1.357$ | $-0.782$ | $-0.870\gamma$ |
| $0$ | $5.033$ | $0$ | $0$ | $-0.001$ | $-1.654$ | $-0.002$ | $0$ | $1.357$ | $1.077$ | $1.389$ | $1.545\gamma$ |
| $0$ | $0$ | $4.713$ | $0$ | $5.527$ | $-0.002$ | $4.707$ | $0$ | $0.782$ | $1.389$ | $-0.532$ | $0.891\gamma$ |
| $0$ | $0$ | $0$ | $1.797$ | $0$ | $0$ | $0$ | $-1.654$ | $0.870\gamma$ | $1.545\gamma$ | $0.891\gamma$ | $-0.342$ |
| $-6.667$ | $-0.001$ | $5.527$ | $0$ | $-3.130$ | $0$ | $0$ | $0$ | $-0.974$ | $-1.357$ | $0.784$ | $-0.870\gamma$ |
| $0.001$ | $-1.654$ | $-0.002$ | $0$ | $0$ | $5.033$ | $0$ | $0$ | $1.357$ | $1.075$ | $-1.392$ | $1.544\gamma$ |
| $-5.527$ | $-0.002$ | $4.707$ | $0$ | $0$ | $0$ | $4.713$ | $0$ | $-0.784$ | $-1.392$ | $-0.529$ | $-0.892\gamma$ |
| $0$ | $0$ | $0$ | $-1.654$ | $0$ | $0$ | $0$ | $1.797$ | $0.870\gamma$ | $1.544\gamma$ | $-0.892\gamma$ | $-0.344$ |
| $-0.974$ | $1.357$ | $0.782$ | $0.870\gamma$ | $-0.974$ | $1.357$ | $-0.784$ | $0.870\gamma$ | $-3.130$ | $0$ | $0$ | $0$ |
| $-1.357$ | $1.077$ | $1.389$ | $1.545\gamma$ | $-1.357$ | $1.075$ | $-1.392$ | $1.544\gamma$ | $0$ | $5.033$ | $0$ | $0$ |
| $-0.782$ | $1.389$ | $-0.532$ | $0.891\gamma$ | $0.784$ | $-1.392$ | $-0.529$ | $-0.892\gamma$ | $0$ | $0$ | $4.713$ | $0$ |
| $-0.870\gamma$ | $1.545\gamma$ | $0.891\gamma$ | $-0.342$ | $-0.870\gamma$ | $1.544\gamma$ | $-0.892\gamma$ | $-0.344$ | $0$ | $0$ | $0$ | $1.797$ |

| $s$ | $p_x$ | $p_y$ | $p_z$ | $s$ | $p_x$ | $p_y$ | $p_z$ | $s$ | $p_x$ | $p_y$ | $p_z$ | |
|---|---|---|---|---|---|---|---|---|---|---|---|---|
| $0.100$ | $0.046$ | $0.080$ | $0$ | $-6.667$ | $4.792$ | $2.755$ | $0$ | $-0.974$ | $-0.009$ | $1.565$ | $-0.873\gamma$ | $s$ |
| $-0.046$ | $-0.185$ | $0.020$ | $0$ | $-4.792$ | $3.126$ | $2.749$ | $0$ | $0.009$ | $-1.333$ | $-0.018$ | $0.010\gamma$ | $p_x$ |
| $-0.080$ | $0.020$ | $-0.162$ | $0$ | $-2.755$ | $2.749$ | $-0.073$ | $0$ | $-1.565$ | $-0.018$ | $1.871$ | $-1.788\gamma$ | $p_y$ |
| $0$ | $0$ | $0$ | $-0.197$ | $0$ | $0$ | $0$ | $-1.654$ | $0.873\gamma$ | $0.010\gamma$ | $-1.788\gamma$ | $-0.336$ | $p_z$ |
| $0$ | $0$ | $0$ | $0$ | $0$ | $0$ | $0$ | $0$ | $0$ | $0$ | $0$ | $0$ | $s$ |
| $0$ | $0$ | $0$ | $0$ | $0$ | $0$ | $0$ | $0$ | $0$ | $0$ | $0$ | $0$ | $p_x$ |
| $0$ | $0$ | $0$ | $0$ | $0$ | $0$ | $0$ | $0$ | $0$ | $0$ | $0$ | $0$ | $p_y$ |
| $0$ | $0$ | $0$ | $0$ | $0$ | $0$ | $0$ | $0$ | $0$ | $0$ | $0$ | $0$ | $p_z$ |
| $0$ | $0$ | $0$ | $0$ | $0$ | $0$ | $0$ | $0$ | $0$ | $0$ | $0$ | $0$ | $s$ |
| $0$ | $0$ | $0$ | $0$ | $0$ | $0$ | $0$ | $0$ | $0$ | $0$ | $0$ | $0$ | $p_x$ |
| $0$ | $0$ | $0$ | $0$ | $0$ | $0$ | $0$ | $0$ | $0$ | $0$ | $0$ | $0$ | $p_y$ |
| $0$ | $0$ | $0$ | $0$ | $0$ | $0$ | $0$ | $0$ | $0$ | $0$ | $0$ | $0$ | $p_z$ |

| $s$ | $p_x$ | $p_y$ | $p_z$ | $s$ | $p_x$ | $p_y$ | $p_z$ | $s$ | $p_x$ | $p_y$ | $p_z$ | |
|---|---|---|---|---|---|---|---|---|---|---|---|---|
| 0 | 0 | 0 | 0 | 0 | 0 | 0 | 0 | 0 | 0 | 0 | 0 | $s$ |
| 0 | 0 | 0 | 0 | 0 | 0 | 0 | 0 | 0 | 0 | 0 | 0 | $p_x$ |
| 0 | 0 | 0 | 0 | 0 | 0 | 0 | 0 | 0 | 0 | 0 | 0 | $p_y$ |
| 0 | 0 | 0 | 0 | 0 | 0 | 0 | 0 | 0 | 0 | 0 | 0 | $p_z$ |
| −6.667 | 4.791 | −2.757 | 0 | 0.100 | 0.046 | −0.080 | 0 | −0.974 | −0.009 | −1.564 | −0.874$\gamma$ | $s$ |
| −4.791 | 3.125 | −2.749 | 0 | −0.046 | −0.185 | −0.020 | 0 | 0.009 | −1.333 | 0.019 | 0.011$\gamma$ | $p_x$ |
| 2.757 | −2.749 | −0.072 | 0 | 0.080 | −0.020 | −0.162 | 0 | 1.564 | 0.019 | 1.869 | 1.789$\gamma$ | $p_y$ |
| 0 | 0 | 0 | −1.654 | 0 | 0 | 0 | −0.197 | 0.874$\gamma$ | 0.011$\gamma$ | 1.789$\gamma$ | −0.334 | $p_z$ |
| 0 | 0 | 0 | 0 | 0 | 0 | 0 | 0 | 0 | 0 | 0 | 0 | $s$ |
| 0 | 0 | 0 | 0 | 0 | 0 | 0 | 0 | 0 | 0 | 0 | 0 | $p_x$ |
| 0 | 0 | 0 | 0 | 0 | 0 | 0 | 0 | 0 | 0 | 0 | 0 | $p_y$ |
| 0 | 0 | 0 | 0 | 0 | 0 | 0 | 0 | 0 | 0 | 0 | 0 | $p_z$ |

| $s$ | $p_x$ | $p_y$ | $p_z$ | $s$ | $p_x$ | $p_y$ | $p_z$ | $s$ | $p_x$ | $p_y$ | $p_z$ | |
|---|---|---|---|---|---|---|---|---|---|---|---|---|
| 0.100 | 0.092 | 0 | 0 | 0 | 0 | 0 | 0 | −0.974 | 1.350 | −0.788 | −0.877$\gamma$ | $s$ |
| −0.092 | −0.150 | 0 | 0 | 0 | 0 | 0 | 0 | −1.350 | 1.050 | −1.392 | −1.548$\gamma$ | $p_x$ |
| 0 | 0 | −0.197 | 0 | 0 | 0 | 0 | 0 | 0.788 | −1.392 | −0.520 | 0.904$\gamma$ | $p_y$ |
| 0 | 0 | 0 | −0.197 | 0 | 0 | 0 | 0 | 0.877$\gamma$ | −1.548$\gamma$ | 0.904$\gamma$ | −0.327 | $p_z$ |
| 0 | 0 | 0 | 0 | 0.100 | 0.092 | 0 | 0 | −0.974 | 1.349 | 0.790 | −0.876$\gamma$ | $s$ |
| 0 | 0 | 0 | 0 | −0.092 | −0.150 | 0 | 0 | −1.349 | 1.047 | 1.394 | −1.547$\gamma$ | $p_x$ |
| 0 | 0 | 0 | 0 | 0 | 0 | −0.197 | 0 | −0.790 | 1.394 | −0.516 | −0.906$\gamma$ | $p_y$ |
| 0 | 0 | 0 | 0 | 0 | 0 | 0 | −0.197 | 0.876$\gamma$ | −1.547$\gamma$ | −0.906$\gamma$ | −0.328 | $p_z$ |
| 0 | 0 | 0 | 0 | 0 | 0 | 0 | 0 | 0 | 0 | 0 | 0 | $s$ |
| 0 | 0 | 0 | 0 | 0 | 0 | 0 | 0 | 0 | 0 | 0 | 0 | $p_x$ |
| 0 | 0 | 0 | 0 | 0 | 0 | 0 | 0 | 0 | 0 | 0 | 0 | $p_y$ |
| 0 | 0 | 0 | 0 | 0 | 0 | 0 | 0 | 0 | 0 | 0 | 0 | $p_z$ |

| $s$ | $p_x$ | $p_y$ | $p_z$ | $s$ | $p_x$ | $p_y$ | $p_z$ | $s$ | $p_x$ | $p_y$ | $p_z$ | |
|---|---|---|---|---|---|---|---|---|---|---|---|---|
| 0 | 0 | 0 | 0 | 0 | 0 | 0 | 0 | 0 | 0 | 0 | 0 | $s$ |
| 0 | 0 | 0 | 0 | 0 | 0 | 0 | 0 | 0 | 0 | 0 | 0 | $p_x$ |
| 0 | 0 | 0 | 0 | 0 | 0 | 0 | 0 | 0 | 0 | 0 | 0 | $p_y$ |
| 0 | 0 | 0 | 0 | 0 | 0 | 0 | 0 | 0 | 0 | 0 | 0 | $p_z$ |
| 0 | 0 | 0 | 0 | 0 | 0 | 0 | 0 | 0 | 0 | 0 | 0 | $s$ |
| 0 | 0 | 0 | 0 | 0 | 0 | 0 | 0 | 0 | 0 | 0 | 0 | $p_x$ |
| 0 | 0 | 0 | 0 | 0 | 0 | 0 | 0 | 0 | 0 | 0 | 0 | $p_y$ |
| 0 | 0 | 0 | 0 | 0 | 0 | 0 | 0 | 0 | 0 | 0 | 0 | $p_z$ |
| 0 | 0 | 0 | 0 | 0 | 0 | 0 | 0 | 4.560 | 0 | 0 | 1.446 | $s$ |
| 0 | 0 | 0 | 0 | 0 | 0 | 0 | 0 | 0 | 4.189 | 0 | 0 | $p_x$ |
| 0 | 0 | 0 | 0 | 0 | 0 | 0 | 0 | 0 | 0 | 4.189 | 0 | $p_y$ |
| 0 | 0 | 0 | 0 | 0 | 0 | 0 | 0 | −1.446 | 0 | 0 | −0.738 | $p_z$ |

| $s$ | $p_x$ | $p_y$ | $p_z$ | $s$ | $p_x$ | $p_y$ | $p_z$ | $s$ | $p_x$ | $p_y$ | $p_z$ |
|---|---|---|---|---|---|---|---|---|---|---|---|
| 1 | 0 | 0 | 0 | 0.379 | 0 | 0.162 | 0 | −0.126 | 0.006 | 0.003 | $0.004\gamma$ |
| 0 | 1 | 0 | 0 | 0 | 0.165 | 0 | 0 | −0.006 | −0.229 | −0.0495 | $-0.055\gamma$ |
| 0 | 0 | 1 | 0 | −0.162 | 0 | 0.202 | 0 | −0.003 | −0.050 | −0.172 | $-0.032\gamma$ |
| 0 | 0 | 0 | 1 | 0 | 0 | 0 | 0.165 | $-0.004\gamma$ | $-0.055\gamma$ | $-0.032\gamma$ | −0.178 |
| 0.379 | 0 | −0.162 | 0 | 1 | 0 | 0 | 0 | −0.126 | 0.006 | −0.003 | $0.004\gamma$ |
| 0 | 0.165 | 0 | 0 | 0 | 1 | 0 | 0 | −0.006 | −0.229 | 0.050 | $-0.055\gamma$ |
| 0.162 | 0 | 0.202 | 0 | 0 | 0 | 1 | 0 | 0.003 | 0.0496 | −0.172 | $0.032\gamma$ |
| 0 | 0 | 0 | 0.165 | 0 | 0 | 0 | 1 | $-0.004\gamma$ | $-0.055\gamma$ | $0.032\gamma$ | −0.178 |
| −0.126 | −0.006 | −0.003 | $-0.004\gamma$ | −0.126 | −0.006 | 0.003 | $-0.004\gamma$ | 1 | 0 | 0 | 0 |
| 0.006 | −0.229 | −0.0495 | $-0.055\gamma$ | 0.006 | −0.229 | 0.050 | $-0.055\gamma$ | 0 | 1 | 0 | 0 |
| 0.003 | −0.050 | −0.172 | $-0.032\gamma$ | −0.003 | 0.050 | −0.172 | $0.032\gamma$ | 0 | 0 | 1 | 0 |
| $0.004\gamma$ | $-0.055\gamma$ | $-0.032\gamma$ | −0.178 | $0.004\gamma$ | $-0.055\gamma$ | $0.032\gamma$ | −0.178 | 0 | 0 | 0 | 1 |

| $s$ | $p_x$ | $p_y$ | $p_z$ | $s$ | $p_x$ | $p_y$ | $p_z$ | $s$ | $p_x$ | $p_y$ | $p_z$ | |
|---|---|---|---|---|---|---|---|---|---|---|---|---|
| 0.035 | −0.020 | −0.034 | 0 | 0.379 | −0.141 | −0.081 | 0 | −0.126 | 0 | −0.006 | $0.004\gamma$ | $s$ |
| 0.0196 | 0.0376 | −0.042 | 0 | 0.141 | 0.193 | 0.016 | 0 | 0 | −0.143 | 0.001 | 0 | $p_x$ |
| 0.034 | −0.042 | −0.011 | 0 | 0.081 | 0.016 | 0.174 | 0 | 0.006 | 0.001 | −0.257 | $0.064\gamma$ | $p_y$ |
| 0 | 0 | 0 | 0.062 | 0 | 0 | 0 | 0.165 | $-0.004\gamma$ | 0 | $0.064\gamma$ | −0.179 | $p_z$ |
| 0 | 0 | 0 | 0 | 0 | 0 | 0 | 0 | 0 | 0 | 0 | 0 | $s$ |
| 0 | 0 | 0 | 0 | 0 | 0 | 0 | 0 | 0 | 0 | 0 | 0 | $p_x$ |
| 0 | 0 | 0 | 0 | 0 | 0 | 0 | 0 | 0 | 0 | 0 | 0 | $p_y$ |
| 0 | 0 | 0 | 0 | 0 | 0 | 0 | 0 | 0 | 0 | 0 | 0 | $p_z$ |
| 0 | 0 | 0 | 0 | 0 | 0 | 0 | 0 | 0 | 0 | 0 | 0 | $s$ |
| 0 | 0 | 0 | 0 | 0 | 0 | 0 | 0 | 0 | 0 | 0 | 0 | $p_x$ |
| 0 | 0 | 0 | 0 | 0 | 0 | 0 | 0 | 0 | 0 | 0 | 0 | $p_y$ |
| 0 | 0 | 0 | 0 | 0 | 0 | 0 | 0 | 0 | 0 | 0 | 0 | $p_z$ |

| $s$ | $p_x$ | $p_y$ | $p_z$ | $s$ | $p_x$ | $p_y$ | $p_z$ | $s$ | $p_x$ | $p_y$ | $p_z$ | |
|---|---|---|---|---|---|---|---|---|---|---|---|---|
| 0 | 0 | 0 | 0 | 0 | 0 | 0 | 0 | 0 | 0 | 0 | 0 | $s$ |
| 0 | 0 | 0 | 0 | 0 | 0 | 0 | 0 | 0 | 0 | 0 | 0 | $p_x$ |
| 0 | 0 | 0 | 0 | 0 | 0 | 0 | 0 | 0 | 0 | 0 | 0 | $p_y$ |
| 0 | 0 | 0 | 0 | 0 | 0 | 0 | 0 | 0 | 0 | 0 | 0 | $p_z$ |
| 0.379 | −0.141 | 0.081 | 0 | 0.035 | −0.020 | 0.034 | 0 | −0.126 | 0 | 0.006 | $0.004\gamma$ | $s$ |
| 0.141 | 0.193 | −0.016 | 0 | 0.020 | 0.038 | 0.042 | 0 | 0 | −0.143 | −0.001 | 0 | $p_x$ |
| −0.081 | −0.016 | 0.174 | 0 | −0.034 | 0.042 | −0.011 | 0 | −0.006 | −0.001 | −0.257 | $-0.064\gamma$ | $p_y$ |
| 0 | 0 | 0 | 0.165 | 0 | 0 | 0 | 0.062 | $-0.004\gamma$ | 0 | $-0.064\gamma$ | −0.179 | $p_z$ |
| 0 | 0 | 0 | 0 | 0 | 0 | 0 | 0 | 0 | 0 | 0 | 0 | $s$ |
| 0 | 0 | 0 | 0 | 0 | 0 | 0 | 0 | 0 | 0 | 0 | 0 | $p_x$ |
| 0 | 0 | 0 | 0 | 0 | 0 | 0 | 0 | 0 | 0 | 0 | 0 | $p_y$ |
| 0 | 0 | 0 | 0 | 0 | 0 | 0 | 0 | 0 | 0 | 0 | 0 | $p_z$ |

| $s$ | $p_x$ | $p_y$ | $p_z$ | $s$ | $p_x$ | $p_y$ | $p_z$ | $s$ | $p_x$ | $p_y$ | $p_z$ | |
|---|---|---|---|---|---|---|---|---|---|---|---|---|
| 0.035 | −0.039 | 0 | 0 | 0 | 0 | 0 | 0 | −0.126 | −0.005 | 0.003 | $0.004\gamma$ | $s$ |
| 0.039 | −0.035 | 0 | 0 | 0 | 0 | 0 | 0 | 0.005 | −0.228 | 0.050 | $0.055\gamma$ | $p_x$ |
| 0 | 0 | 0.062 | 0 | 0 | 0 | 0 | 0 | −0.003 | 0.050 | −0.172 | $-0.032\gamma$ | $p_y$ |
| 0 | 0 | 0 | 0.0617 | 0 | 0 | 0 | 0 | $-0.004\gamma$ | $0.055\gamma$ | $-0.032\gamma$ | −0.179 | $p_z$ |
| 0 | 0 | 0 | 0 | 0.035 | −0.039 | 0 | 0 | −0.126 | −0.005 | −0.003 | $0.004\gamma$ | $s$ |
| 0 | 0 | 0 | 0 | 0.039 | −0.035 | 0 | 0 | 0.005 | −0.228 | −0.050 | $0.055\gamma$ | $p_x$ |
| 0 | 0 | 0 | 0 | 0 | 0 | 0.062 | 0 | 0.003 | −0.050 | −0.172 | $0.032\gamma$ | $p_y$ |
| 0 | 0 | 0 | 0 | 0 | 0 | 0 | 0.062 | $-0.004\gamma$ | $0.055\gamma$ | $0.032\gamma$ | −0.179 | $p_z$ |
| 0 | 0 | 0 | 0 | 0 | 0 | 0 | 0 | 0 | 0 | 0 | 0 | $s$ |
| 0 | 0 | 0 | 0 | 0 | 0 | 0 | 0 | 0 | 0 | 0 | 0 | $p_x$ |
| 0 | 0 | 0 | 0 | 0 | 0 | 0 | 0 | 0 | 0 | 0 | 0 | $p_y$ |
| 0 | 0 | 0 | 0 | 0 | 0 | 0 | 0 | 0 | 0 | 0 | 0 | $p_z$ |

| $s$ | $p_x$ | $p_y$ | $p_z$ | $s$ | $p_x$ | $p_y$ | $p_z$ | $s$ | $p_x$ | $p_y$ | $p_z$ | |
|---|---|---|---|---|---|---|---|---|---|---|---|---|
| 0 | 0 | 0 | 0 | 0 | 0 | 0 | 0 | 0 | 0 | 0 | 0 | $s$ |
| 0 | 0 | 0 | 0 | 0 | 0 | 0 | 0 | 0 | 0 | 0 | 0 | $p_x$ |
| 0 | 0 | 0 | 0 | 0 | 0 | 0 | 0 | 0 | 0 | 0 | 0 | $p_y$ |
| 0 | 0 | 0 | 0 | 0 | 0 | 0 | 0 | 0 | 0 | 0 | 0 | $p_z$ |
| 0 | 0 | 0 | 0 | 0 | 0 | 0 | 0 | 0 | 0 | 0 | 0 | $s$ |
| 0 | 0 | 0 | 0 | 0 | 0 | 0 | 0 | 0 | 0 | 0 | 0 | $p_x$ |
| 0 | 0 | 0 | 0 | 0 | 0 | 0 | 0 | 0 | 0 | 0 | 0 | $p_y$ |
| 0 | 0 | 0 | 0 | 0 | 0 | 0 | 0 | 0 | 0 | 0 | 0 | $p_z$ |
| 0 | 0 | 0 | 0 | 0 | 0 | 0 | 0 | −0.193 | 0 | 0 | 0.054 | $s$ |
| 0 | 0 | 0 | 0 | 0 | 0 | 0 | 0 | 0 | −0.047 | 0 | 0 | $p_x$ |
| 0 | 0 | 0 | 0 | 0 | 0 | 0 | 0 | 0 | 0 | −0.047 | 0 | $p_y$ |
| 0 | 0 | 0 | 0 | 0 | 0 | 0 | 0 | −0.054 | 0 | 0 | −0.017 | $p_z$ |

and $\mathbf{b}_{1,0} = \mathbf{b}_{0,1} = \mathbf{b}_{1,1} = \mathbf{d}_{1,0} = \mathbf{d}_{0,1} = \mathbf{d}_{1,1} = \mathbf{0}$. The values are presented in unit of $eV$ and note that the indices of the elements of the Hamiltonian and the overlap matrix are the same as the indices presented in table C.2. We constructed the TB model up to the third nearest neighbor so there is no interaction between cells $(0,0)$ and $(-1,1)$, and therfore $\mathbf{h}_{-1,1} = \mathbf{s}_{-1,1} = \mathbf{0}$. Other elements of the coupling matrices can be found from the relation Eq. (C.5).

# BIBLIOGRAPHY

[1]     Gleiter H. Acta Mater **48**, 1 (2000).

[2]     Skorokhod V, Ragulya A, Uvarova I. Physico-chemical kinetics in nanostructured systems. Kyiv: Academperiodica, 180 (2001).

[3]     Pokropivny VV, Skorokhod VV. Mater Sci Eng C **27**, 990 (2007).

[4]     Armand M, Tarascon JM. Nature **451**, 652 (2008).

[5]     Winter M, Brodd RJ. Chem Rev. **104**, 4245 (2004).

[6]     Hu LB, Choi JW, Yang Y, Jeong S, La Mantia F, Cui LF, et al. Proc Natl Acad Sci USA **106**, 21490 (2009).

[7]     Kamarudin SK, Achmad F, Daud WRW. Int J Hydrogen Energy **34**, 6902 (2009).

[8]     Ren X, Zelenay P, Thomas S, Davey J, Gottesfeld S. J Power Sources **86**, 111 (2000).

[9]     Arico AS, Bruce P, Scrosati B, Tarascon JM, Van Schalkwijk W. Nature Mater **4**, 366 (2005).

[10]    Ferreira-Aparicio P, Folgado MA, Daza L. J Power Sources **192**, 57 (2009).

[11]    de Oliveira EC, Pires CTGVMT, Pastore HO. J Braz Chem Soc **17**, 16 (2006).

[12]    Jin YH, Lee SH, Shim HW, Ko KH, Kim WD. Electrochim Acta **55**, 7315 (2010).

[13]    Dong Z, Kennedy SJ, Wu Y. J Power Sources **196**, 4886 (2011).

[14]    Hu CC, Chang KH, Lin MC, Wu YT. Nano Lett **6**, 2690 (2006).

[15]    Chen H, Cong TN, Yang W, Tan C, Li Y, Ding Y. Prog Nat Sci **19**, 291 (2009).

[16]    Li HQ, Wang YG, Wang CX, Xia YY. J Power Sources **185**, 1557 (2008).

[17]    Jun JW, Seo JW, Oh SJ, Cheon J. Coord Chem Rev **249**, 1766 (2005).

[18]   Kim KS et al. Nature **457**, 706 (2009).

[19]   Bae S et al. Nature Nanotechnol **5**, 574 (2010).

[20]   Pradhan D, Leung KT. J Phys Chem C **112**, 1357 (2008).

[21]   Tiwari JN, Pan FM, Tiwari RN, Nandi SK. Chem Commun **6**, 516 (2008).

[22]   Nayak BB, Behera D, Mishra BK. J Am Ceram Soc **93**, 3080 (2010).

[23]   Dong X, Ji X, Jing J, Li M, Li J, Yang W. J Phys Chem C **114**, 2070 (2010).

[24]   Mann AKP, Skrabalak SE. Chem Mater **23**, 1017 (2011).

[25]   Siril PF, Ramos L, Beaunier P, Archirel P, Etcheberry A, Remita H. Chem Mater **21**, 5170 (2009).

[26]   Vizireanu S, Stoica SD, Luculescu C, Nistor LC, Mitu B, Dinescu G. Plasma Sources Sci Technol **19**, 034016 (2010).

[27]   Jung SH, Oh E, Lee KH, Yang Y, Park CG, Park W, et al. Cryst Growth Des **8**, 265 (2008).

[28]   Kittel, Charles (1996). Introduction to Solid State Physics. New York: Wiley. ISBN 0-471-14286-7.

[29]   Katsuda, A.; Sunada, T Amer., J. Math. **110**, 145 (1987).

[30]   Kuchment, P., RUSS MATH SURV. **37**, 1 (1982).

[31]   Kotani M, Sunada T., Comm. Math. Phys. 209, 633 (2000).

[32]   PY Yu and M Cardona, *"Tight-binding or LCAO approach to the band structure of semiconductors"*, (Fundamentals of Semiconductors, Springer, 2005).

[33]   Orfried Madelung, *Introduction to Solid-State Theory*, (Springer-Verlag, Berlin Heidelberg, 1978).

[34]   Alexander Altland and Ben Simons, *Interaction effects in the tight-binding system*, (Condensed Matter Field Theory. Cambridge University Press, 2006).

[35]   J. C. Slater and G. F. Koster, Phys. Rev. **94**, 1498 (1954).

[36]   A. R. Leach, *Molecular modelling: principles and applications*, (Harlow, Prentice Hall, 2001).

[37]   T. Ozaki, K. Nishio, and H. Kino, Phys. Rev. B **81**, 035116 (2010).

[38]  G. Kresse and J. Hafner Phys. Rev. B **47**, 558 (1993).

[39]  G. Kresse and J. Furthmuller, Comput. Mater. Sci. **6**, 15 (1993).

[40]  G. Kresse and J. Furthmuller, Phys. Rev. B **54**, 11169 (1993).

[41]  S. Scandolo, P. Giannozzi, C. Cavazzoni, S. de Gironcoli, A. Pasquarello, and S. Baroni, Z. Kristallogr. Cryst. Mater. **220**, 574 (2005).

[42]  X. Gonze, J.M. Beuken, R. Caracas, F. Detraux, M. Fuchs, G.M. Rignanese, L. Sindic, M. Verstraete, G. Zerah, F. Jollet, and M. Torrent, Comput. Mat. Sci. **25**, 478 (2002).

[43]  T. Clark and R. Koch, *Linear Combination of Atomic Orbitals* (Springer, Berlin, Heidelberg, 1999).

[44]  G. Grosso, *Giuseppe Pastori Parravicini-Solid State Physics*, 2rd edn. (Academic Press, 2013).

[45]  G. J. Ackland, M. W. Finnis and V. Vitek, Journal of Physics F: Metal Physics **18**, 153 (1988).

[46]  C M Goringedag, D R Bowlerdag, and E Hernándezddag Rep. Prog. Phys. **60**, 12, 1447 (1997).

[47]  J. Smart and S. Csomor, *Cross-platform GUI programming with wxWidgets* (Prentice Hall Professional, 2005).

[48]  C. L. Lawson, R. J. Hanson, D. Kincaid, and F. T. Krogh, ACM Trans. Math. Software **5**, 308 (1979).

[49]  E. Anderson, Z. Bai, C. Bischof, S. Blackford, J. Demmel, J. Dongarra, J. Du Croz, A. Greenbaum, S. Hammarling, A. McKenney and D. Sorensen, *LAPACK User's Guide*, 3rd edn. (Philadelphia, PA, 1999).

[50]  M. Woo, J. Neider, T. Davis, and D. Shreiner, *OpenGL programming guide: the official guide to learning OpenGL* (Addison-Wesley Longman Publishing Co., Inc. 1999).

[51]  K. Lendi, Phys. Rev. B **9**, 2433 (1974).

[52]  F. Herman, C.D. Kuglin, K.F. Cuff, and R.L. Kortum, Phys. Rev. Lett. **11**, 541 (1963).

[53]  H.J. Noh, H. Koh, S.J. Oh, J.H. Park, H.D. Kim, J.D. Rameau, T. Valla, T.E. Kidd, P.D. Johnson, Y. Hu, and Q. Li, EPL (Europhysics Letters) **81**, 57006 (2008).

[54]  G. Dresselhaus, Physical Review **100**, 580 (1955).

[55]  M. Sakano, M.S. Bahramy, A. Katayama, T. Shimojima, H. Murakawa, Y. Kaneko, W. Malaeb, S. Shin, K. Ono, H. Kumigashira, and R. Arita, Phys. Rev. Lett. **110**, 107204 (2013).

[56]  B.A. Bernevig, T.L. Hughes, and S.C. Zhang, Science **314**, 1757 (2006).

[57]  A.V. Shevelkov, E.V. Dikarev, R.V. Shpanchenko, and B.A. Popovkin, J. Solid State Chem. **114**, 379 (1995).

[58]  D. Moldovan, M. Anđelković, and F. Peeters, *PyBinding: A Python package for tight-binding calculations*, *DOI: 10.5281/zenodo.826942*

[59]  S. M. João, M. Anđelković, L. Covaci, T. Rappoport, J.M.V.P. Lopes, and A. Ferreira, *DOI: 10.5281/zenodo.3245011*

[60]  C. W. Groth, M. Wimmer, A. R. Akhmerov, X. Waintal, Kwant: a software package for quantum transport, New J. Phys. **16**, 063065 (2014).

[61]  Z. Fan, V. Vierimaa, and A. Harju, Comput. Phys. Commun. **230**, 113 (2018).

[62]  K. Björnson, SoftwareX **9**, 205 (2019).

[63]  S. Coh and D. Vanderbilt, Python tight binding (PythTB) code. (2018).

[64]  Q. Wu, S. Zhang, H.F. Song, M. Troyer, and A.A. Soluyanov, Comput. Phys. Commun. **224**, 405 (2018).

[65]  I. Souza, N. Marzari, and D. Vanderbilt, Phys. Rev. B **65**, 035109 (2001).

[66]  A.A. Mostofi, J.R. Yates, G. Pizzi, Y.S. Lee, I. Souza, D. Vanderbilt, and N. Marzari, Comput. Phys. Commun. **185**, 2309 (2014).

[67]  B. A. Bernevig and T. L. Hughes, *Topological Insulators and Topological Superconductors* (Princeton University Press, 2013).

[68]  F. D. M. Haldane, Phys. Rev. Lett. **61**, 2015 (1988).

[69]  H. Zhang, C.-X. Liu, X.-L. Qi, X. Dai, Z. Fang, and S.-C. Zhang, Nat. Phys. **5**, 438 (2009).

[70]  Y. Xia, D. Qian, D. Hsieh, L. Wray, A. Pal, H. Lin, A. Bansil, D. Grauer, Y. S. Hor, R. J. Cava, and M. Z. Hasan, Nat. Phys. **5**, 398 (2009).

[71]    C. L. Kane and E. J. Mele, Phys. Rev. Lett. **95**, 146802 (2005).

[72]    V. Derakhshan and S. A. Ketabi, Physica E **85**, 253 (2017).

[73]    B. Feng, B. Fu, S. Kasamatsu, S. Ito, P., Cheng, C. C. Liu, Y. Feng, S. Wu, S. K. Mahatha, P. Sheverdyaeva, and P. Moras, Nature Communications **8**, 1007 (2017).

[74]    A. J. Mannix, X.-F. Zhou, B. Kiraly, J. D. Wood, D. Alducin, B. D. Myers, X. Liu, B. L. Fisher, U. Santiago, J. R. Guest, M. J. Yacaman, A. Ponce, A. R. Oganov, M. C. Hersam, and N. P. Guisinger, Science **350**, 1513 (2015).

[75]    Z. H. Zhang, A. J. Mannix, Z. L. Hu, B. Kiraly, N. P. Guisinger, M. C. Hersam, and B. I. Yakobson, Nano Lett. **16**, 6622 (2016).

[76]    Q. Zhong, L. Kong, J. Gou, W. Li, S. Sheng, S. Yang, P. Cheng, H. Li, K. Wu, and L. Chen, Phys. Rev. Mater. **1**, 021001 (2017).

[77]    Q. Zhong, J. Zhang, P. Cheng, B. Feng, W. Li, S. Sheng, H. Li, S. Meng, L. Chen, and K. J. Wu, J. of Phys.: Condens. Matter **29**, 095002 (2017).

[78]    A. Lopez-Bezanilla and P. B. Littlewood, Phys. Rev. B **93**, 241405 (2016).

[79]    N. G. Szwacki, Nanoscale Res. Lett. **3**, 49 (2008).

[80]    Z.A. Piazza, H.S. Hu, W.L. Li, Y.F. Zhao, J. Li, and L.S. Wang, Nat. Commun. **5**, 3113 (2014).

[81]    H. Tang and S. Ismail-Beigi, Phys. Rev. Let. **99**, 115501 (2007).

[82]    H. Tang and S. Ismail-Beigi, Phys. Rev. B **80**, 134113 (2009).

[83]    L.C. Xu, A. Du, and L. Kou, Phys. Chem. Chem. Phys. **18**, 27284 (2016).

[84]    C. C. Liu, H. Jiang, and Y. Yao, Phys. Rev. B **84**, 195430 (2011).

[85]    D. A. Papaconstantopoulos and M. J. Mehl, J. of Phys.: Condens. Matter **15**, R413. (2003).

[86]    K. Levenberg, Quarterly of Applied Mathematics **2**, 164 (1944).

[87]    T. Kwiatkowski, S. Olszewski, and A. Wierzbicki, Int. J. Quantum Chem. **11**, 21 (1977).

[88]    W. C. Lu, C. Z. Wang, K. Ruedenberg, and K. M. Ho, Phys. Rev. B **72**,

205123 (2005).

[89]     C. M. Goringe, D. R. Bowler, and E. Hernandez, Reports on Progress in Physics **60**, 1447 (1997).

[90]     W. Kutzelnigg, Journal of Molecular Structure: THEOCHEM **169**, 403 (1988).

[91]     S. D. Deshpande and R. B. Pode, American Journal of Physics **56**, 362 (1988).

[92]     R. W. Jansen and O. F. Sankey, Phys. Rev. B **36**, 6520 (1987).

[93]     J. P. Perdew, K. Burke, and M. Ernzerhof, Phys. Rev. Let. **77**, 3865 (1996).

[94]     A. D. Becke, Phys. Rev. A **38**, 3098 (1988).

[95]     A. C. Neto, F. Guinea, N. M. Peres, K. S. Novoselov, and A. K. Geim, Rev. Mod. Phys. **81**, 109 (2009).

[96]     T. C. Harman, M. P. Walsh and G. W. Turner, Journal of electronic materials **34**, 19 (2005).

[97]     G. K. H. Madsen, D. J. Singh, Comput. Phys. Commun. **175**, 67 (2006).

[98]     P. Giannozzi and et al., J. Phys.:Condens. Matter **21**, 395502 (2009).

[99]     P. E. Blochl, Phys. Rev. B **50**, 17953 (1994).

[100]   P. Gorai, V. Stevanović, and E. S. Toberer, Nature Reviews Materials **2**, (2017).

[101]   A. Yamamoto, K. Ogawa and T. Takeuchi, Materials Transactions **52**, 1539 (2011).

[102]   Z. Wang, Y. Sun, X. Q. Chen, C. Franchini, G. Xu, H. Weng, X. Dai, and Z. Fang, Phys. Rev. B **85**, 195320 (2012).

[103]   Z. Wang, H. Weng, Q. Wu, X. Dai, and Z. Fang, Phys. Rev. B **88**, 125427 (2013).

[104]   H. B. Nielsen and M. Ninomiya, Phys. Lett. B **130**, 389 (1983).

[105]   L. Balents, Physics **4**, 36 (2011).

[106]   X. Wan, A. M. Turner, A. Vishwanath, and S. Y. Savrasov, Phys. Rev. B **83**, 205101 (2011).

[107]   G. Xu, H. Weng, Z. Wang, X. Dai, and Z. Fang, Phys. Rev. Lett. **107**, 186806 (2011).

[108] C. Fang, Y. Chen, H. Y. Kee, and L. Fu, Phys. Rev. B **92**, 081201 (2015).

[109] A. A. Burkov, M. D. Hook, and L. Balents, Phys. Rev. B **84**, 235126 (2011).

[110] H. Weng, Y. Liang, Q. Xu, R. Yu, Z. Fang, X. Dai, and Y. Kawazoe, Phys. Rev. B **92**, 045108 (2015).

[111] J. T. Wang, H. Weng, S. Nie, Z. Fang, Y. Kawazoe, and C. Chen, Phys. Rev. Lett. **116**, 195501 (2016).

[112] R. Li, H. Ma, X. Cheng, S. Wang, D. Li, Z. Zhang, Y. Li, and X. Q. Chen, Phys. Rev. Lett. **117**, 096401 (2016).

[113] J. L. Lu, W. Luo, X. Y. Li, S. Q. Yang, J. X. Cao, X. G. Gong, and H. J. Xiang, Chinese Physics Letters **34**, 057302 (2017).

[114] J. Zhao, R. Yu, H. Weng, and Z. Fang, Phys. Rev. B **94**, 195104 (2016).

[115] K. Mullen, B. Uchoa, and D. T. Glatzhofer, Phys. Rev. Lett. **115**, 026403 (2015).

[116] M. Ezawa, Phys. Rev. Lett. **116**, 127202 (2016).

[117] N. B. Kopnin, T. T. Heikkila, and G. E. Volovik, Phys. Rev. B **83**, 220503 (2011).

[118] G. E. Volovik, Phys. Scr. **T164**, 014014 (2015).

[119] T. T. Heikkilä and G. E. Volovik, Springer, Cham. , 123 (2016).

[120] R. Yu, H. Weng, Z. Fang, X. Dai, and X. Hu, Phys. Rev. Lett. **115**, 036807 (2015).

[121] Q. Xu, R. Yu, Z. Fang, X. Dai, and H. Weng, Phys. Rev. B **95**, 045136 (2017).

[122] L. S. Xie, L. M. Schoop, E. M. Seibel, Q. D. Gibson, W. Xie, and R. J. Cava, APL Mater. **3**, 83602 (2015).

[123] G. Bian, T. R. Chang, H. Zheng, S. Velury, S. Y. Xu, T. Neupert, C. K. Chiu, S. M. Huang, D. S. Sanchez, I. Belopolski, N. Alidoust, P.J. Chen, G. Chang, A. Bansil, H. T. Jeng, H. Lin, and M. Z. Hasan, Phys. Rev. B **93**, 121113 (2016).

[124] Z. Yan, P. W. Huang, and Z. Wang, Phys. Rev. B **93**, 085138 (2016).

[125] J. W. Rhim and Y. B. Kim, Phys. Rev. B **92**, 045126 (2015).

[126] S. M. Huang, S. Y. Xu, I. Belopolski, C. C. Lee, G. Chang, B. Wang, N.

Alidoust, G. Bian, M. Neupane, C. Zhang, S. Jia, A. Bansil, H. Lin, and M. Z. Hasan, Nat. Commun. **6**, 7373 (2015).

[127]  B. Q. Lv, H. M. Weng, B. B. Fu, X. P. Wang, H. Miao, J. Ma, P. Richard, X. C. Huang, L. X. Zhao, G. F. Chen, Z. Fang, X. Dai, T. Qian, and H. Ding, Phys. Rev. X **5**, 031013 (2015).

[128]  X. Huang, L. Zhao, Y. Long, P. Wang, D. Chen, Z. Yang, H. Liang, M. Xue, H. Weng, Z. Fang, X. Dai, and G. Chen, Phys. Rev. X **5**, 031023 (2015).

[129]  B. Q. Lv, N. Xu, H. M. Weng, J. Z. Ma, P. Richard, X. C. Huang, L. X. Zhao, G. F. Chen, C. E. Matt, F. Bisti, V. N. Strocov, J. Mesot, Z. Fang, X. Dai, T. Qian, M. Shi, and H. Ding, Nat. Phys. **11**, 724 (2015).

[130]  R. Yu, Z. Fang, Z., Dai, X. and Weng, H., Frontiers of Physics, **12**, 127202 (2017).

[131]  L. Petersen, P. Hedegård, Surf. Sci. **459**, 49 (2000).

[132]  Z. K. Liu, B. Zhou, Y. Zhang, Z. J. Wang, H. M. Weng, D. Prabhakaran, S. K. Mo, Z. X. Shen, Z. Fang, X. Dai, and Z. Hussain, Science **343**, 864 (2014).

[133]  B. F. Decker and J. S. Kasper, Acta Crystallogr. **12**, 503 (1959).

[134]  Z. A. Piazza, H. S. Hu, W. L. Li, Y. F. Zhao, J. Li, and L. S. Wang, Nat. Commun. **5**, 3113 (2014).

[135]  X. F. Zhou, X. Dong, A. R. Oganov, Q. Zhu, Y. Tian, and H. T. Wang, Phys. Rev. Lett. **112**, 085502 (2014).

[136]  A. R. Oganov, J. Chen, C. Gatti, Y. Ma, Y. Ma, C. W. Glass, Z. Liu, T. Yu, O. O. Kurakevych, and V. L. Solozhenko, Nature **457**, 863 (2009).

[137]  V. Bezugly, J. Kunstmann, B. Grundkçtter-Stock, T. Frauenheim, T. Niehaus, and G. Cuniberti, ACS Nano **5**, 4997 (2011).

[138]  W. Huang, A. P. Sergeeva, H. J. Zhai, B. B. Averkiev, L. S. Wang, and A. I. Boldyrev, Nat. Chem. **2**, 202 (2010).

[139]  F. Ma, Y. Jiao, G. Gao, Y. Gu, A. Bilic, Z. Chen, and A. Du, Nano Letters **16**, 3022 (2016).

[140]  D. A. Papaconstantopoulos, *Handbook of the band structure of elemental solids* (Plenum Press, New York, 1986).

[141]  E. McCann and V. I. Fal'ko, Phys. Rev. Lett. **96**, 086805 (2006).

[142]  K. Kechedzhi, V. I. Fal'ko, E. McCann, and B. L. Altshuler, Phys. Rev. Lett. **98**, 176806 (2007).

[143]  C. Park, J. Ryou, S. Hong, B. G. Sumpter, G. Kim, and M. Yoon, Phys. Rev. Lett. **115**, 015502 (2015).

[144]  M. Z. Hasan, and C. L. Kane, Rev. Mod. Phys. **82**, 3045 (2010).

[145]  X.-L. Qi, and S.-C. Zhang, Rev. Mod. Phys. **83**, 1057 (2011).

[146]  Z. Wang, Y. Sun, X. Q. Chen, C. Franchini, G. Xu, H. Weng, X. Dai, and Z. Fang, Phys. Rev. B **85**, 195320 (2012).

[147]  Z. Wang, H. Weng, Q. Wu, X. Dai, and Z. Fang, Phys. Rev. B **88**, 125427 (2013).

[148]  H. B. Nielsen and M. Ninomiya, Phys. Lett. B **130**, 389 (1983).

[149]  L. Balents, Physics **4**, 36 (2011).

[150]  X. Wan, A. M. Turner, A. Vishwanath, and S. Y. Savrasov, Phys. Rev. B **83**, 205101 (2011).

[151]  G. Xu, H. Weng, Z. Wang, X. Dai, and Z. Fang, Phys. Rev. Lett. **107**, 186806 (2011).

[152]  C. Fang, Y. Chen, H. Y. Kee, and L. Fu, Phys. Rev. B **92**, 081201 (2015).

[153]  A. A. Burkov, M. D. Hook, and L. Balents, Phys. Rev. B **84**, 235126 (2011).

[154]  S.-Y. Xu, N. Alidoust, I. Belopolski, Zh. Yuan, G. Bian, T.-R. Chang, H. Zheng, V. N. Strocov, D. S. Sanchez, G. Chang, Ch. Zhang, D. Mou, Y. Wu, L. Huang, C.-Ch. Lee, Sh.-M. Huang, B. Wang, A. Bansil, H.-T. Jeng, T. Neupert, A. Kaminski, H. Lin, Sh. Jia, and M. Z. Hasan, Nat. Phys. **11**, 748 (2015).

[155]  B. Q. Lv, N. Xu, H. M. Weng, J. Z. Ma, P. Richard, X. C. Huang, L. X. Zhao, G. F. Chen, C. E. Matt, F. Bisti, V. N. Strocov, J. Mesot, Z. Fang, X. Dai, T. Qian, M. Shi, and H. Ding, Nat. Phys. **11**, 724 (2015).

[156]  S.-Y. Xu, I. Belopolski, N. Alidoust, M. Neupane, G. Bian, Ch. Zhang, R. Sankar, G. Chang, Zh. Yuan, C.-Ch. Lee, Sh.-M. Huang, H. Zheng, J. Ma, D. S. Sanchez, B. Wang, A. Bansil, F. Chou, P. P. Shibayev, H. Lin, Sh. Jia, and M. Z. Hasan, Science **349**, 613 (2015).

[157]  C. C. Lee, Phys. Rev. B. **92**, 235104 (2015).

[158]  Sh.-M. Huang, S.-Y. Xu, I. Belopolski, Ch.-Ch. Lee, G. Chang, B. Wang, N. Alidoust, G. Bian, M. Neupane, Ch. Zhang, Sh. Jia, A. Bansil, H. Lin, and M. Z. Hasan, Nat. Commun. **6**, 7373 (2015).

[159]  Y. Wu, L.-L. Wang, E. Mun, D. D. Johnson, D. Mou, L. Huang, Y. Lee, S. L. Bud'ko, P. C. Canfield, and A. Kaminski, Nat. Phys. **12**, 667 (2016).

[160]  G. Bian, T.-R. Chang, R. Sankar, S.-Y. Xu, H. Zheng, T. Neupert, Ch.-K. Chiu, Sh.-M. Huang, G. Chang, I. Belopolski, D. S. Sanchez, M. Neupane, N. Alidoust, Ch. Liu, B. Wang, Ch.-Ch. Lee, H.-T. Jeng, Ch. Zhang, Zh. Yuan, Sh. Jia, A. Bansil, F. Chou, H. Lin, and M. Z, Hasan, Nat. Commun. **7**, 10556 (2016).

[161]  L. M. Schoop, M. N. Ali, C. Straßer, A. Topp, A. Varykhalov, D. Marchenko, V. Duppel, S. S. P. Parkin, B. V. Lotsch, and Ch. R. Ast, Nat. Commun. **7**, 11696 (2016).

[162]  M. Neupane, I. Belopolski, M. M. Hosen, D. S. Sanchez, R. Sankar, M. Szlawska, S.-Y. Xu, K. Dimitri, N. Dhakal, P. Maldonado, P. M. Oppeneer, D. Kaczorowski, F. Chou, M. Z. Hasan, and T. Durakiewicz, Phys. Rev. B **93**, 201104 (2016).

[163]  J. Liu and L. Balents, Phys. Rev. B **95**, 075426 (2017).

[164]  Z. Yan, P. W. Huang, Z. Wang, Phys. Rev. B **93**, 085138 (2016).

[165]  L. K. Lim and R. Moessner, Phys. Rev. Lett. **118**, 016401 (2017)

[166]  S. Nie, G. Xu, F. B. Prinz, S. C. Zhang, Proc. Natl. Acad. Sci. **114**, 10596 (2017).

[167]  G. Bian, T.-R. Chang, H. Zheng, S. Velury, S.-Y. Xu, T. Neupert, Ch.-K. Chiu, Sh.-M. Huang, D. S. Sanchez, I. Belopolski, N. Alidoust, P.-J. Chen, G. Chang, A. Bansil, H.-T. Jeng, H. Lin, and M. Z. Hasan, Phys. Rev. B **93**, 121113 (2016).

[168]  L.S. Xie, L.M. Schoop, E.M. Seibel, Q.D. Gibson, W. Xie, and R.J. Cava, APL Mater. **3**, 083602 (2015).

[169]  Y.H. Chan, C.K. Chiu, M.Y. Chou, and A.P. Schnyder, Phys. Rev. B **93**, 205132 (2016).

[170]  R. Yu, H. Weng, Z. Fang, X. Dai, and X. Hu, Phys. Rev. Lett. **115**,

036807 (2015).

[171]  J.T. Wang, H. Weng, S. Nie, Z. Fang, Y. Kawazoe, and C. Chen, Phys. Rev. Lett. **116**, 195501 (2016).

[172]  R. Yu, Z. Fang, X. Dai, and H. Weng, Front. Phys. **12**, 127202 (2017).

[173]  H. Weng, X. Dai, and Z. Fang, J. Phys. Condens. Matter **28**, 303001 (2016).

[174]  N. P. Armitage, E.J. Mele, and A. Vishwanath, Rev. Mod. Phys. **90**, 015001 (2018).

[175]  Y.-J. Jin, R. Wang, J.-Zh. Zhao, Y.-P. Du, C.-D. Zheng, L.-Y. Gan, J.-F. Liu, H. Xu, and S. Y. Tong, Nanoscale **9**, 13112 (2017).

[176]  B. Yang, X. Zhang, and M. Zhao, Nanoscale **9**, 8740 (2017).

[177]  J.-L. Lu, W. Luo, X.-Y. Li, Sh.-Q. Yang, J.-X. Cao, X.-G. Gong, and H.-J. Xiang, Chin. Phys. Lett. **34**, 057302 (2017).

[178]  B. Feng, B. Fu, Sh. Kasamatsu, S. Ito, P. Cheng, Ch. Ch. Liu, Y. Feng, Sh. Wu, S. K. Mahatha, P. Sheverdyaeva, P. Moras, M. Arita, O. Sugino, T. Ch. Chiang, K. Shimada, K. Miyamoto, T. Okuda, K. Wu, L. Chen, Y. Yao, and I. Matsuda, Nat. Commun. **8**, 1007 (2017).

[179]  N. Troullier and J. Martins, Phys. Rev. B **43**, 1993 (1991).

[180]  T. Ozaki, Phys. Rev. B **67**, 155108 (2003).

[181]  T. Ozaki and H. Kino, Phys. Rev. B **69**, 195113 (2004).

[182]  H. J. Monkhorst and J. D. Pack, Phys. Rev. B **13**, 5188 (1976).

[183]  T. Bucko, J. Hafner, S. Lebegue, and J. G Angyan, J. Phys. Chem. A **43**, 11814 (2010).

[184]  J. Tersoff and D. R. Hamann, Phys. Rev. Lett. **50**, 1998 (1983).

[185]  I. Horcas, R. Fernandez, J. M Gomez-Rodriguez, J. Colchero, J. Gomez-Herrero, and A. M. Baro, Rev. Sci. Instruments **78**, 013705 (2007).

[186]  D. A. Papaconstantopoulos, *Handbook of the band structure of elemental solids* (Plenum Press, New York, 1986).

[187]  K. Levenberg, Quarterly of Applied Mathematics **2**, 164 (1944).

[188]  K. S. Novoselov, A. K. Geim, S. V. Morozov, D. Jiang, Y. Zhang, S. V. Dubonos, I. V. Grigorieva, and A. A. Firsov, Science **306**, 666 (2004).

[189] A. K. Geim and K. S. Novoselov, Nat. Mater. **6**, 183 (2007).

[190] K. K. Kim, A. Hsu, X. Jia, S. M. Kim, Y. Shi, M. Hofmann, D. Nezich, J. F. Rodriguez-Nieva, M. Dresselhaus, T. Palacios, and J. Kong, Nano Lett. **12**, 161 (2012).

[191] S. Manzeli, D. Ovchinnikov, D. Pasquier, O. V. Yazyev, and A. Kis, Nat. Rev. Mater **2**, 17033 (2017).

[192] J. N. Coleman, M. Lotya, A. O'Neill, S. D. Bergin, P. J. King, U. Khan, K. Young, A. Gaucher, S. De, R. J Smith, I. V. Shvets, S. K. Arora, G. Stanton G., H. Y. Kim, K. Lee, G. T. Kim, G. S. Duesberg, T. Hallam, J. J. Boland, J. J. Wang, J. F. Donegan, J. C. Grunlan, G. Moriarty, A. Shmeliov, R. J. Nicholls, J. M. Perkins, E. M. Grieveson, K. Theuwissen, D. W. McComb, P. D. Nellist, and V. Nicolosi, Science **331**, 568 (2011).

[193] M. Chhowalla, H. S. Shin, G. Eda, L. J. Li, K. P. Loh, and H. Zhang, Nat. Chem **5**, 263 (2013).

[194] A. Kara, H. Enriquez, A. P. Seitsonen, L. C. L. Y. Voon, S. Vizzini, B. Aufray, and Hamid Oughaddou, Surf. Science Report. **67**, 1 (2012).

[195] P. Vogt, P. Padova, C. Quaresima, J. Avila, E. Frantzeskakis, M. C. Asensio, A. Resta, B. Ealet, and G. L. Lay, Phys. Rev. Lett. **108**, 155501 (2012).

[196] P. D. Padova, O. Kubo, B. Olivieri, C. Quaresima, T. Nakayama, M. Aono, and G. Le Lay, Nano Lett. **12**, 5500 (2012).

[197] E. Bianco, S. Butler, S. Jiang, O. D. Restrepo, W. Windl, and J. E. Goldberger, ACS Nano **7**, 4414 (2013).

[198] M. Derivaz, D. Dentel, R. Stephan, M.-C. Hanf, A. Mehdaoui, P. Sonnet, and C. Pirri, Nano Lett. **15**, 2510 (2015).

[199] M. E. Dávila, L. Xian, S. Cahangirov, A. Rubio, and G. Le Lay, New J. Phys. **16**, 095002 (2014).

[200] M. E. Dávila and G. L. Lay, Sci. Rep **6**, 20714 (2016).

[201] F.-f. Zhu W.-j. Chen, Y. Xu, C.-l. Gao, D.-d. Guan, C.-h. Liu, D. Qian, S.-C. Zhang, and J.-f. Jia, Nat. Mater. **14**, 1020 (2015).

[202] S. Saxena, R. P. Chaudhary, and S. Shukla, Sci. Rep **6**, 31073 (2016).

[203] L. Li, Y. Yu, G. J. Ye, Q. Ge, X. Ou, H. Wu, D. Feng, X. H. Chen, and Y.

Zhang, Nat. Nanotech. **9**, 372 (2014).

[204]  H. Sachdev, Science **350**, 1468 (2015).

[205]  Y. Xu, B. Yan, H.-J. Zhang, J. Wang, G. Xu, P. Tang, W. Duan, and S.-C. Zhang, Phys. Rev. Lett. **111**, 136804 (2013).

[206]  S.-C. Wu, G. Shan, and B. Yan, Phys. Rev. Lett. **113**, 256401 (2014).

[207]  A. Barfuss, L. Dudy, M. R. Scholz, H. Roth, P. Höpfner, C. Blumenstein, G. Landolt, J. H. Dil, N. C. Plumb, M. Radovic, A. Bostwick, E. Rotenberg, A. Fleszar, G. Bihlmayer, D. Wortmann, G. Li, W. Hanke, R. Claessen, and J. Schäfer, Phys. Rev. Lett. **111**, 157205 (2013).

[208]  Y. Ohtsubo, P. L. Fëvre, F. Bertran, A. Taleb-Ibrahimi, Phys. Rev. Lett. **111**, 216401 (2013).

[209]  S. A. Yang, H. Pan, and Fan Zhang RSC Adv., **5**, 83350 (2015).

[210]  V. Kochat, A Samanta, Y. Zhang, S. Bhowmick, P. Manimunda, S. Asif, A. S. Stender, R. Vajtai, A. K. Singh, C. S. Tiwary, and P. M. Ajayan, Sci. Adv. **4**, e1701373 (2018).

[211]  M. Bernasconi, G. L. Chiarotti, and E. Tosatti, Phys. Rev. B **52**, 9988 (1995).

[212]  T. Kenichi, K. Kazuaki, and A. Masao, Phys. Rev. B **58**, 2482 (1998).

[213]  L. Bosio, J.Chem.Phys. **68**, 1221 (1978).

[214]  K. G. Steenbergen and N. Gaston, Phys.Chem.Chem.Phys., **15**, 15325 (2013).

[215]  O. Schulte and W. Holzapfel, Phys. Rev. B **55**, 8122 (1997).

[216]  R. N. Hall, G. E. Fenner, J. D. Kingsley, T. J. Soltys, and R. O. Carlson, Phys. Rev. Lett. **9**, 366 (1962).

[217]  H. Amano, N. Sawaki, I. Akasaki, and Y. Toyoda, App. Phys. Lett. **48**, 353, (1986).

[218]  L. E. Smart, and E. A. Moore, Solid State Chemistry: *an introduction*, (CRC press 2012).

[219]  D. S. Fisher and P. A. Lee, Phys. Rev. B 23, 6851 (1981).

[220]  W. A. Harrison *Electronic Structure and the Properties of Solids*, (Dover Publications, 1989).

[221] M. Kuno, *Introductory nanoscience: Physical and chemical concepts*, (MRS Bulletin. 2012)

[222] NW. Ashcroft, ND. Mermin, *Solid state physics*, (holt, rinehart and winston, new york, 1976).

[223] Vapnik, V. Pattern recognition using generalized portrait method. Autom. Remote Control **24**, 774 (1963).

[224] Murphy, K. P. Machine learning: a probabilistic perspective (MIT Press, Massachusetts, 2013).

[225] Arsenault, L. F. Lopez-Bezanilla, A. von Lilienfeld, O. A. & Millis, A. J. Machine learning for many-body physics: the case of the Anderson impurity model. Phys. Rev. B **90**, 155136 (2014).

[226] Ghiringhelli, L. M. Vybiral, J. Levchenko, S. V. Draxl, C. & Scheffler, M. Big data of materials science: critical role of the descriptor. Phys. Rev. Lett. **114**, 105503 (2015).

[227] Schoenholz, S. S. Cubuk, E. D. Sussman, D. M. Kaxiras, E. & Liu, A. J. A structural approach to relaxation in glassy liquids. Nat. Phys. **12**, 469 (2016).

[228] Pilania, G. Mannodi-Kanakkithodi, A. Uberuaga, B. P. Ramprasad, R. Gubernatis, J. E. & Lookman, T. Machine learning bandgaps of double perovskites. Sci. Rep. **6**, 19375 (2016).

[229] Lee, J. Seko, A. Shitara, K. Nakayama, K. & Tanaka, I. Prediction model of band gap for inorganic compounds by combination of density functional theory calculations and machine learning techniques. Phys. Rev. B **93**, 115104 (2016).

[230] Snyder, J. C. Rupp, M. Hansen, K. Müller, K. R. & Burke, K. Finding density functionals with machine learning. Phys. Rev. Lett. **108**, 253002 (2012).

[231] Bartók, A. P. Gillan, M. J. Manby, F. R. & Csányi, G. Machine-learning approach for one-and two-body corrections to density functional theory: Applications to molecular and condensed water. Phys. Rev. B **88**, 054104 (2013).

[232] Carrasquilla, J. & Melko, R. G. Machine learning phases of matter. Nat. Phys. **13**, 431 (2017).

[233]  Russell, S.J. & Norvig, P. Artificial intelligence: a modern approach
       (Pearson Education Limited, Malaysia, 2016).

[234]  Mohri, M. Rostamizadeh, A. & Talwalkar, A. Foundations of Machine
       Learning (MIT Press, Massachusetts, 2012).

[235]  Clark, T. & Koch, R. B. Machine learning : a probabilistic perspective
       (Springer Science, Berlin, 2013).

[236]  Nakhaee, M. Ketabi, S. A. & Peeters, F. M. Tight-binding model for
       borophene and borophane. Phys. Rev. B **97**, 125424 (2018).

[237]  Nakhaee, M. Ketabi, S. A. & Peeters, F. M. Dirac nodal line in bi-
       layer borophene: Tight-binding model and low-energy effective
       Hamiltonian. Phys. Rev. B **98**, 115413 (2018).

[238]  Yue, Z. Cai, B. Wang, L. Wang, X. & Gu, M. Intrinsically core-shell plas-
       monic dielectric nanostructures with ultrahigh refractive index.
       Sci. Adv. **2**, e1501536 (2016).

[239]  Yue, Z. Xue, G. Liu, J. Wang, Y. & Gu, M. Nanometric holograms based
       on a topological insulator material. Nat. Commun. **8**, 15354 (2017).

[240]  König, M. Wiedmann, S. Brüne, C. Roth, A. Buhmann, H. Molenkamp,
       L. W. Qi, X. L. & Zhang, S. C. Quantum spin Hall insulator state
       in HgTe quantum wells. Science **318**, 766 (2007).

[241]  Chang, C. Z. Zhang, J. Feng, X. Shen, J. Zhang, Z. Guo, M. Li, K. Ou,
       Y. Wei, P. Wang, L. L. & Ji, Z. Q. Experimental observation of the
       quantum anomalous Hall effect in a magnetic topological insulator.
       Science **340**, 167 (2013).

# Cirruculum Vitae

# Mohammad Nakhaee

*Curriculum Vitae*

📞 +98-912-410-1723
✉ mohammad.nakhaee@uantwerpen.be
Ⓢ Mohammad Nakhaee

---
## Contact

Researchgate   https://www.researchgate.net/profile/Mohammad_Nakhaee2

✉   mohammad.nakhaee.1@gmail.com

✉   mohammad.nakhaee@uantwerpen.be

---
## Personal

**Date of Birth**, *28-June-1985*.

**Place of Birth**, *Bam, Kerman, Iran*.

**Nationality**, *Iranian*.

**Gender**, *Male*.

**Marital status**, *Married*.

---
## Education

2014–Present   **PhD in Condensed matter Physics**, *Department of Physics*, University of Antwerp, Groenenborgerlaan 171, B-2020 Antwerp, Belgium.
and School of Physics, Damghan University, Damghan, 36715-364, Iran. (Joint-PhD)

**Thesis title**, *Tight-Binding model for 2D materials*.

2010–2012   **MSc in Astrophysics**, *School of Physics, Damghan University, Damghan*, 36715-364, Iran.

**Project title**, *Simulation of Hall Effect in Magnetized Accretion Discs*.

2003–2007   **BSc in Physics**, *School of Physics, Damghan University, Damghan*, 36715-364, Iran.

1999–2003   **High School Diploma in Mathematics and Physics**, *Rashad, Tehran*, Iran.

## Research fields of interests

**Computational Physics**.
**Computational and experimental Condensed Matter Physics**.
**Computational and experimental Nanophysics**.
**Molecular Dynamics Simulation**.

## Programming Skills

| Language | Level | Experiances |
|---|---|---|
| C++ | ★★★★★ | I have experiences of two projects (as Software Development Manager) Condensed Matter Laboratory (CML) (http://cml.du.ac.ir) and TBStudio (https://tight-binding.com). |
| Fortran | ★★★★★ | Parallelize the CML core in Fortran using OpenMPI for Green's function calculations. |
| C# and C++ .Net | ★★★★★ | I have experiences of three softwares for equipments, Electrochemical Impedance Spectroscopy (EIS), Contact Angle and SEM. The softwares communicate with the microcontrollers of the devices to control them and visualize the received data. (http://sharifsolar.ir/product-category/equ and ncl.sharif.edu). |
| C++ microcontroller | ★★★★★ | I have experiences of ARM programming microcontroller for SEM (using STM32 nucleo F746ZG board)) and communicate with the GUI software through TCP (send and receive commands) and UDP (send real time data) and communicate with other boards such as Filament and Gun Alignment through USART serial communication. (http://sharifsolar.ir/product-category/equ and ncl.sharif.edu). |
| Mathematica and Matlab | ★★★★★ | I always write my codes in Mathematica or Matlab (Serial or Parallel) and then convert them to fast programming languages such as C++ and Fortran. |
| MPI | ★★★★☆ | I have experiences of parallel programming OpenMPI in CML project. |
| Lapack | ★★★★☆ | In CML project, Solving complex matrix eigenvalue problems and inverting matrix. |
| LapackE | ★★★★☆ | In TBStudio project, Solving complex matrix eigenvalue problems. |
| Python | ★★★☆☆ | In TBStudio in menu:Code Generator, I wrote a module in c++ to generate a python code for someone who needs to do post processing in his/her own code. |
| Java | ★★☆☆☆ | Somewhat familiar in App programming for Android. |
| OpenGL | ★★★☆☆ | I used opengl programming in TBStudio project for 3D visualization of the structures and a fast 2D plotter. Also I used OpenGL for real time visualization. |
| Cuda | ★☆☆☆☆ | Somewhat familiar with GPU computing in matlab. |
| LaTeX | ★★★☆☆ | Writing papers and thesis. |

## Mathematical Techniques

| Technique | Level | Experiances |
|---|---|---|
| Nonlinear Regression | ★★★★★ | In TBStudio the aim is finding the best fitting between Tight-Binding band-structure and the the first-principles band-structure. Also in EIS software we can find the equilibrium circuit of the measured impedance. |
| Finite-Difference Method (FDM) | ★★★★★ | I have written a manuscript entitled **"Time evolution of nanoscale systems by finite difference method"**. https://arxiv.org/abs/1603.04214 |
| Finite-Element Method (FEM) | ★★★☆☆ | Some exercises. |
| Numerical Integration | ★★★★★ | In CML project: calculating Current-Voltage characteristics. I know different methods. |
| Fast Fourier Transform | ★★★★☆ | I have experience of this method in Matlab, Mathematica and Fortran. To transfer the time-dependent Green's function to energy (frequency) space. |

## Programming Techniques and Software Developing

| Subject | Level | Experiances |
|---|---|---|
| Git | ★★★★☆ | Version control and team working. The open-source TBStudio project is placed in https://github.com/mohammadnakhaee/tbstudio |
| Multi-Threading | ★★★★☆ | TBStudio regression process was programmed in another thread and the communication between two threads was implemented by custom events. |
| Packaging and Deploying | ★★★★★ | I have experiences of packaging for Windows, Debian based linux (.deb), Redhat package manager (.rpm) and Apple MacOS application (.app) (see https://tight-binding.com/download) |

## Special Packages

| Package | Level | Experiances |
|---|---|---|
| OpenMX | ★★★★☆ | I have done some DFT calculations for some of my articles by using this package. Also TBStudio has a module to import the band-structure from the .band output of this package. |
| VASP | ★★☆☆☆ | I have done some DFT calculations for some of my articles by using this package. Also TBStudio has a module to import the band-structure from its xml output. |
| Quantum ESPRESSO | ★★★☆☆ | I have some experiences in this package. I have also used this package and Wannier90 to find wannier functions. |
| Wannier90 | ★★☆☆☆ | I have some experiences in this package. |

## Publication

( 2019 ) **Tight-Binding Studio: A Technical Software Package to Find the Parameters of Tight-Binding Hamiltonian**

**Authors**: M. Nakhaee, S. A. Ketabi, and F. M. Peeters

*arXiv:1910.02917 − 7 Oct 2019 (under review)*

https://arxiv.org/abs/1910.02917

( 2019 ) **Single-layer structures of a100-and b010-Gallenene: a tight-binding approach**

**Authors**: M. Nakhaee, M. Yagmurcukardes, S. A. Ketabi, and F. M. Peeters

*PCCP 21, 15798 – 17 July 2019 (published)*

https://www.ncbi.nlm.nih.gov/pubmed/31282510

( 2018 ) **Dirac nodal line in bilayer borophene: Tight-binding model and low-energy effective Hamiltonian**

**Authors**: M. Nakhaee, S. A. Ketabi, and F. M. Peeters

*Phys. Rev. B 98, 115413 – 6 September 2018 (published)*

https://journals.aps.org/prb/abstract/10.1103/PhysRevB.98.115413

( 2018 ) **Tight-binding model for borophene and borophane**

**Authors**: M. Nakhaee, S. A. Ketabi, and F. M. Peeters

*Phys. Rev. B 97, 125424 – 21 March 2018 (published)*

https://journals.aps.org/prb/abstract/10.1103/PhysRevB.97.125424

( 2016 ) **Condensed Matter Laboratory: new application for quantum simulation.**

**Authors**: Mohammad Nakhaee, S. Ahmad Ketabi, Saeed Amiri, M. Ali M. Keshtan, Mahmoud Moallem, Elham Rahmati, M. Taher Pakbaz

https://arxiv.org/abs/1605.08604, https://cml.du.ac.ir

( 2015 ) **Influence of the soliton distributions on the spin-dependent electronic transport through polyacetylene molecule**

**Authors**: M. Nakhaee and S. A. Ketabi

*PRAMANA J. Phys. - In Press, (published)*

https://link.springer.com/article/10.1007/s12043-015-1077-6

( 2013 ) **Numerical Simulation of Hall Effect in Magnetized Accretion Discs by using Pluto Code**

**Authors**: M. Nakhaei, G. Safaei and S. Abbassi

*Research in Astronomy and Astrophysics 14, 93 (published)*

https://iopscience.iop.org/article/10.1088/1674-4527/14/1/008/meta

## Advanced courses

**Many-body quantum theory condensed matter**.
**Advanced Statistical Mechanics**.
**Advanced Quantum Mechanics (1 and 2)**.
**Electrodynamics**.
**Advanced Solid State Physics (1 and 2)**.
**Computational Physics**.
**I have also written a solution to Many-body quantum theory**, *(link)*.

## Activities

2015–Present **Programmer**, *Nanoparticles and Coatings Laboratory (NCL)*, Tehran, Iran.

| | |
|---|---|
| 2013–2014 | **Researcher and Programmer**, *Institute for Research in Fundamental Sciences (IPM)*, Damghan University, Tehran, Iran. |
| Fall 2014 | **Teaching**, *Computer programming, "Matlab Programming Chem. Sch.",* Damghan University. |
| Fall 2014 | **Teaching**, *Computer programming, "Matlab Programming Geo. Sch.",* Damghan University. |
| Fall 2015 | **Teaching**, *Computer programming, "C Programming",* Damghan University. |
| Spring 2015 | **Teaching**, *Fundamental of physics 1,* Damghan University. |
| Spring 2015 | **Teaching assistant**, *Electro Dynamics,* Damghan University, Damghan, Iran. |
| Spring 2015 | **Teaching assistant**, *Statistical Mechanics,* Damghan University, Damghan, Iran. |
| Fall 2015 | **Teaching assistant**, *Computational Physics, "Nanophysics",* Damghan University, Damghan, Iran. |
| Fall 2015 | **Teaching assistant**, *Computational Physics, "Condensed Matter",* Damghan University, Damghan, Iran. |
| Fall 2015 | **Teaching assistant**, *Computational Physics, "Astrophysics",* Damghan University, Damghan, Iran. |
| Spring 2014 | **Teaching assistant**, *Electro Dynamics,* Damghan University, Damghan, Iran. |
| Spring 2014 | **Teaching assistant**, *Computational Physics, "Nanophysics",* Damghan University, Damghan, Iran. |
| Spring 2014 | **Teaching assistant**, *Computational Physics, "Condensed Matter",* Damghan University, Damghan, Iran. |
| Fall 2014 | **Teaching assistant**, *Computational Physics, "Astrophysics",* Damghan University, Damghan, Iran. |
| Fall 2013 | **Teaching assistant**, *Computational Physics, "Nanophysics",* Damghan University, Damghan, Iran. |
| Fall 2013 | **Teaching assistant**, *Computational Physics, "Condensed Matter",* Damghan University, Damghan, Iran. |
| Fall 2013 | **Teaching assistant**, *Computational Physics, "Astrophysics",* Damghan University, Damghan, Iran. |
| Fall 2013 | **Teaching assistant**, *Computer application in Physics,* Damghan University, Damghan, Iran. |
| Spring 2011 | **Teaching assistant**, *Computer application in Physics,* Damghan University, Damghan, Iran. |
| Fall 2011 | **Teaching assistant**, *Computer application in Physics,* Damghan University, Damghan, Iran. |
| Fall 2011 | **Teaching assistant**, *Computational Physics,* Damghan University, Damghan, Iran. |

## Language

**Persian**, Native.

**English**, IELTS B2 level.

# References

**Prof. Dr. Francois Peeters**, *Professor of Physics (Head of CMT group) , Physics Department, University of Antwerp, Antwerpen, Belgium*.

✉ francois.peeters@uantwerpen.be

**Dr. Nima Taghavinia**, *Professor of Physics, Physics Department, Sharif University of Technology , Tehran, Iran and the head of Nanoparticles and Coatings Laboratory (NCL), Tehran, Iran*.

✉ taghavinia@ncl.sharif.edu

Lab Page: ncl.sharif.edu

**Prof. Dr. Seyyed Ahmad Ketabi**, *Professor of Physics, Head of School of Physics, Damghan University, Damghan, Iran*.

✉ saketabi@du.ac.ir

**Dr. Shahram Abbassi**, *Associated Professor of Physics, Department of Physics, School of Sciences, Ferdowsi University of Mashhad, Iran*.

✉ abbassi@ipm.ir